Analysis of an Actuator Disc under Unsteady Loading

Validation of Engineering Models using Experimental and Numerical Methods

Master of Science Thesis

For obtaining the degree of Master of Science in Aerospace Engineering at Delft University of Technology and in Engineering Wind Energy at Technical University of Denmark.

Vincent W. Hong

21 September 2015

European Wind Energy Master
Of
Rotor Design Track

The undersigned hereby certify that they have read and recommend to the European Wind Energy Master on the acceptance of the thesis entitled **"Analysis of an Actuator Disc under Unsteady Loading"** by **Vincent W. Hong** in partial fulfillment of the requirements for the degree of the **Master of Science**.

Dated: 21 September 2015

Chairman/Supervisor:
Dr. Carlos J., Simão Ferreira (Wind Energy Group, TU Delft)

Supervisor:
Dr. Martin Otto Laver, Hansen (Wind Energy Department, DTU)

Daily Supervisor:
Ir. Wei, Yu (DUWIND, TU Delft)

Reader:
Dr. Leif, Lind (DTU Censor)

Reader:
Dr. Andrea, Sciacchitano (Aerodynamics Group, TU Delft)

Abstract

Wind turbines operate in the earth's atmospheric boundary layer - an environment where the climate is turbulent and unsteady. In addition, wind turbines usually operate in clusters (wind farms) and are thus subjected to the unsteady wakes generated by upstream turbines. Because of the unsteady inflow, wind turbines suffer from structural fatigue damages. There is therefore motivation to better analyse and model the unsteady loading in order to design better turbines and reduce the cost of energy.

To study the unsteady aerodynamics phenomena, an actuator disc model under unsteady loading was simulated using experimental and numerical methods. Experimentally, a porous disc rotor was constructed and tested in the Open Jet Facility, TU Delft. The design involved a novel method to dynamically control the rotor's thrust coefficient through its porosity. Numerically, a dynamically loaded actuator disc was implemented in the RANS equations and solved by the commercial CFD solver `Star-CCM+`. Results from the experiment, CFD simulations, as well as a free wake vortex ring model were used to benchmark the performance of dynamic inflow engineering models.

Results show that the wake of a wind turbine under steady loading is also turbulent and meandering. The Strouhal number of the wake fluctuation closely agrees to that from a previous experiment of a 2-bladed wind turbine (Medici & Alfredsson, 2006). This suggests that the wakes of blade rotors are comparable to that from disc rotors. The tower shadow effect also bears a major influence on the inner wake profile which causes further velocity deficit and higher turbulent intensity. For rotors with higher C_T, the velocity recovery process occurs relatively earlier. This is because of the enhanced momentum entrainment arising from a steeper velocity gradient at the shear layer.

For the disc rotor under unsteady loading, the wake is affected by unsteady aerodynamics or the dynamic inflow effect. The transient velocity profile experiences an overshoot due to the passage of the 'old' and 'new' shed vortices, which are generated at the wake edge as a consequence of the uniform load profile on the rotor. The subsequent decay of the velocity in the wake or inflow at the rotor plane to the 'new' equilibrium state is a result of the rate of convection of the 'new' shed vortices to the far field. From this research, numerical results showed lower inflow velocity decay rates (velocity response due to the change in loading on the rotor) than that predicted by engineering models. While this is so, it was found that the decay rate is highly influenced by the ambient flow's turbulence. At high ambient turbulence, the 'new' equilibrium state is achieved in a shorter time due to the enhanced momentum mixing process. It is hypothesised that this is the primary reason behind the higher decay rates predicted by empirical-based engineering models.

Acknowledgements

This thesis would not have been possible without the support from many. I sincerely thank the EWEM programme, for without which I may not have the opportunity to learn from two leading European universities. Also the EWEM coordinator, A/Prof. Carlos (TU Delft) has been supportive towards my work as my supervisor. His teachings, encouragement and the regular conversations has given helpful suggestions towards a successful experimental campaign. A/Prof. Martin (DTU) has pioneered my knowledge on wind engineering and through his introduction to `Star-CCM+`, I have learnt a great deal on running CFD simulations. My appreciation also goes to Wei of the Wind Energy Group in TU Delft. Besides being my regular 'go-to' person for any thesis related discussion, she has been un-relentless towards the research cause and the experimental work in the OJF could not have been possible if not for her resourcefulness and 'can-do' attitude. I enjoyed our partnership and wish her the best.

My thanks also go to Daniel Baldachinno, Gael de Oliveira Andrade and Lorenzo Lignarolo. All of them have been friendly in sharing their knowledge so that I can improve my understanding and translation of both the theoretical and experiment aspects of the work. Although the PIV setup was not successful, my thanks also goes to A/Prof. Daniele Ragni for his valuable time and advice.

Experimental work in the OJF is always hard work. Due to the larger scale model, every gadget, device, setup and their associated challenges are also scaled. It would have not been possible to have workable test apparatus if not for the support from the staff of Aerodynamics Laboratory. Nico van Beek, Stefan Bernady, Peter Duyndam and Frits Donker Duyvis have contributed substantially towards the experimental setup. The people at DEMO (electronics and mechanical workshop), especially Ed Roessen and his colleague Rob, have always acceded to our incessant modification requests. The successful disc rotor model is a testimony to their standards of quality and ethics. From time to time, it was also pleasant to tap on the experiences of Prof. Gijs van Kuik, Prof. Fulvio Scarano and Nando Timmer, when they came by the OJF and gave pointers so that we could avoid possible pitfalls. Their kind insights were necessary and have contributed to my success.

I may have inadvertently missed out some names here, but that should not take away any credit if they have contributed to my work in one way or another. I hope I made some friends along the way.

Last but not least, my love and gratitude goes deep for my family and friends. They are, who I am.

Thank you.

Contents

List of Figures

List of Tables

Nomenclature

Acronyms

AD	Actuator Disc
CFD	Computational Fluid Dynamics
DES	Detached Eddy Simulation
DNS	Direct Numerical Simulation
FWVR	Free Wake Vortex Ring model
HWA	Hot Wire Anemometer
LES	Large Eddy Simulation
MT	Momentum Theory
NS	Navier Stokes
OJF	Open Jet wind tunnel Facility in Delft University of Technology
RANS	Reynolds Averaged Navier-Stokes

Alphabet Symbols

$\overline{V}$ or V	mean (time-averaged or ensemble-average) velocity $[ms^{-1}]$
$\widetilde{\Delta V}$	relative change in velocity normalised by the values at the initial and steady state of an unsteady load cycle.
A	Rotor area $[m^2]$
a_{avg}	axial induction factor averaged over the rotor area $[-]$
c	chord length $[m]$
C_T	thrust coefficient $[-]$
D	rotor diameter $[m]$
K	Turbulent Kinetic Energy $[m^2s^{-2}]$
l_m	Prandtl Mixing Length $[m]$
nD	distance equivalent to n rotor diameters downstream $[m]$
t^*	Time non-dimensionalisd by τ $[-]$
t_1	Time associated with the in-stationary profile aerodynamics $[s]$
t_1^*	Non-dimensional time response associated with the in-stationary profile aerodynamics effect $[s]$
t_2	Time associated with the in-stationary wake effect $[s]$

t_2^*	Non-dimensional time response associated with the in-stationary wake effect [s]
th	Disc Thickness [m]
TI	Turbulent Intensity [$-$]
v	instantaneous velocity [ms^{-1}]
V_0	mean undisturbed freestream velocity [ms^{-1}]
v_x	instantaneous velocity in the streamwise direction [ms^{-1}]
V_{avg}	velocity averaged over the rotor area [ms^{-1}]
W	induced velocity [ms^{-1}]
a	axial induction factor [$-$]
n-D	n dimensional space
R	rotor radius [n]
St	Strouhal Number

Greek Symbols

δt	Duration of the load unsteadiness [s]
η	Kolmogorov length scale - smallest scale in turbulent flow [m]
κ-ϵ	RANS 2-equation Turbulence model
κ-ω	RANS 2-equation Turbulence model
μ	dynamic viscosity [$kgs^{-1}m^{-1}$]
ω	vorticity or the curl of velocity [s^{-1}]
ρ	density [kgm^{-3}]
τ	time scale associated with the dynamic inflow phenomenon [s]
θ	azimuthal angle measured from rotor axis [$^\circ$]

"We need to bring sustainable energy to every corner of the globe with technologies like solar energy mini-grids, solar powered lights, and wind turbines."

Ban Ki-moon (1944 – present)

1 Introduction

1 Current Wind Energy Landscape

With the Industrial Revolution in the late 18th century, the world has been largely dependent on traditional energy sources such as oil, coal and natural gas. Since then, global energy demand has been rising exponentially owing to emergence of developing economies. Up till now, the conventional knowledge is that traditional energy sources are finite and would at some point be depleted. To complement traditional energy sources, there has been growing support on developing renewable energy, of which wind energy has a significant role. Owing to industrial and societal support, there has been spurt growth in the harness of wind energy, especially in the last 50 years. Countries adopting wind energy as a energy source has been largely the developed nations with supporting financial and knowledge economies. The adoption has been complemented by the deeper understanding of wind engineering through sustained research activities. In Europe, the European Union has legislated that renewable energy sources should rise to 20% by the year 2020, and the target is expected to further increase in the future. This motion has led to several off- and onshore wind farms being built in the last twenty years and with many more planned up to 2050.

2 Principles of Wind Engineering

Wind turbines usually operate in clusters at sites with high levels of wind resource. During power generation operation, the power extraction from wind causes a momentum deficit after the rotor, resulting in lower velocities in the wake, than the free stream velocity (outside of the wake). This means wind turbines sited downstream in the wakes of upstream turbines could be affected, depending on the spatial distance between turbines. This spacing is closely co-related to the momentum recovery or re-energization of the wake. Intuitively, for larger spatial distances, the momentum of the wake is likely to have recovered. Depending on the ambient and wake-induced turbulence, it is known than wake losses of between 20% and 25% have even been observed at distance of up to 40 rotor diameter (40D) downstream. It is therefore, a fine balance and trade-off between a tightly spaced turbine layout in the windiest sector and a loosely spaced layout that extends into lower wind speed sectors, but experience less wake losses.

To optimise the material of wind turbines against fatigue and extreme load cases, the aerodynamics loads experienced by wind turbines need to be better analysed and modelled. In real operating conditions, the loading on rotors fluctuate due to unsteady inflows as these machines operate in the atmospheric boundary layer.

3 Research Context

Many factors affect the performance of a wind farm. Most obviously, the wind climate affects power extraction by individual turbines whereby the generation of lower speed turbulent wakes affect downstream turbines. Wind is both a non-dispatchable resource i.e. its request cannot be controlled and its behaviour is also turbulent - therefore, somehow not exactly predictable. With dynamic inflow conditions, wind turbine rotors are subjected to unsteady aerodynamic loads. Load fluctuations cause material fatigue damage which further increases with higher unsteadiness. Therefore, the unsteady wake development process is of great research interest as it affects the lifetime of wind turbines and more importantly, the cost of energy.

It is therefore of academic and commercial interest to study the wake characteristics and its development in order to assess the power performance and its influence on the fatigue lifetime of wind turbines. In [37], experimental data has been gathered for actuator discs subjected to steady loads. This research project builds on the work in [37] through an experimental and numerical analysis of an actuator disc subjected to unsteady loads.

Aerodynamics engineering models are characteristic relations which predict the rotor's aerodynamic response under a given flow situation. Such models are usually derived from either or both empirical data and the flow physics. In wind turbine aerodynamics, the actuator disc (AD) model forms the basis of many state of the art aeroelastic codes. Since AD theory is premised on quasi-steady or the equilibrium wake state assumption, it is unlikely to be accurate in unsteady flow situations. These aeroelastic models are therefore usually coupled with engineering 'add-ons' for correction in order to reduce the uncertainties under unsteady flow situations (e.g. dynamic inflow, unsteady profile aerodynamics and yawed flow).

Alternatively, Computational Fluid Dynamics (CFD) simulations can also be performed to obtain the aerodynamic solution. This involves solving the Navier-Stokes equations which govern the flow physics. If done correctly, these results are usually of high-fidelity and highly dependable. However, good CFD simulations are computationally expensive and require far longer time. The choice between engineering models and CFD simulations is essentially the balance between computation effort and the accuracy of the results. More often than not, engineering models are preferred as they are usually computationally fast and easy to implement.

4 Research Motivation and Objective

In the course of this review, it has been found that while there are many measurements work has been done regarding the dynamic inflow on bladed wind turbine rotors, no published records exist on the use of actuator discs to investigate the phenomena due to unsteady loading. The use of an actuator disc to numerically and experimentally investigate dynamic inflow effects is interesting as it lends a fundamental perspective to many existing engineering models, which are based on AD theory. This thesis's research objective is to validate state of the art dynamic inflow engineering models through experimental and numerical methods. The most common engineering models of [49] and [47] will be benchmarked.

The scope of this research involves the investigation of aerodynamic effects of an actuator disc subject to unsteady loading. By controlling the rate of change of the unsteadiness, unsteady flow effects can be simulated. At an inflow unsteady time scale order of $\frac{D}{V_0}$ [58, 54], there is a time lag in the load response due to the influence of the time varying shed vorticity on the velocity at the rotor plane. A response delay of the downstream wake is also expected as it adjusts to the unsteady flow regime at the rotor.

Comprehensive field[58] and wind tunnel[54] experiments on wind turbines have demonstrated the existence of this unsteady flow phenomenon. In these experiments, the wind turbine blades were subjected to fast blade pitching to invoke the dynamic flow response. In a way, the use of an actuator disc model in this thesis represents a novel approach, which is fundamentally simple and computationally cheaper, as opposed to a blade rotor.

5 Report Outline

In Part I, the steady, inviscid actuator disc theory is briefly introduced and followed by a discussion of its reliability in modelling the flow of a horizontal axis wind turbine. This is followed by a presentation on the wake development of a wind turbine where the physics of the phenomenon will be explained. Subsequently, unsteady aerodynamics will be introduced, as well as the engineering models that will be benchmarked in this thesis. Lastly, an overview of a vortex method (FWVR) to model the rotor's transient and steady wake response will be covered.

In Part II, a numerical analysis of an actuator disc subjected to unsteady loading will be presented. This is first preceded by an introduction to the field of computational fluid dynamics and the broad stages involved in such numerical computations. The different RANS turbulence models to solve the Navier-Stokes equations will also be included. Finally, the setup and validation of the actuator disc model in the commercial CFD solver `Star-CCM+` are presented.

In Part III, the design process of the porous disc rotor used in the two experimental campaigns is reported. This includes the technique on how dynamic thrust coefficient rotor was achieved. This is followed by a short write-up on the various aerodynamic measurement techniques used during the testing. Finally, the experimental apparatus and layout are presented.

Finally in Part IV, results from the CFD simulations and wind tunnel experiments are presented and analysed. Using these results and that from the FWVR, the performances of the dynamic inflow engineering models are benchmarked. From the comparisons, analyse and discussions were made before drawing conclusions. This part also contains proposals on further enhancements and suggested extensions to this research.

Part I: Literature Review

"Among existing methods fuzzy set theory appears to be a mathematical system which is instrumental in constructing formal models of imprecise [design] behavior."

Yee Leung

2 Actuator Disc Model

1 Aerodynamics modelling of Horizontal Axial Wind Turbines

A wind turbine is an aerodynamics machine, where kinetic energy is extracted from the wind to perform mechanical work (turning of the generator). This process of extracting energy is an aerodynamic process as the generation of the force (to perform useful work) has occurred as a result of the flow changes as it passes a shaped structure - in this case, the shaped structure is the blade. Describing the aerodynamic effects involves having knowledge on the fundamental flow properties such as pressure and velocity. Through these quantities, other affected flow properties such as the turbulent intensity and loads can be determined. The study of the aerodynamics of rotors is usually done at two parts of the flow field:

(a) Near Wake. Resolving the flow field at the rotor plane and a short distance downstream is to primarily obtain the flow velocity and pressure field. Flow field in the near wake exerts the largest influence on the rotor due to its vicinity and the information is then used to determine the load response and induced velocity.

(b) Far Wake. The flow field far downstream is known as the far wake of a wind turbine. Fluid properties of the far wake is important in order to understand wake development dynamics and its development. This information would facilitate better wind farm planning as the wind turbines can appropriately sited to optimise the total energy production and reduce fatigue damages.

2 Actuator Disc Theory

The presence of the rotor causes the flow velocity in the wake of a rotor to be reduced from the value of the freestream velocity. From the principle of energy conservation, the wind leaving the turbine must have a lower energy content that the wind arriving in front of it since energy has been expended to perform mechanical work (turn the generator). The amount of velocity which is 'lost' at the rotor plane is known as the induced velocity and is usually conveniently expressed using a term called the induction factor a, as a multiple of the freestream velocity V_∞.

To resolve the flow field of a wind turbine, the concept of axial momentum theory[27] is used, which is part of the basis of the Blade Element Momentum (BEM) model. Also known as actuator disc theory, it describes a infinitely thin disc subjected to one-dimensional flow. The location of the actuator disc is a momentum sink (or momentum source in the case of helicopter aerodynamics). It is key to note that the actuator disc is not a physical disc but a hypothetical model which slows the incoming flow. The amount of momentum exchange between the actuator disc is a result of the aerodynamic design. Since the amount of momentum exchange of an actuator disc is directly related to the turbine's thrust coefficient[22] (or drag in the flow's reference frame), the thrust coefficient of the disc and a bladed rotor should be matched for aerodynamic similarity. By applying conservation of mass, momentum and energy, many interesting relationships between the axial induced velocity and the axial force can be derived.

2.1 Assumptions of Actuator Disc Theory

Underpinning the axial momentum theory are the following assumptions:

(a) Incompressible fluid. Flow around a wind turbine is incompressible as the tip speed is generally limited to around 80 m/s[54], which is below the generally accepted compressible Mach number limit of 0.3.

(b) Inviscid fluid. Inviscid flow means that there are no shearing effect between air particles. This is of course not valid, especially in flow separation cases for which turbulence generation becomes a flow-influencing phenomenon.

(c) One dimensional. Flow is assumed to be one-dimensional in order to simplify the analysis. However, it should be noted that in real wind conditions, the turbine is operating in yaw conditions due to wind directional changes.

(d) Uniform loading. The assumption of flow uniformity is analogous to a rotor with infinite number of blades. If an accurate and realistic prediction of the rotor's aerodynamics is desired, corrections to the AD model need to be included.

2.2 Momentum Conservation

To apply momentum conservation, a streamtube and the adjacent flow are considered as shown in Figure 2.2.

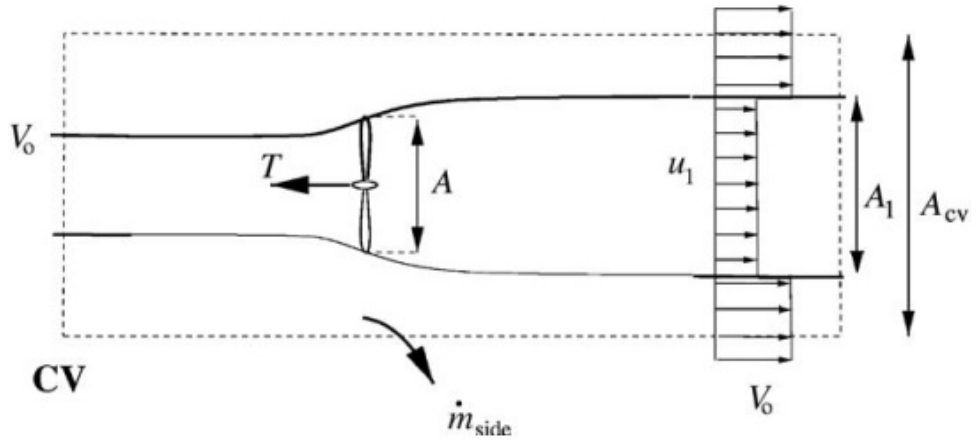

Figure 2.1: Control Volume encompassing a streamtube (far up- and downstream) with an actuator disc applying a force T on the incoming flow[30].

A control volume (CV) analysis is invoked to obtain conservation of momentum where

$$\begin{aligned} &\text{Incoming Momentum} = \text{Outgoing Momentum} + \text{Momentum Exerted on the Flow} \\ &\implies \rho A_{CV} V_0^2 = \rho A_1 u_1^2 + \rho(A_{CV} - A_1)V_0^2 + \dot{m}_{side} V_0 + T \end{aligned} \tag{2.1}$$

Equation 2.1 essentially describes that the incoming flow is slowed according to the amount of thrust (axial) force acting on the fluid. In other words, for a non-loaded rotor (or a C_T value of 0), the flow will not slow down at the rotor plane, just like as though there was no obstacle in the flow (noting again that the actuator disc is hypothetical). For an actual rotor turbine, the amount of thrust exerted on the flow would depend on its aerodynamic design.

2.3 Mass Conservation

Invoking the laws of mass conservation (or mass continuity) on the same CV, the following is obtained:

$$\begin{aligned} \dot{m}_{side} &= \rho A_{CV} V_0 - \rho A_1 U_1 - \rho(A_{CV} - A_1)V_0 \\ &= \rho A_1 (V_0 - U_1) \end{aligned} \tag{2.2}$$

At the rotor plane, the flow velocity reduces due to energy extraction. This means that the streamtube downstream of the rotor plane must expand. If not, mass conservation law would be violated!

2.4 Energy Conservation

Since the total energy of a closed system is constant, the energy (or the total pressure) of the flow should be constant. Given that the presence of the rotor extracts energy from the flow, this represents a discontinuity in the energy level and therefore energy conservation should only be applied to from (a) far upstream to just before the rotor plane and (b) just after the rotor plane to downstream. Assuming incompressible flow, Bernoulli's equation can be conveniently applied as in the following (see Figure 2.2):

$$\left.\begin{aligned} P_0 + \frac{1}{2}\rho V_0^2 &= P + \frac{1}{2}\rho u^2 \\ P - \Delta P + \frac{1}{2}\rho u^2 &= P_0 + \frac{1}{2}\rho u_1^2 \end{aligned}\right\} \implies \Delta P = \frac{1}{2}\rho(V_0 + u_1)(V_0 - u_1) \tag{2.3}$$

As seen in Figure 2.2, in the case of the loaded disc, for the flow to slow down after the disc, the streamtube that encapsulates the rotor has to expand in order to fulfil the law of mass continuity. By applying Bernoulli's continuity equation before and after the disc and mass continuity, the flow experiences a drop in static pressure after the disc. It should be also noted that flow dynamics is a continuum, i.e. flow changes cannot be abrupt ot instantaneous, the change in the steady state values of the flow speed and pressure must take place over a certain distance.

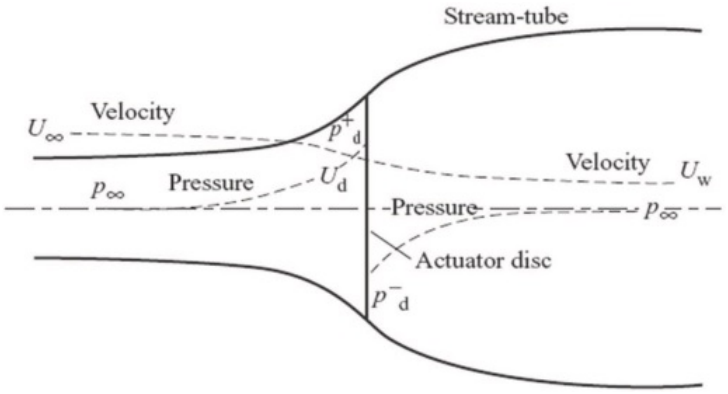

Figure 2.2: Streamtube analysis of an actuator disc showing the pressure and velocity at far upstream, disc and far downstream[16]. The subscripts ∞ and w correspond to 0 (freestream) and 1 (far wake) of Figure 2.1.

By equating $\dot{m}_{side}$ from Equation 2.1 and Equation 2.2, the resulting equation can be compared to Equation 2.3 to give:

$$\left.\begin{aligned} \text{(2.1) \& (2.2)} &\implies T = \rho A_1 U_1 (V_0 - U_1) = \rho A_d U_d (V_0 - U_1) \\ \text{(2.3)} &\implies T = \Delta P A_d = \frac{1}{2}(V_0 + U_1)(V_0 - U_1) A_d \end{aligned}\right\} \implies U_d = \frac{1}{2}(V_0 + U_1) \quad (2.4)$$

An interesting relationship has now been derived in Equation 2.4, where it means that the velocity at the rotor plane is half of the velocities of the free stream and far wake! It is also interesting to note as the velocity between the rotor plane and far wake is reducing, the wake (or the streamtube in this analysis) has to expand to comply with the mass conservation law.

It is now convenient to define the axial induced velocity W, which is defined as the velocity deficit (or mathematically, the difference between V_0 and U_d) as a result of the energy extraction by the rotor. The induced velocity is usually expressed as a ratio of V_0, known as the induction factor a (see Equation 2.5).

$$U_d = (1 - a)V_0 \quad (2.5)$$

$$U_1 = (1 - 2a)V_\infty \quad (2.6)$$

At this point, it is convenient to non-dimensionally quantify the power extracted and thrust exerted from the flow where:

$$\text{Power:} \quad P = \frac{dKE}{dt} = \frac{1}{2}\rho U_d A (V_0^2 - U_1^2) = 2\rho V_0^3 a (1 - a)^2 A$$

$$\implies C_P = \frac{P}{\frac{1}{2}\rho V^3 A} = 4a(1 - a)^2 \quad (2.7)$$

$$\text{Thrust:} \quad T = \rho A_d U_d (V_0 - U_1) = 2\rho V_0^2 a (1 - a) A$$

$$\implies C_T = \frac{T}{\frac{1}{2}\rho V_0^2 A} = 4a(1 - a) \quad (2.8)$$

By plotting Equation 2.7 and Equation 2.8 for a range of lowly to highly loaded rotors, we see the following trends as shown in Figure 2.3. Here, axial momentum theory predicts an interesting fact that there is a limit $\frac{16}{27}$ on the power extraction efficiency (denoted by the maximum of the C_P curve). This limit is known as the Betz limit[12] and occurs for $a \approx \frac{1}{3}$. Since actuator disc theory deals with

an idealised flow (1-dimensional, uniform induction at rotor plane), this means that even the best axial wind turbine applications can never outperform the Betz limit!

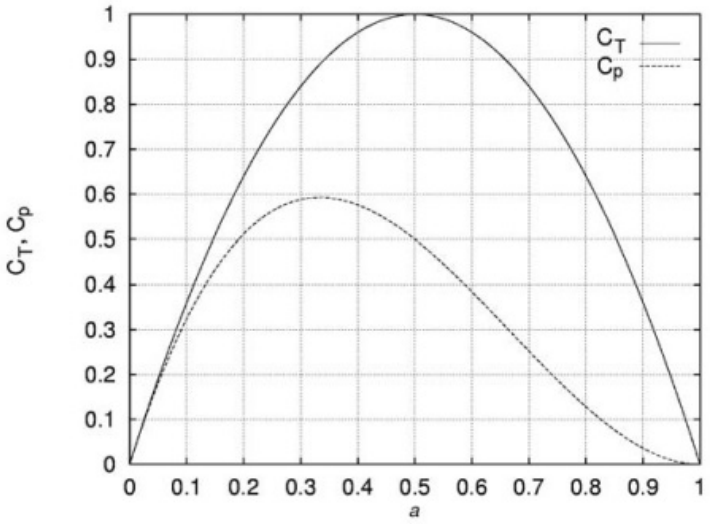

Figure 2.3: Coefficient of Power and Thrust with respect to Axial Induction Factor as predicted by Actuator Disc Theory[30].

2.5 Size of Fully Expanded Near Wake

Mass continuity can also be invoked to determine the size of the fully expanded wake, downstream of the turbine.

$$\begin{aligned} \rho_\infty A_{disc} V_{disc} &= \rho_\infty A_{wake} V_{wake} \\ \pi \left(\frac{D}{2}\right)^2 \cdot (1-a) V_0 &= \pi \left(\frac{d_{wake}}{2}\right)^2 \cdot (1-2a) V_0 \\ \implies \quad d_{wake} &= \sqrt{\frac{1-a}{1-2a}} D \end{aligned} \tag{2.9}$$

For the case of $C_T = \frac{8}{9}$, the inviscid momentum theory predicts an induction factor of $a = \frac{1}{3}$. This gives a fully expanded wake of $\sqrt{2}D \approx 1.4D$.

The distance over which the near wake fully expands is dependent on the rotor's thrust coefficient and ambient conditions. Field surveys conducted in [23] have estimated the wake to be fully expanded at 1D, while numerical wake models such as [53] use a distance of 2.25D.

3 Limitations of Actuator Disc Theory

From Equation 2.6, it can be deduced that as the axial induction factor increases, the wake velocity decreases. Following this theoretical arugment, when a increases to 0.5 and above, V_{wake} would become zero or negative. In reality, the flow aft the disc has to move downstream, otherwise there would be a mass of stationary fluid collected which is non-physical. Therefore, under highly loaded conditions (i.e. large a), the actuator disc momentum theory is no longer valid. In order to extract from energy from the flow, the rotor has to exchange more momentum with the flow by exerting a

larger force (higher C_T) to further slow the incoming flow. However, the fundamental actuator disc theory predicts otherwise, which is therefore not exactly a useful model to predict loads at high C_T.

3.1 Turbulent Wake State

Real flows cannot be considered as inviscid, contrary to the assumptions in actuator disc theory. At high C_T, the large expansion of the streamtube results in the shear layer (defined as a turbulent region which forms at the edge of the wake) becoming unstable due to the presence of a high velocity gradient. This turbulent shear layer results in the formation of eddies which help to transport momentum from the outer undisturbed flow into the wake (see Figure 2.4). In such cases, the flow situation is termed as a turbulent wake state. In other words, even at high C_T, the wake does not stop, as opposed to actuator disc theory.

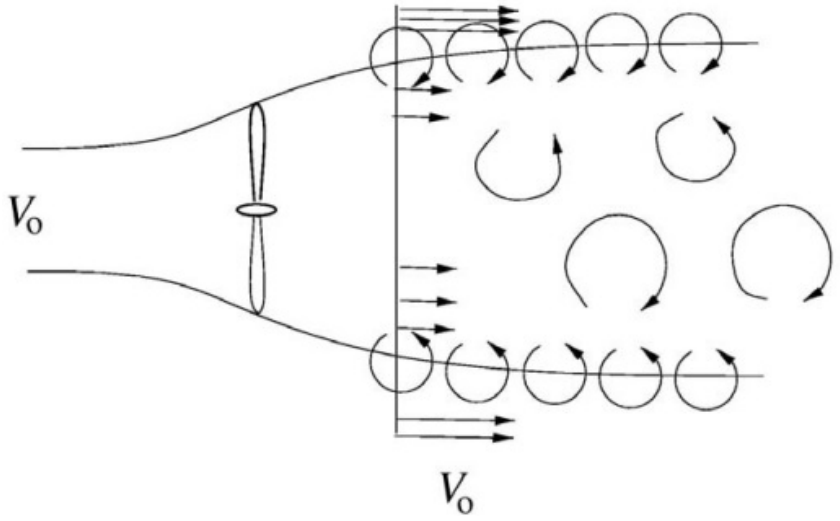

Figure 2.4: Turbulent Wake State at high axial inductor factors[30].

4 Relevance of Actuator Disc Model

The effectiveness of an AD to model an actual wind turbine rotor has been extensively studied. It is a generally well accepted and is the basis behind the popular Blade Element Theory (BEM) model. Many commercial wind turbine design codes (such as `BLADED`, `HAWC-2`, `AeroDyn` etc) also based their aeroelastic codes on the BEM model due to low computation requirements and reliable results.

A key feature of a blade rotor is the tip vortices development and its subsequent breakdown. This phenomenon has an effect on the near wake velocity and turbulence development and is different from that of a disc rotor[11] whose vorticity is distributed throughout the wake volume. Because of this, wakes of disc rotors have excessive turbulence peaks and enhanced dissipation in the near wake. Besides the tip vortices, the blade movement also causes flow swirls that are inherently not considered for a disc rotor. On the other hand, the far wake of both blade and disc rotors has been found to be very comparable. To achieve this similarity, the matching of C_T for both rotors was found to be the key and shown in many experimental works such as [31], [50], [36] and [6]. While the mentioned works deal with rotors under steady conditions, [47], [59] and [24] have implemented AD based engineering models to deal with unsteady flows.

To experimentally implement an actuator disc, a porous disc is often used. The circular discs are usually made from wire mesh or plates with holes. Although the presence of the discrete discrete

holes in the porous material creates small-scale length turbulence, this approach has been validated in [35], where LES computations and experimental results were compared.

A key value proposition afforded by the AD model is in its implementation simplicity to analyse flow problems. From an experimental perspective, disc rotors do not suffer from scaling issues compared to blade rotors. To model a 10 m diameter turbine spinning at 15 RPM, a 1:10 model would have to be spinning at 1500 RPM. This poses implementation challenges and the fast rotor spin would also introduce unrealistic swirls into the wake[7].

From a numerical perspective, using a AD model would avoid the need to capture the boundary layer development around the turbine. Modelling wind farm aerodynamics using full wind turbines models is extremely prohibitive and the use of AD models would result in very substantial computation savings as the mesh density can be lower. Thus, AD models are usually the choice to study the downstream wakes and their effects.

"I'm a great believer that any tool that enhances communication has profound effects in terms of how people can learn from each other, and how they can achieve the kind of freedoms that they're interested in."

Bill Gates, (1955 – present)

3

Wake Development

This chapter discusses the wake development of a wind turbine. The analysis will be divided into two parts: at the near wake and the far wake. Referring to Figure 3.1, it can be generally taken that the near wake is a region which has low momentum flow, followed by the momentum recovery process in the far wake.

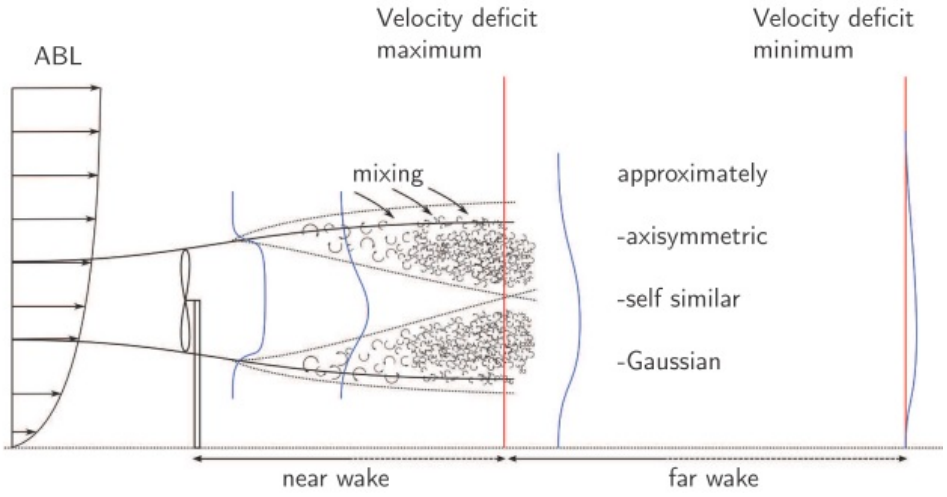

Figure 3.1: Schematic depicting the Near and Far Wake of a Wind Turbine[52].

1 Near Wake

The area just behind the rotor is known as the near wake. There have been many suggestions on the length of the near wake. In [64], it was described that the wake is approximately 1 rotor diameter (1D) downstream, while in [42], Medici describes the near wake region is up to 10D. Distances between 6D and 10D which are rough space parameters to space wind turbines in clusters. Indeed, the decision on spatial distances between turbines is influenced by the wake recovery distance. This distance refers to recovery of the momentum deficit in the flow before meeting the subsequent downstream turbine. In the following section, it will be explained that the near wake can be described to be up to the

region where the expansion of the shear layer meets the turbine axis.

1.1 Shear Layer

A shear layer is formed due to the difference in the velocity between the flow inside the wake and the freestream. This shear layer is characterised as a turbulent region which expands downstream. As a result of mass conservation, the flow expands and the velocity in the wake decreases. In [1], the author estimates that the maximum deficit occurs about one to two rotor diameters according to C_T of the rotor. For viscous flows, turbulent eddies are formed due to shearing effects and thus the so-called shear layer (see Figure 3.2).

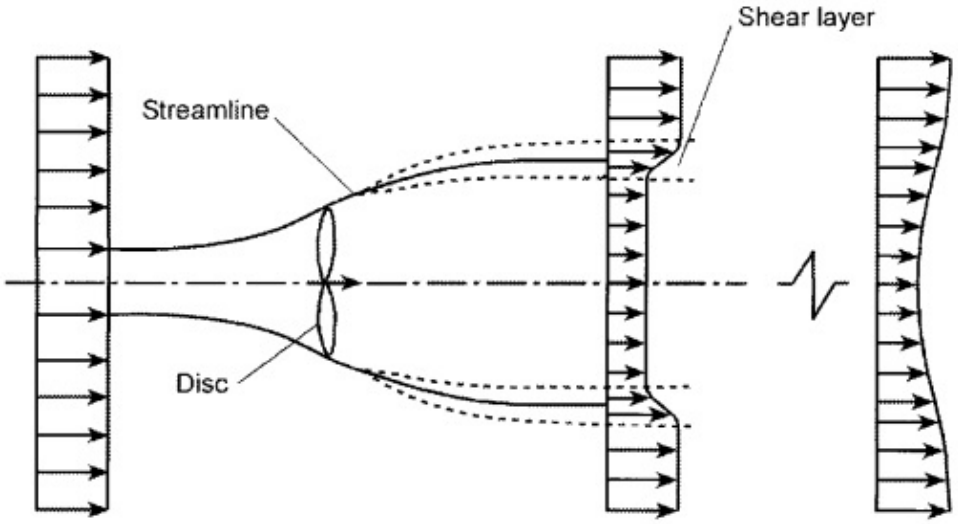

Figure 3.2: Schematic depicting the Shear Layer of a Wind Turbine Wake[23].

The presence of the rotor, leads to a slower flow field and a corresponding wake expansion according to mass conservation. At a sufficiently high expansion, the resulting turbulent eddies leads to the so-called turbulent wake state. A higher thrust of the rotor leads to a lower wake velocity and thus forms stronger vortical structures. These eddies entrain the velocity from the freestream and increase the wake's momentum by mixing from the wake edge to the inner flow. In this momentum mixing process, the shear layer begins to diffuse or thickens.

1.2 Tip Vortex Production

Vortices are largely produced at the blade tips due to pressure differences at the pressure and suction sides of the blade. For a given aerodynamic design of the blade, one can also expect vortices to be shed everywhere on the blade due to the span-wise variation of the load (or the bound vorticity). To illustrate this, one can picture the model of a horseshoe vortex to represent the circulation on a finite section of a wing. A horseshoe vortex model is mooted as it fulfils the Kelvin's theorem of the conservation of circulation $\frac{d\Gamma}{dt} = 0$.

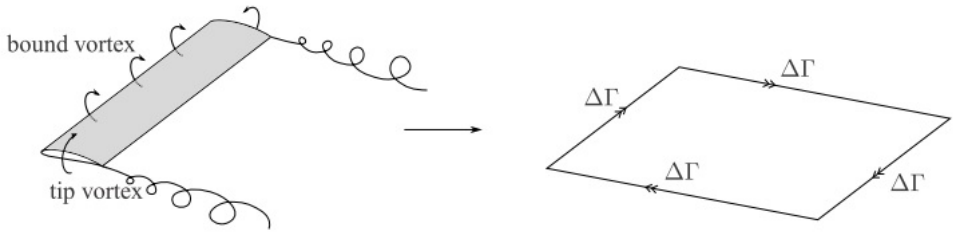

Figure 3.3: Use of a Horseshoe Vortex model to represent the circulation on the finite section of a wing.[52].

These tip vortices have been observed in many experiments. Since each blade sheds a tip vortex at a azimuthal position during one revolution, this results in vortex rings forming a helical structure that is convected downstream. In Figure 3.4, a trail of smoke particles has been injected to follow the streamlines of the incoming flow. This flow visualisation shows the formation and convection of tip vortices at an azimuthal position of the rotor plane. In this example, six coherent vortical cores are seen which have been produced in three full revolutions of the rotor.

Figure 3.4: Flow Visualisation of the Tip Vortices of a 2 Bladed Rotor[3].

The formation of the helical vortex rings was observed in the experiment of the NREL wind turbine in the NASA-AMES Wind Tunnel (see Figure 3.5a). In the experiment, smoke particles is injected at the blade tips to trace the movement of the tip vortices. Due to the rotor rotation, the tendency is for the helix to rotate opposite to the rotation direction. It should also be noted that the number of spirals in the helix is dependent on the number of blades. In Figure 3.5b, the presence of three blades result in the formation of three distinct spirals.

With increasing rotation speed Ω or with increasing number of blades, the tip vortices would be formed closed (streamwise distance) to one another. Rows of tip vortices which are formed closed to each other is a so-called tubular vortex sheet, as would be observed in the case of a flow past a disc. As the number of blades increase, the path of the spirals or tip vortices will also be increasingly

parallel to the rotor plane. The helical angle ϕ, defined as the flow angle at the blade tip, is therefore inversely proportional to Ω.

(a) Wake of a two-bladed 10 m diameter horizontal axis wind turbine[56]

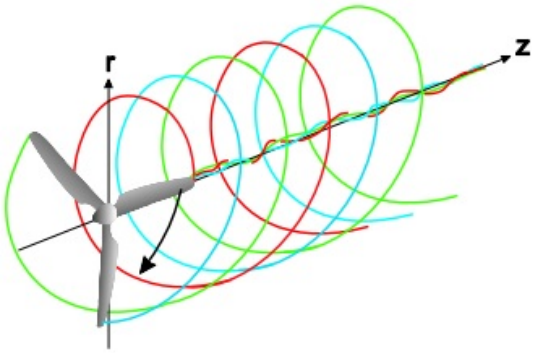

(b) Numerical visualisation of the wake of a three-bladed wind turbine rotor[33].

Figure 3.5: Vortices are generated from the blade tips and convected downstream to form a helical-shaped wake.

1.3 Azimuthal Induction

Considering a case where the inflow velocity is straight and uniform, the wake has a azimuthal component (i.e. wake is rotating with respect to the rotor axis). This azimuthal movement is due to both the rotating rotor and the aerodynamic induction in the azimuthal direction. The azimuthal induction (denoted as a') can be said to be therefore influenced by the aerodynamic design, since it occurs due to presence of the rotor.

However, it should be noted that the azimuthal velocity is usually driven by the speed of the rotor rotation as the azimuthal induction is relatively small. In [42], it was experimentally found that the maximum azimuthal velocity at 1D is of the order of 10-15% of the free stream velocity.

1.4 Diffusion of Shear Layer

Just after the rotor plane, tip vortices are coherent and can be visually distinguished. These vortices are present in the shear layer and form a vortex sheet, which separates the flow in the wake and the freestream. The tip vortices also serve as a medium to transport higher momentum flow from the fresstream into the wake. After a certain distance downstream, one vortex of each tip vortex pair catches with the other, resulting in a 'leap-frogging' phenomenon. Eventually, the spirals tracing the path of the tip vortices become intertwined. This is seen in the experimental works of [63] (see Figure 3.6). In the figure, the tip vortices trace the wake edge and therefore indicates the expansion of the wake.

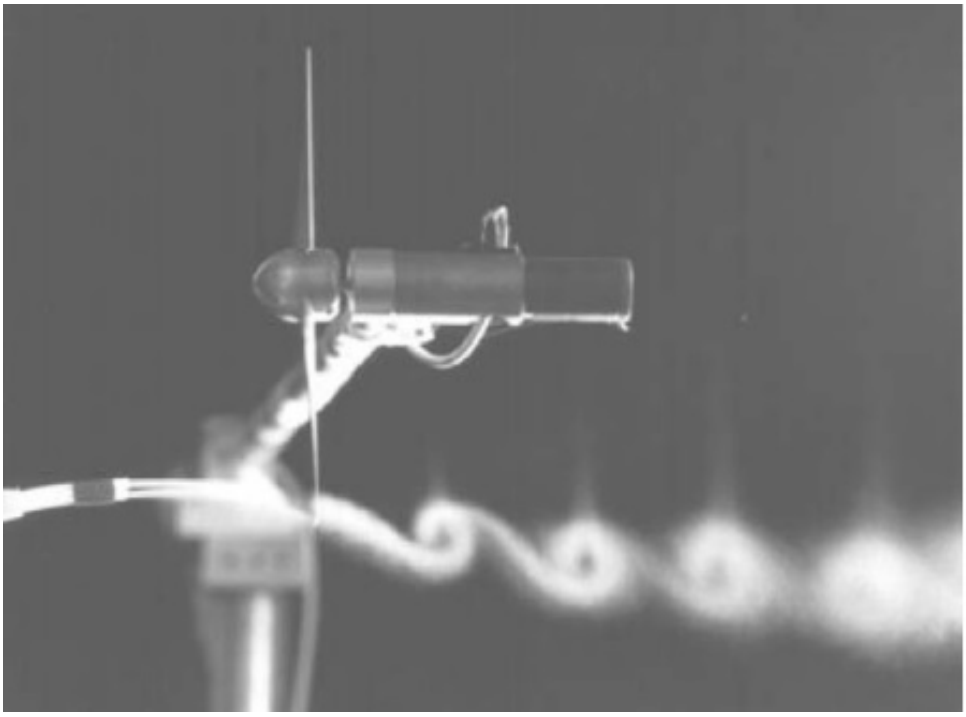

Figure 3.6: Tip Vortex breakdown after about 2 revolutions seen in the works of [63].

An explanation for the leap-frogging phenomenon (see Figure 3.7) of the tip vortices can be explained as such. Due to the introduction of flow perturbations, each of the tip vortices would have their own path and transport velocity, which results in one eventually catching up with the other.

Flow perturbations can for example, be introduced when the blades are set at different pitch angles. The onset of this instability is therefore highly dependent on the mounting of the blades (pitch) and boundary condition at the rotor. Under atmospheric wind climate conditions, the presence of ambient turbulence mean perturbations are inherent. Rather, it should be a question how the strength of the perturbation would invoke the vortex pairing instability. In the experimental analysis of [36], it was also shown that this instability phenomenon has an earlier onset with higher tip speed ratios. This can be attributed to the formation of spirals which are spaced more closely to each other, leading to an earlier instability tendency.

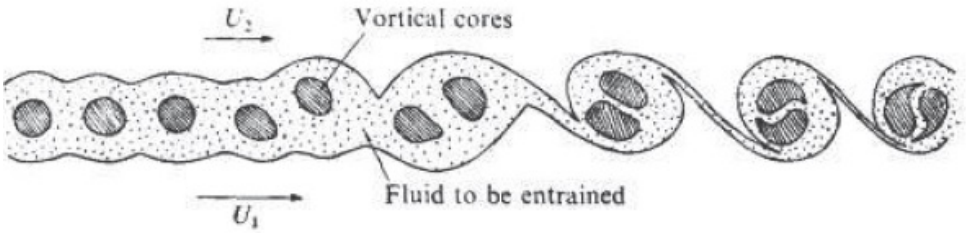

Figure 3.7: Schematic showing the vortex pairing and subsequent difussion of the coherent tip vortical cores[69].

In the near wake, the expansion of the wake leads to high velocity gradients which induce turbulent mixing. At the same time, viscous effects stretch the tip vortices (vortex stretching) and increase their sizes. As the leap-frogging and intertwining process continues, the vortex pairs are eventually smeared which is marked by the complete collapse of the coherent vortical structures. The breakdown of the tip vortices marks the start of the breakdown of the shear layer, where significant diffusion

occurs downstream. In Figure 3.8, it can be seen that that the onset of tip vortex instability increases the turbulent intensity of the flow field in the near wake.

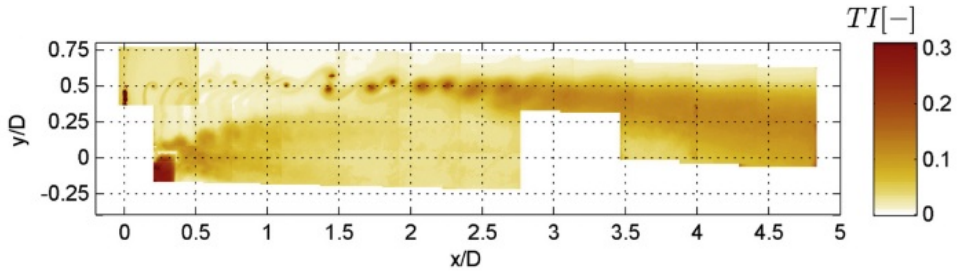

Figure 3.8: Axial Turbulent Intensity of the Wake of a 2 bladed rotor shwoing the phenomenon of the leap-frogging and subseuqent diffusion of the shear layer. In this experiment, the complete breakdown occurs at around $x/D = 2.5$ [37].

For easy reference, the length of the near wake is taken to be when the diffusion of the shear layer reaches the rotor axis (refer to Figure 3.1 for schematic). The wake edge (measured from the rotor axis) is conveniently taken to be the boundary where the flow first achieves the freestream velocity. For practical reasons, many experiments such as those in [37] and [36], the wake edge is taken to be points where the velocities are 99% of U_∞.

2 Effects of Ambient Turbulence

In the above analysis, the inflow velocity was assumed to be steady and uniform.

In reality, this would not be true as a wind turbine is operating in the atmospheric boundary layer and would thus, be subjected to ambient turbulence. Furthermore, there would be wind shear profiles due to the presence of the ground. The wind shear profiles would also vary due to the different orography and their corresponding roughness lengths in a given terrain. One should also not ignore the turbulent flow effects resulting from the the turbine components, especially the tower.

For lower ambient turbulence, the shear layer would tend to be stable over longer distances. This would lead to larger velocity deficits in the wake as there is less turbulence in the flow to induce momentum mixing.

The presence of the ground and the tower shadow effect also leads to the maximum point of the velocity deficit occurring below the turbine axis due to a lower incoming flow velocity. On the contrary, the velocity gradient is higher above the turbine axis which leads to a region of higher turbulent intensity. These effects are shown in the experimental and numerical computations of [65] and [57] (see Figure 3.9).

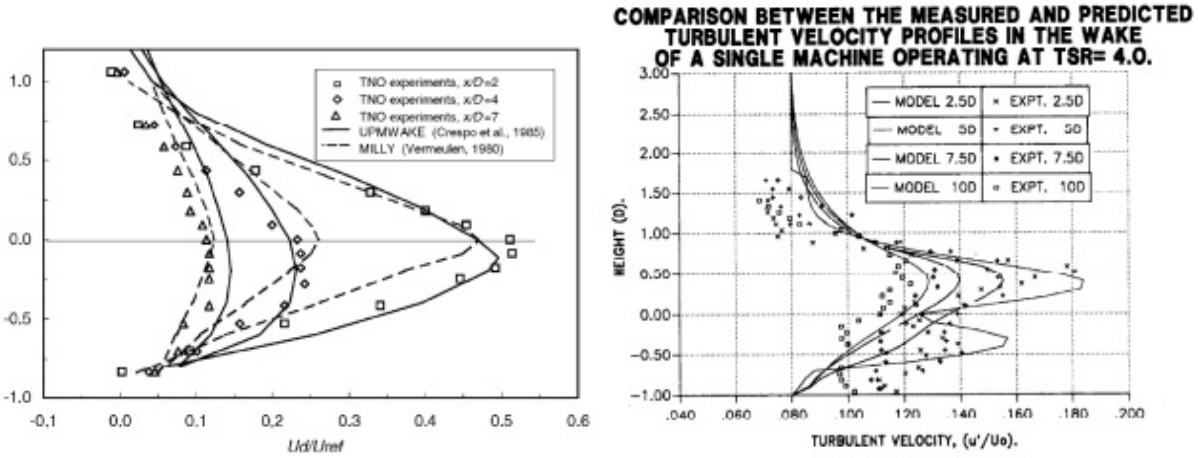

(a) Maximum velocity deficit occuring below the wake axis due to shear flow[65]

(b) Maxmimum turbulent intensity occuring above the wake axis due to higher velocity shear[57].

Figure 3.9: Effects on Velocity Deficity and Turbulent Intensity Profiles due to Shear Flow.

3 Far Wake

The start of the far wake region is marked by diffusion of the shear layer up to the turbine axis. After the shear layer has diffused entirely into the wake, this region is marked by smaller velocity gradients in the wake flow but is highly turbulent. The wake has now fully developed.

3.1 Wake Momentum Recovery

In the near wake, turbulent mixming and the diffusion of the shear layer has already started the momentum recovery process. In the far wake region, the flow velocity is no longer decreasing as the wake has fully expanded. The ambient and wake-induced turublence continues to drive the mixing of wake with the freestream and thereby, reduces the velocity deficit.

In several wind tunnel (such as [3] and [65]) and field experiements (such as [32]), the velocity deficit decay is largely dependent on the process of turbulent mixing. Lower ambient turbulence and rotors with low thrust (less wake-induced turbulence) leads to a more persistent wake profile.

3.2 Decay of Turbulent Intensity

In general, the wake's turbulence intensity decreases to the ambient value as the wake moves to the far downstream. The decrease of turbulence can be explained by the stretching of larger eddies into smaller ones. Through a process called Energy Cascade, the turbulent kinetic energy is transferred from large to small mircoscale eddies (see Figure 3.10). At the smallest length scale (also known as the Kolmogorov length scale η), viscous forces dominate over the inertia forces and the eddies are dissipated into heat.

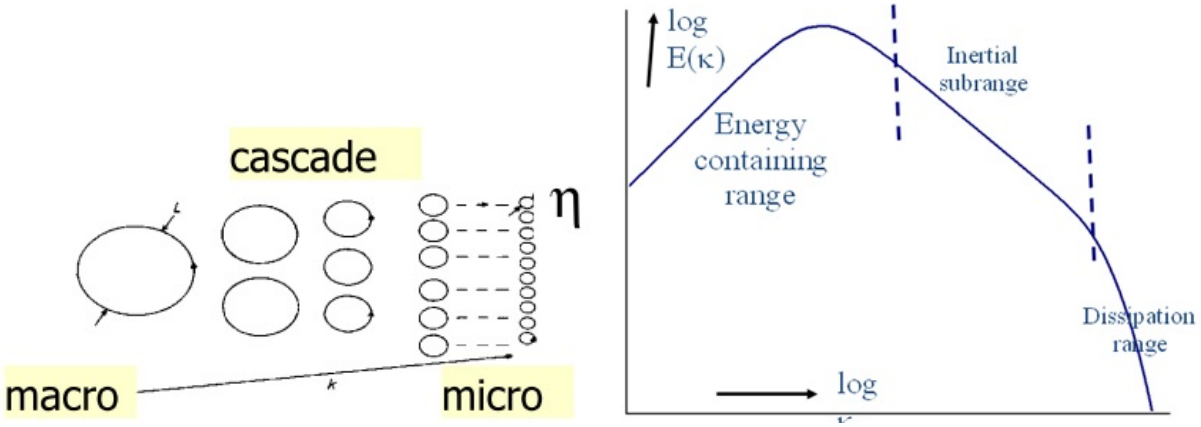

(a) Stretching of Eddies from macro to micro scales.

(b) Relationship between turbulent kinetic energy to the wavenumber (length scale).

Figure 3.10: Turbulent Kinetic Energy Cascade Process.

The persistence of the turbulent intensity of the wake is of concern as it increases the load fluctuations (frequency and amplitude) of the wind turbine structures. Load fluctuations result in fatigue loading which reduces the safe operational lifetime of the wind turbine structure.

4 Wind Farm Aerodynamics

The previous section has introduced the development of the far wake of a single rotor. Understanding the development of the far wake is important in wind farm planning in order to optimise power productions and alleviate fatigue loads. From a high power production and low fatigue loading perspective, it is desired to have widely spaced wind farms to obtain high velocity inflow with low turbulence conditions. However, sparsely spaced wind farms lead to higher cost of energy due to lower land usage intensity.

Several authors have studied the effects of several parameters on the development. These parameters that have been studied include the downstream distance [29, 28, 61, 51], thrust coefficient [46, 28, 61] and ambient turbulence [46, 65, 2]. Some of the experimental results have been translated into engineering models to be used to efficiently compute the wake properties.

In the case of offshore windfarms, the climate is characterised by low ambient turbulence due to relatively lower roughness lengths, leading to more persistent wakes. In general, the recovery of the velocity deficit occurs faster than the decay of turbulent intensity. Velocity deficit was observed to completely recover after 10D[5] while turbulent intensity was still relatively high even up to 15D.

By measuring the correlation between the velocity for several locations in a simulated windfarm cluster and the upstream value, [66] showed that the turbulence correlation between the wake of a turbine and that from the upstream machine remained fairly consistent after the first row and after multiple rows. This is attributed to the same rotor diameter interacting with the flow.

As aforementioned, turbulence in the flow results in fatigue loading on the turbines. The complex interactions between wakes of adjacent turbines further complicate the analysis. Generally, the turbulence level of the flow after interacting with a downstream turbine increases. This leads to the wake of a downstream turbine recovering faster than the one upstream due to better turbulent mixing. This point was corroborated by measurements in the UPWIND project on wind farms in Nysted and Hons Rev by [10]. In the study, the incremental energy loss between subsequent turbine decreases to

an asymptote (see Figure 3.11) and it was hypothesised that the turbulence level in a given windfarm can reach a saturation level.

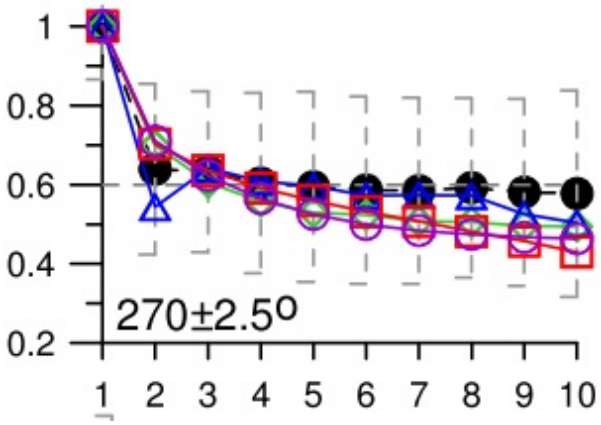

Figure 3.11: Normalised power of wind turbines reaching an asymptotic value after a few rows (x-axis)[10].

5 Wake Meandering

In many field and wind tunnel measurements, the wake of a wind turbine was found to be meandering. Wake meandering refers to oscillation of the flow strucure as it convects downstream.

5.1 Effects of Wake Meandering

The effects of wake meandering is meandering are two fold. Firstly, the meandering of the flow behind upstream turbines means the incoming flow is yawed on downstream turbines. From aerodynamic analysis, this yawed inflow leads to a periodic variation of the angle of attack on a blade depending on its azimuthal position. This time variation of the angle of attack leads to load fluctuation and therefore fatigue loads.

Secondly, because of the meandering, the low velocity wake is swept in and out of the rotor plane of the downstream turbine. From a theoretical sense, this reduces the velocity deficit and therefore increases power extraction. This effect has been corroborated by the reported measurements on wind farms in [34].

5.2 Von Karman Shedding

The physical process of the wind turbine wake meandering can be compared to the Von Karman sheet, which is a repeating pattern of swirling large scale vortices (compared to size of the wake) caused by unsteady flow separation around blunt bodies.

A characteristic of bluff body shedding is the self similarity state that is achieved downstream. Self similarity refers to the axis-symmetric properties of the flow. This shedding effect is usually associated with the non-dimensional Strouhal number St, which describes oscillating flow mechanisms, and is given by:

$$St = \frac{f_s D}{V_0} \tag{3.1}$$

The Strouhal number identifies the shedding phenomenon as a function of the body's aspect ratio. According to experimental analysis in [45], wake behind non-rotating discs has no preferred rotation pattern and f_s depends on the Reynolds number.

5.3 Wind Turbine Wake Meandering

For the same reasons, wake meandering is due to the unsteady separation of the vortices shed at the edge of the rotor plane. The laboratory results from [42] showed that wake meandering for a solid disc due to the ring vortices shed at the disc edge. This is similar to a wind turbine with an infinite number of blades or a wind turbine with a high tip speed ratio.

In [42], Medici also demonstrated that was a clear relationship between St and the tip speed ratio λ. At low tip speed ratios, no wake meandering (or no large scale vortex shedding) was observed (see Figure 3.12). On the other hand, the Strouhal number between disc and blade rotors were found to be very close at high tip speed ratios. This behaviour implies the flow increasingly sees the wind turbine as a solid disc as λ increases. At low λ, the flow does not see the blockage as a disc, but individual blades, which thereby does not give rise to periodic vortex shedding. It can also be said that the *effective* rotor diameter is smaller[41] at low λ, leading to higher St.

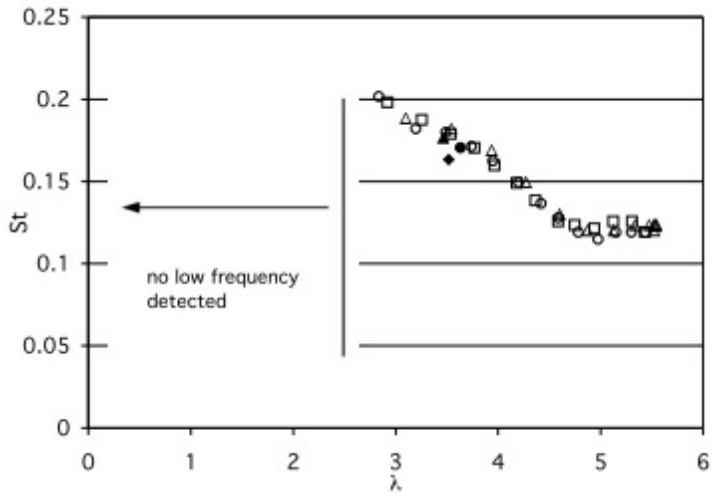

Figure 3.12: Relationship between the Strouhal number St and the tip speed ratio λ of the rotor[42]. Filled symbols represent data from the wind turbine, while unflled symbols represents disc with different porosities.

The study of the wake meandering effects is important as it can be seen that wake meandering may or may not be present depending on tip speed ratio (or the Reynolds number). This would present control strategies to avoid the wake of upstream turbines, so as to optimise the power production and alleviate fatigue loads.

Special mention is given to experimental works of Medici in [42, 41], as the results have showed clear presence of the tip vortex shedding and meandering. In [41], the contour plots of the streamwise or radial velocities in the temporal-spatial domain have shown periodicity in the cross-correlation values (see Figure 3.13). The respective signals were correlated with a reference probe that was positioned where the shedding and meandering phenomenon were clearly observed.

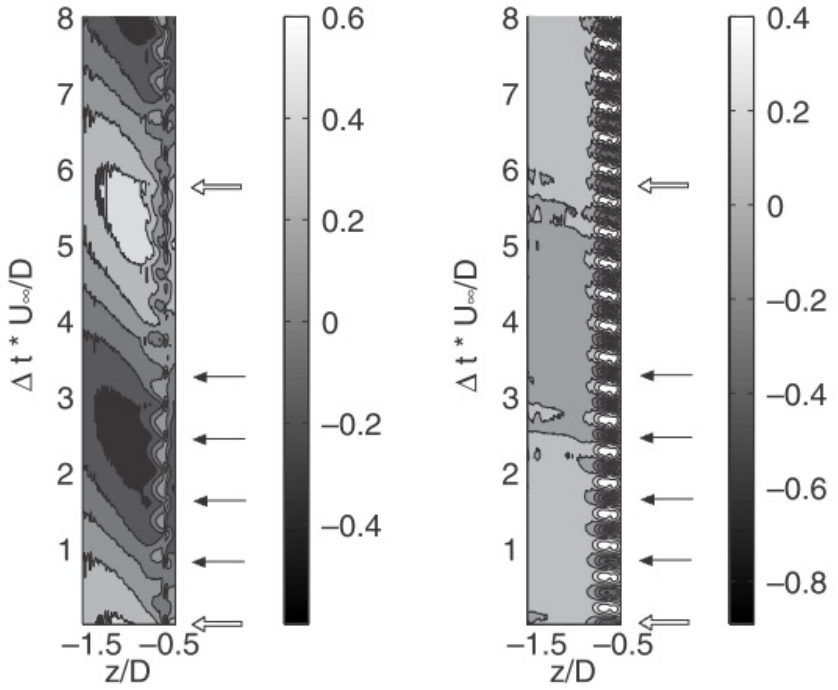

Figure 3.13: Contour plots of the cross-correlation between the streamwise (L) and radial (R) velocities in temporal and spatial domain[41]. The unfilled arrows and filled arrows mark the periodicity (found using spectral analysis) of the shedding of the large scale vortices and the rotation respectively.

"Science is like a love affair with nature; an elusive, tantalising mistress. It has all the turbulence, twists and turns of romantic love, but that's part of the game."

Vilayanur S. Ramachandran, 1951 -

4

Unsteady Rotor Aerodynamics

Since wind turbines operate close to the surface of the earth, the wind movement is affected by the surface roughness. The wind profile in this atmospheric boundary layer is usually non-uniform (wind shear) and can extend up to 200 m above ground[70]. Because of the fluctuating temperature on the earth's surface (e.g. day and night effect), the boundary layer is unstable and turbulent. Under such in-stationary wind conditions, wind turbines are almost always subjected to unsteady loads. In this context, it is important to examine the physics of unsteady rotor aerodynamics.

1 Wind Farm Planning

In a wind farm, wind turbines are sited in clusters at wind sectors with high levels of wind resource. During power generation operation, the power extraction from the wind causes a momentum deficit in the flow after the rotor, resulting in lower velocities than the free stream velocity (outside of the wake). Besides suffering from a velocity deficit, the turbulent nature of the wake increases fatigue load response.

In this context, the unsteady aerodynamics phenomenon in a wind farm are clearly apparent as downstream turbines are subjected to a highly fluctuating inflow. The amount of fluctuation due to the generated wake would depend on the spatial distance between turbines. It should also be noted that this spatial distance influences the rate of momentum recovery or re-energisation of the wake. Intuitively, for larger spatial distances, the momentum of the wake is likely to have recovered. Depending on the ambient and wake-induced turbulence, wake losses of between 20% and 25% have been observed at a distance of up to several tenths of the rotor diameter downstream in stable conditions[14]. It is therefore a fine balance or a trade-off between a tightly spaced layout in the windiest sector and a loosely spaced layout that extends into lower wind speed sectors, but experience less fatigue loads.

2 Unsteady Aerodynamics

The phenomenon of unsteady aerodynamics can classified into two types[58]: airfoil aerodynamics and dynamic inflow. The practical implications of unsteady rotor aerodynamics are two folds. Firstly, power production is unsteady, especially in yawed flow cases as there is variation of loads due to the varying angles of attck on the blade dependin on its azimuthal position. Secondly, there is increase in both fatigue and extreme loads due to the load variations. This effect further compels a higher cost of energy as the turbine specifications has to be scaled with a safety factor to assure operational safety.

While both effects of unsteady airfoil aerodynamics and dynamic inflow are independent and occur at different time scales ($\frac{c}{V}$ and $\frac{D}{V}$ respectively), it should be noted that the both effects are not mutually exclusive (as seen in experimental work such as [59]).

3 Concept of Flow Circulation and Bound Vortex

Unsteady profile or airfoil aerodynamics is related to the variation of the shed vorticity of a airfoil profile. Before this concept can be understood, the concept of flow circulation and bound vortex must be understood. Consider Figure 4.1, which shows real viscous flow around an airfoil with developed boundary layers.

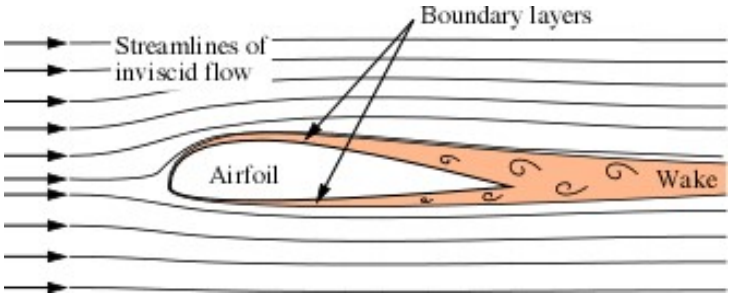

Figure 4.1: Inviscid flow around viscous boundary layer of an airfoil.

3.1 Circulation of an Airfoil

By mathematical definition, circulation Γ is the closed line integral of velocity over a closed path. In this case, we refer to a closed path around the airfoil.

$$\overrightarrow{\Gamma} = -\oint_l \overrightarrow{V} \cdot d\mathbf{l} \tag{4.1}$$

At this point, it should also be noted that the circulation term $\overrightarrow{\Gamma}$ can also be expressed in terms of vorticity ω (mathematically defined as the curl $\bigtriangledown$ of velocity $\overrightarrow{V}$) by using the results from Stokes's Divergence theorem. A closed surface $\overrightarrow{S}$ integral of the vorticity over the entire airfoil surface is

obtained as shown in Equation 4.2.

$$\begin{aligned}\overrightarrow{\Gamma} &= \oint_l \overrightarrow{V} \cdot d\mathbf{l} \\ &= \iint_S \bigtriangledown \times \overrightarrow{V} \cdot d\overrightarrow{S} \\ &= \iint_S \omega \cdot d\overrightarrow{S}\end{aligned} \tag{4.2}$$

3.2 Lift and Circulation

From the Kutta-Joukowski's theorem, the resulting aerodynamic lift of an airfoil is given by:

$$\overrightarrow{L} = -\rho\overrightarrow{\Gamma} \times \overrightarrow{U} \tag{4.3}$$

where $\overrightarrow{U}$ represents the velocity relative to (or seen by) the airfoil. The theorem describes that lift is proportional to the bound circulation at the airfoil.

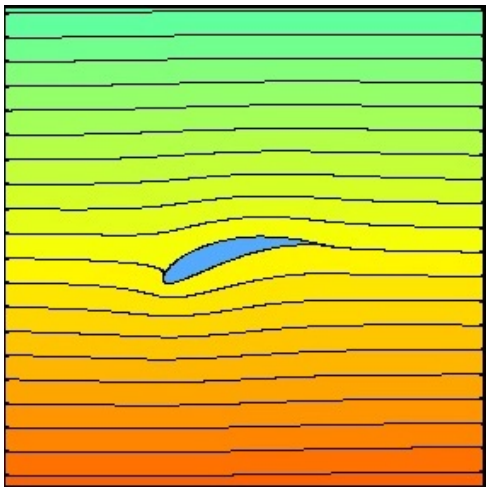

Figure 4.2: Stagnation Point on an airfoil. A circulation value that satisfies Kutta condition moves the rear stagnation point exactly to the trailing edge.

3.3 Starting Vortex

Considering the well known case of inviscid irrotational flow around a cylinder, there exists two stagnation points which lie on the centre line axis of the cylinder (see Figure 4.3).

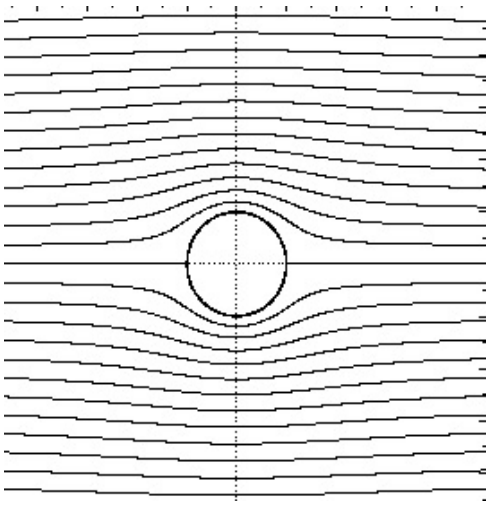

Figure 4.3: Inviscid and irrotational flow over a cylinder showing the Stagnation Points.

By similarity analysis, one would expect to find two stagnation points along the airfoil. If an airfoil with a sharp trailing edge begins to move with a positive angle of attack through air, the two stagnation points are initially located on the underside near the leading edge and on the topside near the trailing edge, just as what would be observed on a cylinder.

The following situation is now created: a seed particle on the lower side of the airfoil should travel along the airfoil profile, make a sharp U-turn at the trailing edge, go upstream on the upper face until it reaches the stagnation point and then, eventually, leave the airfoil towards the downstream. Vortex (circulatory) flow occurs around the trailing edge and because the radius of the trailing edge is small, the speed of the air particle would be very huge! The movement of air particles from the underside to the upper side of the profile are met with adverse pressure forces (due to the fluid's viscosity). The strong vortex which accumulates on the upper side near the trailing edge is known as the starting vortex which forms very quickly during the start-up process (i.e. the movement from the initial to next α position).

3.4 Kelvin Circulation Theorem

According to Kelvin Circulation Theorem, the total net circulation around a closed loop is independent of time. In the case of an airfoil initially in static flow, the total net circulation in a path enclosing the airfoil must be zero.

In the case of the airfoil considered here, as the starting vortex increases in strength at the trailing edge during the start-up process, there must a corresponding increase in the strength of the bound vortex in order to satisfy Kelvin's Theorem. The bound vortex results in the flow over the topside of the airfoil to increase in speed.

From this theorem, it apparently seems that the strength of the circulation Γ can be assigned arbitrarily since Kelvin theorem will be satisfied. However, the following Kutta Condition principle would also have to be satisfied.

3.5 Kutta Condition

In steady flow dynamics, the Kutta condition is a principle which states:

> *"A body with a sharp trailing edge which is moving through a fluid will create about itself a circulation of sufficient strength to hold the rear stagnation point at the trailing edge."*
>
> - Kuethe and Schetzer, *1959*

The position of the stagnation point is determined by the strength of Γ of the airfoil profile. There is a particular value of Γ that moves the rear stagnation point exactly on the trailing edge. For a stagnation point to exist at the trailing edge, the velocity on the upper and lower surface of a sharp or cusped edge must be leaving parallel to each other. This means that the stagnation point must exist on the trailing edge in order for a stagnation point to exist.

To satisfy Kutta condition, the bound vortex will move the stagnation point in tandem on the upper side of the airfoil until it reaches the trailing edge where the flow over the upper and lower side leave parallel to one another. Once the stagnation has moved to the trailing edge, the strong adverse pressure force disappears and the magnitude of the circulation of the bound and starting vortex has reached a maximum.

In fluid flow around a body with a sharp corner, the Kutta condition describes the flow pattern in which fluid approaches the corner from both directions, meets at the corner and then flows away from the body. None of the fluid flows around the corner and remains attached to the body. The Kutta condition is significant when using the Kutta-Joukowski theorem to calculate the lift created by an airfoil with generally cusped trailing edge. This requires a unique value of Γ which satisfies both Kelvin and Kutta condition - not just any arbitrary value. The airfoil now has a finite value of the bound vortex (equal to the strength of the starting vortex) and the steady lift value is computed by Equation 4.3.

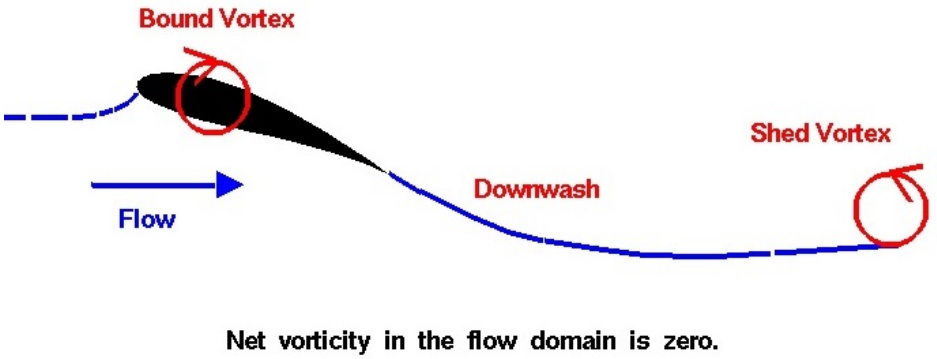

Figure 4.4: Schematic depicting the bound and shed vortex of an airfoil.

As the airfoil moves forward, the starting vortex is cast behind the airfoil, spinning in the air where the airfoil left it (see Figure 4.4). The starting vortex continues induce a velocity at the airfoil (therefore changing the relative velocity V_{rel}) until it has been casted at a far distance behind or has been eventually broken down (energy cascade and vortex stretching) and finally dissipated through heat due to viscosity.

4 Unsteady Profile Aerodynamics

Extending the argument from the previous section, unsteady profile aerodynamics refer to the time-variation of the shed vorticity (starting vortex) of the airfoil, which directly leads to an unsteady variation of the bound vortex.

From Figure 4.4, it can be seen that a starting vortex is formed whenever there is a change in the flow speed or angle or attack. This starting vortex and a new equilibrium for the bound vortex has to be re-established to satisfy both Kelvin theorem and Kutta condition. In highly unsteady flow, this would mean constant shedding of new starting vortices in response to the change in circulation. There is an associated time response to these imposed α changes and is therefore known to be the unsteady profile aerodynamics.

The shed vorticity is transported by V_{rel} with a characteristic length scale of the chord c. This results in the time scale of unsteady profile effects in the order of $\frac{c}{V_{rel}}$.

4.1 Dynamic Stall

As the angle of attack of the flow on an airfoil increases, the boundary layer starts to separate from the walls of the airfoil due to increasing adverse pressure gradients. Flow separation occurs further upstream with higher angles of attack. Dynamic Stall refers to the delay of this conventional flow separation on wings and airfoils caused by rapid variations in the angle of attack beyond the critical static stall angle due to the unsteady motion[19].

In viscous flow, the flow over the airfoil is prone to boundary layer separation at increasing angles of attack due to adverse pressure gradient especially at the walls as a result of viscous shearing.

Consider a situation when the angle of attack increases from below to above stall behaviour, the airfoil exhibits for a short time some of the previously unstalled lift which leads to an overshoot in the time evolution of the lift profile. Therefore, if dynamic stall effects are not considered, one might still expect flap-wise vibrations for stall regulated wind turbines, which are likely non-existent on a well-designed turbine[30].

4.1.1 Dynamic Stall Vortex and Lift Overshoot and Decay

Under stall conditions, the airfoil is known to operate under the detached viscous flow conditions. At the beginning of a sudden upward pitching, an increase in lift generated by the airfoil's suction side during the airfoil sudden pitch-up is associated with the formation of the Dynamic Stall Vortex (DSV). This leads to an abrupt overshoot of the lift due to accumulation of vorticity at the leading edge as the angle of attack increases[21].

The subsequent downstream convection of the DSV leaves behind a region of separated flow which corresponds to the reduction of the lift. The Theodorsen function also serves to explain this phenomenon. At the beginning of the sudden pitch-up motion, there is an increased apparent thickness of the airfoil. This increase in airfoil thickness would explain the corresponding decay of the lift polar.

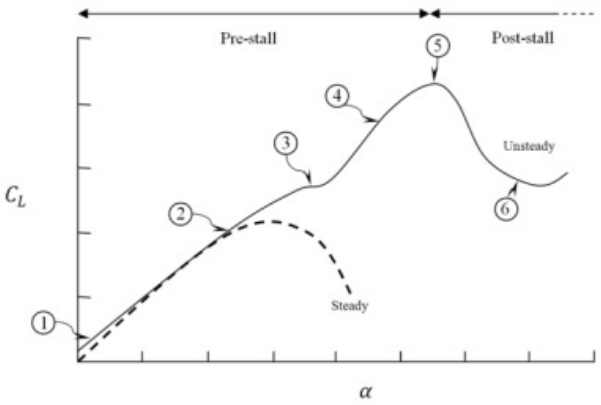

Figure 4.5: Example of the characteristics of a unsteady ramp-type dynamic stall [21]. The dash lines refer to steady test data and the solid lines are the predicted response behaviour in unsteady conditions.

Onset

The initial jump is the impulse pitch up motion of the airfoil which forms a strong vorticiy (starting vortex) at the leading edge. This starting vortex induces significant amount of local velocity and causes a temporary lift spike at the onset (but still lower than the steady value). This starting vortex is convected downstream and its influence decreases which leads to an exponential decay towards the steady state value.

This predicted behaviour also corresponds with the famous `Wagner` function $\phi(t)$, which is a quasi-steady model used to predict the lift response at the quarter chord of an airfoil following a indicial (step) change in the angle of attack:

$$\Delta L = \frac{1}{2}\rho V_{rel}^2 c c_{l,\alpha} \Delta\alpha \phi(\tau) \tag{4.4}$$

where c, $c_{l,\alpha}$ and $\Delta\alpha$ refer to the chord length, quasi-steady lift slope and the step change in angle of attack. w is the downwash contributed by the starting vortex and is sinusoidally proportionate to $\Delta\alpha$ by $w = Vsin(\Delta\alpha) \approx \Delta\alpha$. τ is no of half-chords travelled or the non-dimensional time defined as $\tau = \frac{Vt}{c/2}$. It is proposed by [25] that for incompressible flow, that the Wagner function is given by:

$$\phi(\tau) = 0 \quad \text{where} \quad \tau < 0 \quad \text{and} \quad \phi(\tau) = \frac{\tau + 2}{\tau + 4} \quad \text{where} \quad \tau \geq 0 \tag{4.5}$$

At $t = 0$, with $\phi(\tau) = \frac{1}{2}$, `Wagner` function predicts a jump in lift to be half the quasi-steady value. As τ increases, `Wagner` shows that the lift gradient decays exponentially. This behaviour can be described by a hysteresis loop on the polar curve where there is a high lift coefficient on the upstroke (increase of angle of attack) and a low lift coefficient on the down stroke.

In Figure 4.5, the unsteady response of a particular airfoil under non-stall and stall conditions is shown. It is seen that the range of the response under dynamic stall is much larger. This undesirable behaviour results in more loads fluctuation and lead to higher fatigue loading. At stall conditions, the effects become more complex due to flow separation as the airfoil operates between attached and detached flow conditions. Dynamic stall is therefore also synonymous with airfoil aerodynamics which is characterised by a hysteresis loop on the polar lift.

4.2 Modelling Unsteady Profile Aerodynamics

Theodorsen was one of the pioneers to model unsteady airfoil aerodynamics. His classical model was used to describe the profile of a 2-D airfoil and the vorticity is presented by infinitely long vortex lines.

Dynamic stall effects are often expressed as ordinary time-dependent differential equations. More recently, [13] expressed the dynamic stall effects as a correction to the steady state lift coefficient given in Equation 4.6

$$\tau \frac{dc_l}{dt} + f(\alpha)\dot{c}_l = f(c_l, \alpha, \frac{d\alpha}{dt}, \frac{d^2\alpha}{dt}) \tag{4.6}$$

5 Dynamic Inflow

MT assumes that the induced velocity responds instantaneously to the change in flow situation (e.g. change in inflow velocity or rotor's blade pitch angle). This is also called assumption of equilibrium wake for steady flow situations[54].

5.1 Flow Physics

Dynamic inflow is related to the unsteadiness of the inflow velocity V_0 which has been affected by the resulting wake. There is an associated time lag in the induction of the flow in the wake as a finite mass of air must be accelerated or decelerated in reponse to the change in inflow velocity. Besides being termed as Dynamic Inflow, this class of unsteady phenomenon is also known as dynamic wake or dynamic induction due to the aforementioned effects.

Besides Dynamic Inflow (caused by e.g. turbulence, gust), this unsteady phenomenon would also be present in situations such as sudden blade pitch or wind direction which would indirectly affect the steadiness of the perceived inflow.

The unsteadiness of the induction is caused by shedding of the 'new' vortices from the aerodynamic body and convected by the freestream. Since the size of the shed vortices is related to the size of the problem, this gives rise to the characteristic length scale of the rotor diameter D, which gives a characteristic timescale in the order of $\frac{D}{V_0}$. To illustrate the preceding explanation, the convection of the 'new' vortices in the presence of the 'old' vortices can be seen in Figure 4.6 during the period of the unsteadiness. Due to unsteady inflow, there is a change in the strength of the bound vortex and therefore the shed vortex (Kelvin's theorem). This change (in the dynamic inflow time scale) results in the influence of both 'old' and 'new' shed vortices on the flow field and hence the name, dynamic induction. The induced velocity W at the rotor plane experiences a gradual change, until the 'old' vortices has been convected far downstream and in its place, replaced by the 'new' vortices. In this described process, there is therefore an associated time lag before the induced velocity is changed to the new state (accelerated or decelerated).

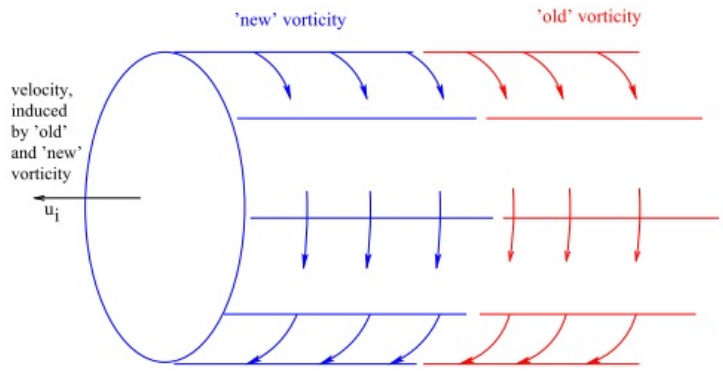

Figure 4.6: Dynamic Inflow effect: Effect on 'old' and 'new' vorticity as a result of a transient change in C_T [54].

5.2 Previous Experimental Work

Several wind tunnel tests have captured the effects of dynamic inflow - notably in [58], Snel and Schepers performed extensive experiments. In this reference, it was found that dynamic inflow effects were most apparent during unsteady loading on the rotors ; sudden changes in blade pitch for bladed rotors were used to observe dynamic inflow. The effects of induction delay were seen in those measurements and the physics of the phenomenon have been explained in the preceding paragraphs.

It is also interesting to note that in dynamic inflow experiments or numerical simulations[59] on blade rotors, a temporary spike of the loads before a subsequent decay to the steady state loads was recorded. An example of this behaviour is shown in Figure 4.7 where the temporary overshoot in loads is due to the unsteady profile aerodynamics.

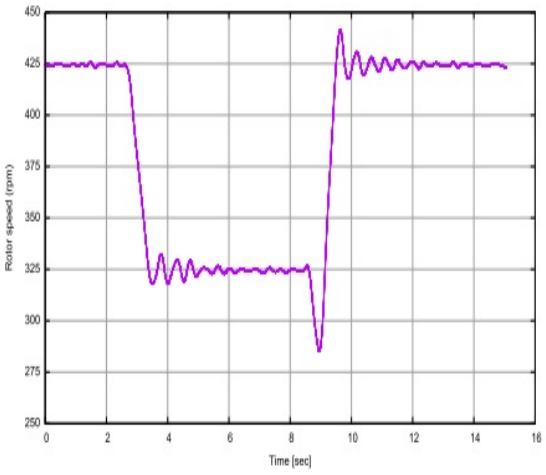

(a) Input: Sudden change in Rotor RPM.

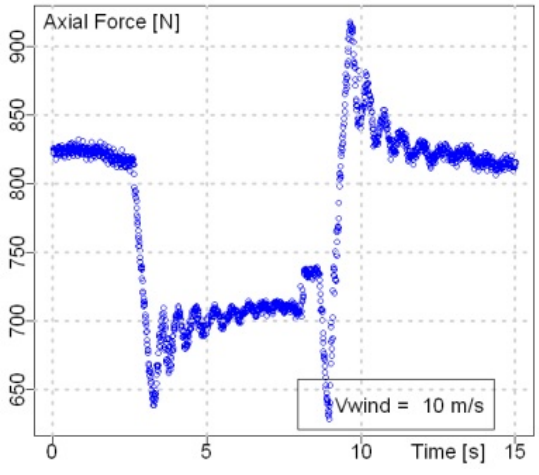

(b) Output: Axial force response recorded by the load cell located at the tower bottom.

Figure 4.7: Experiment Results from Dynamic Inflow experiments on the MEXICO Wind Turbine[54].

From the results of previous works, it seems that is hard to decouple the unsteady effects of airfoil profile aerodynamics and dynamic flow even though the characteristics time scales are different. The impulse rotation (or pitch movement) results in the formation of a strong impulse vortex at the leading edge. This strong impusle vortex accelerates the local velocity, which indirectly causes a spike in the aerodynamic load. The subsequent decay of the load to the steady state value is due to

the convection (or decay) of this impulse vortex and the time delay in the propagation of the 'new' shed vortices.

Under circumstances such as gust and pitch control where the time scale of the unsteadiness is of the order $\frac{D}{V_0}$, there is a time lag before the induced velocity at the rotor plane is adjusted to the new loading state. From this perspective, dynamic inflow effects would be very relevant for large rotor turbines.

In chapter 2, it has been explained that MT inherently assumes an equilibrium wake state. In other words, a pure AD model assumes quasi-steady aerodynamics to analyse the aerodynamic response. This is a convenient assumption taken by many of the current engineering models. The use of quasi-steady assumption allows momentum equilibrium between the up- and downstream sections at any time instance between the new loading state and the induced velocity. This assumption maybe valid when the time scale of the load change is much larger than $\frac{D}{V_0}$ and therefore, the uncertainty in the load prediction maybe acceptable.

According to [58], clear dynamic infow effects were observed from rapid blade pitch steps with corresponding unsteadiness time scale of between 0.3τ and 0.5τ. These effects would be more distinct and significant as the Reynolds number increase (larger turbine) or when the time scale of the unsteadiness is longer.

5.3 Dynamic Inflow Engineering Models

Engineering models refer to methods that give results which are similar to those based on the fundamental physics principles. They are usually based on laws governing momentum, mass and energy, or empirical data, or a combination of both. There are many engineering models which can be largely distinguished by their applicability for different flow situations. In fact, the BEM model that has been described can be considered as an engineering model. The distinction of the spectrum of methods to solve the fluid dynamics: between engineering models and solving the governing Navier-Stokes (NS) equations is depicted in Figure 4.8. The NS equations govern the fluid dynamics which are resolved through the partial differential equations. However, solving the general NS equations requires a huge investment of computational resources. Even with relative cheaper alternatives approaches like LES and RANS, the investment is still significant. Therefore, instead of running costly experiments or computationally expensive numerical simulations, the industry's preference is usually engineering models as the results give reasonable estimates of the fluid dynamics within reasonable computational time.

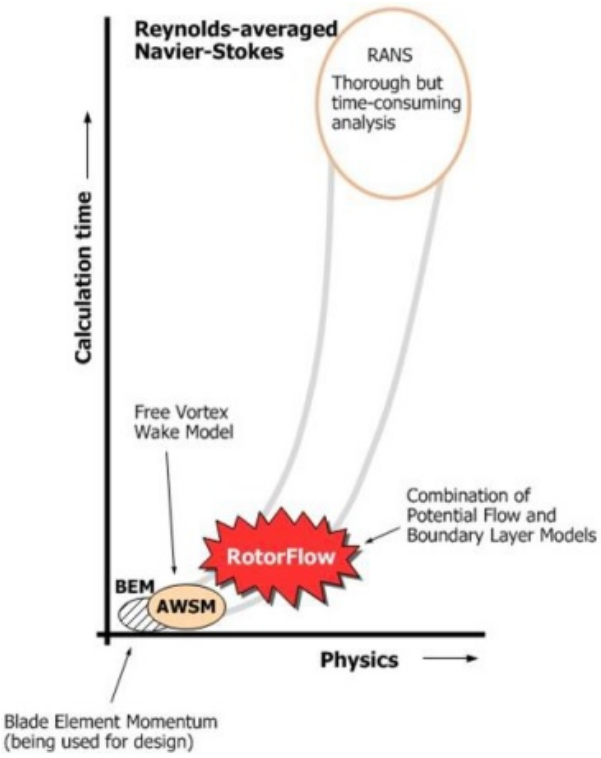

Figure 4.8: Spectrum of methods between Engineering Models and CFD to analyse fluid dynamics[54].

Engineering models have also been developed to predict the fluid dynamics under dynamic inflow conditions. Mention is given to the EU JOULE program under which a project led by Snel[58] was conducted with the aim to account for dynamic inflow effects in the BEM model. Results from this project have been prominent in furthering the research in dynamic inflow effects. The project had investigated, implemented and validated dynamic inflow models in order to capture the time-varying inflow velocity at the rotor plane. This was done by field measurements of the Tjaereborg 2MW wind turbine (3-bladed) and wind tunnel data from a 1.2 m diameter 3-bladed rotor.

General Modelling Approach

The steady BEM model is used when the inflow is steady. To model effects of dynamic inflow, the response is relaxed with time. The unsteady response is accounted in the momentum relations with a time-dependent term, similar to unsteady airfoil aerodynamics. In [54], it is suggested that the associated aerodynamic time decay constant τ is inversely related to the radial distance and increases with rotor diameter.

5.3.1 Pitt-Peters

In 1953, Carpenter et al.[18] developed a dynamic inflow model to characteristic the effect of a rapid blade-pitch increase on the thrust and induced velocity response of a helicopter rotor. Their work has been further improved and forms the basis of the dynamic inflow model developed by [49] and presented in [58]. The model is premised on the actuator disc model and has been implemented in the aerodynamic codes of commericial aeroelastic computation software such as `GH Bladed` and `AeroDyn`. Application of this model allows radial variation of the force and induced velocity which is a much more realistic.

Consider a rotor disc divided into k independent annular rings, the dynamic response of the thrust T can be related to the induced velocity $V_{i,k}$ and axial velocity $V_{z,k}$ of the annulus ring k, which is located at a radius r with an area A_k (see Equation 4.7).

$$\begin{aligned} T &= \text{Dynamic Term} + \text{Steady Term} \\ &= \frac{8}{3\pi}\rho A_k r_k \frac{dV_{i,k}}{dt} + 2\rho A_k V_{i,k} V_{z,k} \end{aligned} \tag{4.7}$$

Implementation Approach - Backward Difference Discretisation

Since the problem is a an actuator disc with uniform loading, the complexity of non-uniformly loaded annulus rings is avoided. By a backward difference discretisation of Equation 4.7, the dynamic induced velocity can be obtained in the following:

$$\begin{aligned} T &= \frac{8}{3\pi}\rho A r \frac{W^i - W^{i-1}}{\Delta t} + 2\rho A W^i V_x^i \\ \iff W^i &= \frac{1}{2} \cdot \left[V_0 + \frac{4r}{3\pi\Delta t} - \sqrt{\left(\frac{4r}{3\pi\Delta t} + V_0\right)^2 - \frac{16r}{3\pi\Delta t} W^{i-1} - C_{T,qs} V_0^2} \right] \end{aligned} \tag{4.8}$$

where the superscript i represents the time instance and $C_{T,qs}$ is the input loading.

5.3.2 S. Øye

The model proposed by Øye[47] computes the dynamic response of the induced velocity W by passing the quasi-steady values W_{qs} through two 1st order, linear, ordinary differential equations (ODEs).

$$W_{int} + \tau_1 \frac{dW_{int}}{dt} = W_{qs} + k \cdot \tau_1 \frac{dW_{qs}}{dt} \qquad \text{where} \quad \tau_1 = \frac{1.1}{1 - 1.3a} \cdot \frac{R}{V_0} \tag{4.9}$$

$$W + \tau_2 \frac{dW}{dt} = W_{int} \qquad \text{where} \quad \tau_2 = \left[0.39 - 0.26\left(\frac{r}{R}\right)^2\right] \tau_1 \tag{4.10}$$

where $k = 0.6$, tuned from a vortex ring model[47]. In Equation 4.9, the values of W_{qs} are found by the steady BEM model, in order to compute W_{int} (an intermediate computation value). W_{int} is given as an input in Equation 4.10, to finally compute the response of the induced velocity at each time instance W^i. At each time step, W_{qs} is updated to compute the corresponding W. In this way, the dynamic response is computed where the time delay associated with a change in the wake state is taken into account.

Implementation Approach 1 - Assuming constant RHS

To obtain the response of W at each time instance (denoted by superscript i), known analytical solutions of ordinary differential equations can be used. The solution approach described here is similar to [30]. To solve the first order ODE, we first express Equation 4.9 in the general form:

$$\frac{dW_{int}}{dt} + \frac{1}{\tau_1} W_{int} = \frac{RHS}{\tau_1} \tag{4.11}$$

where the RHS is *estimated* using a backward differencing scheme as shown:

$$RHS \approx W_{qs}^{i} + k \cdot \tau_1 \frac{W_{qs}^{i} - W_{qs}^{i-1}}{\Delta t} \tag{4.12}$$

The associated integrating factor $\mu(t)$ for the ODE (Equation 4.11) is therefore:

$$\mu(t) = e^{\int \frac{1}{\tau_1} dt} = e^{\frac{t}{\tau_1}} \tag{4.13}$$

Multiplying Equation 4.13 to Equation 4.11, this results in:

$$\begin{aligned}
& e^{\frac{t}{\tau_1}} \cdot \frac{dW_{int}}{dt} + \frac{e^{\frac{t}{\tau_1}}}{\tau_1} W_{int} = e^{\frac{t}{\tau_1}} \cdot \frac{RHS}{\tau_1} \\
\iff \quad & \left(e^{\frac{t}{\tau_1}} \cdot W_{int}\right)' = e^{\frac{t}{\tau_1}} \cdot \frac{RHS}{\tau_1} \\
\text{Integrating w.r.t. } t \implies & \int \left(e^{\frac{t}{\tau_1}} \cdot W_{int}\right)' dt = \int \left(e^{\frac{t}{\tau_1}} \cdot \frac{RHS}{\tau_1}\right) dt \\
& e^{\frac{t}{\tau_1}} \cdot W_{int} = \frac{RHS}{\tau_1} \cdot \tau_1 e^{\frac{t}{\tau_1}} + C \\
& W_{int} = C e^{-\frac{t}{\tau_1}} + RHS
\end{aligned} \tag{4.14}$$

To compute the integrating constant C, we consider the $(i-1)^{th}$ and i^{th} time instances to have:

$$(i-1)^{th}: \quad W_{int}^{i-1} = C e^{-\frac{t^{i-1}}{\tau_1}} + RHS \tag{4.15}$$

$$\implies C = \frac{W_{int}^{i-1} - RHS}{e^{-\frac{t^{i-1}}{\tau_1}}}$$

$$\begin{aligned}
i^{th}: \quad W_{int}^{i} &= C e^{-\frac{t^{i}}{\tau_1}} + RHS \\
&= \frac{W_{int}^{i-1} - RHS}{e^{-\frac{t^{i-1}}{\tau_1}}} \cdot e^{-\frac{t^{i}}{\tau_1}} + RHS \\
&= \left(W_{int}^{i-1} - RHS\right) e^{\frac{-\Delta t}{\tau_1}} + RHS
\end{aligned} \tag{4.16}$$

Similarly, from Equation 4.10, by treating the right hand side as a arbitrary constant, the corresponding analytical expression at a given time instance is derived as:

$$W^{i} = \left(W^{i-1} - W_{int}^{i}\right) e^{\frac{-\Delta t}{\tau_2}} + W_{int}^{i} \tag{4.17}$$

The unknown W^i can then be found by substituting Equation 4.16 into Equation 4.17.

Implementation Approach 2 - Backward Difference Discretisation

Alternatively, W can be found by discretising all the 1st order derivatives using the backward difference scheme. This is done as shown in the following:

(a) Compute the quasi-steady induced velocity W_{qs}^{i} using MT.

(b) To obtain W^i_{int}, the backward difference scheme is applied on Equation 4.9 to obtain:

$$\begin{aligned} W^i_{int} + \tau_1 \frac{W^i_{int} - W^{i-1}_{int}}{\Delta t} &= W^i_{qs} + k\tau_1 \frac{W^i_{qs} - W^{i-1}_{qs}}{\Delta t} \\ \iff \left(1 + \frac{\tau_1}{\Delta t}\right) W^i_{int} - \frac{\tau_1}{\Delta t} W^{i-1}_{int} &= W^i_{qs} + k\tau_1 \frac{W^i_{qs} - W^{i-1}_{qs}}{\Delta t} \\ \iff W^i_{int} &= \frac{\frac{\tau_1}{\Delta t} W^{i-1}_{int} + W^i_{qs} + k\tau_1 \frac{W^i_{qs} - W^{i-1}_{qs}}{\Delta t}}{1 + \frac{\tau_1}{\Delta t}} \end{aligned} \tag{4.18}$$

(c) W^i is found by substituting W^i_{int} using Equation 4.18 and similarly applying the backward difference scheme on Equation 4.10.

$$\begin{aligned} W^i + \tau_2 \frac{W^i - W^{i-1}}{\Delta t} &= W^i_{int} \\ \iff \left(1 + \frac{\tau_2}{\Delta t}\right) W^i - \frac{\tau_2}{\Delta t} W^{i-1} &= W^i_{int} \\ \iff W^i &= \frac{\frac{\tau_2}{\Delta t} W^{i-1} + W^i_{int}}{1 + \frac{\tau_2}{\Delta t}} \end{aligned} \tag{4.19}$$

6 Vortex Methods

Using vortex to model the wake field of rotors is increasingly popular due to its reliability and straightforward implementation and has been adopted by many authors to study rotor aerodynamics. A comprehensive review can be found at [60]. Vortex methods describe the transport of vorticity and is essentially the computation of the velocity at a given point in space and time using the Bio-Savart law:

$$V(x_i, t) = \frac{1}{4\pi} \int \frac{\omega_i(x'_i, t) \times (x_i - x'_i)}{|x_i - x'_i|^3} dx'_i \tag{4.20}$$

Using Equation 4.20, by vectorial summation of the influence of all other vortex particles, the local velocity of a vortex particle can be computed. Subsequently after a time step Δt, the said vortex particle would have been transported by this local velocity. The calculations are then repeated for more timesteps for all particles in to gain knowledge on the velocity field. Some vortex models also include corrections on the vorticity ω in order to account for viscous dissipation or vortex stretching effects. A key challenge for vortex models is the quadratic increase in computation effort as N vortex particles would require $\mathcal{O}(N^2)$ calculations in a time step. A strategy to overcome this is to prescribe a threshold distance, whereby the influence of vortex particles beyond a certain distance is ignored[20].

6.1 Free Wake Vortex Ring Model

The free wake vortex ring model (FWVR) developed in [71] is one such vortex model to compute the transient reponse of the wake field and the velocity at the inflow plane of a actuator disc rotor. The model setup combines the influence of singular vortex particles (or rings) in the near wake, with a semi-infinite cylindrical vortex tube for the far wake (to prevent excessive computation resource). Discrete vortex particles are released (or shed) when the local pressure gradient along the radial direction is non-zero. For an uniformly loaded rotor, the vortex rings are shed at the edges (see Figure 4.9). The

magnitude of the vorticity is then evaluated through an expression[62], which accounts the pressure jump across the rotor. In a time-marching scheme, the velocity in the wake field and at the rotor plane can be resolved.

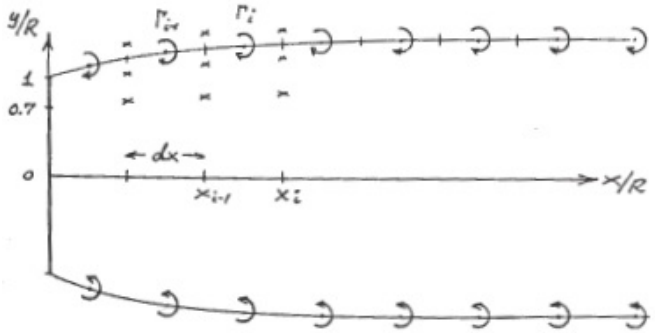

Figure 4.9: Modelling of an actuator disc rotor's near wake by singular vortex rings[48].

Part II: CFD Simulations

"The purpose of computing is insight not numbers."
C. Hastings, 1955 –

5

Overview of Computational Fluid Dynamics

The aim of Computational Fluid Dynamics (CFD) is to compute the solution of a fluid dynamics problem. The solution is known as a 'numerical solution' because it is obtained by solving the flow-governing Navier-Stokes equations.

1 Navier Stokes Equations

It is widely accepted that the solution of the famous Navier-Stokes (NS) equations quite accurately predict fluid behaviour. The derivation of the NS equations from first principles inherently describe fluid dynamics in a continuum. This means that flow variables (i.e. velocity v and pressure p) can be defined as every point in the domain. However, as it is known from chemistry, fluid is in reality, a collection of discrete molecules packed closely i.e. fluid is not exactly a continuum. The continuum assumption, however, is still very reasonable, as the solution is still rather reliable. By nature, fluid motion is highly unsteady, fluctuating, three-dimensional, rotational, dissipative and diffusive all at any one time. Therefore, the NS equations are partial differential which are elliptic, highly non-linear and coupled (pressure-velocity).

2 Art of CFD

The strategy in CFD is to solve the NS equations by representing the continuous flow domain in a discrete manner. The domain is represented or discretised by a grid or a mesh. Discretisation techniques reduce the set of complex partial differential equations into simpler algebraic equations (become a matrix inversion problem). Although algebraic equations are relatively easier to solve, there are just too many repetitive calculations (quantity of repetitions depends on mesh density). This is why CFD is always performed by computers. The flow variables are resolved at grid points (or called nodes) while values at non-grid points can be found by interpolation.

In the course of doing this research, it was appreciated that implementing CFD is an art. This is said so, as obtaining reliable and accurate simulation results requires the user to make appropriate and informed choices on the methods to be applied. More often than not, an experienced CFD user has to

have a feel or knowledge on certain issues such as the mesh density, meshing technique, selection of the physics solver etc, in order to obtain an accurate solution with realistic computational resources.

The process of CFD is akin to a painting artist who has a palette of colours to choose (physics solver), type of drawing paper in order to accentuate the features of his final art (mesh type and density) and drawing techniques - depending on the part that is being drawn (time step and physics solver).

3 Physics Solvers

Physics solvers refer to the different technique used to solve the discretised NS equations. Each technique comprises of:

(a) the manner by which the governing equations are discretised or how the values at the grid points are computed (e.g. upwind or central differencing)

(b) time-marching scheme - whether explicit or implicit. The physical time step is indicate the development or progress of the flow over time. Using the Nyquist criterion, to sufficiently capture the transient phenomenon in unsteady flows, two or more time steps per period are required.

An explicit solver calculates the state of a system at a later time from the current state. An explicit time marching scheme does not involve local time stepping as each iteration represents the time-accurate advancement of the solution. This would thus require the minimum allowable time step that satisfies the Courant condition everywhere in the domain, which means long computation times as the physical time step would be very small.

An implicit solver calculates the solution by solving an equation involving both the current state of the system and the later one. It therefore requires more memory but is a rather stable solver, where the Courant-Friedrichs-Lewy (CFL) value can be more than 1. This allows a large local timestep (inner iterations) for a given time instance. Implicit solvers are usually applied for unsteady problems due to their stability.

(c) solving the unknown quantities (p and v) in a segregated or coupled approach.

A Segregated or un-coupled solver solves the flow equations (one for each component of velocity, and one for pressure) in a separate manner. This is done using the SIMPLE (Semi-Implicit Method for Pressure-Linked Equations) algorithm, where the linkage between the momentum and continuity equation is achieved through a predictor-corrector approach. The pressure distribution term is implicitly solved through an iterative approach by first approximating the velocity field from the previous iteration or an initial guess. With the pressure distribution known, the velocity terms are then explicitly obtained by correcting with the new pressure distribution. This is this reason why the algorithm is called a Semi-Implicit Method.

In an opposite sense, the Coupled approach solves the coupled system (pressure and velocity) of equations simultaneously. A coupled algorithm approach yields more robust and accurate solution and is recommended for compressible flow. However, it should be noted that the Coupled approach uses significantly more memory and computational power.

Each of the above selection has its own implication and has been researched thoroughly. It is not the aim of this report to explicitly discuss their features but to merely highlight the key features and purposes.

4 Meshing

Even with an appropriate physics solver, no reliable solution can be achieved without a suitable mesh or grid to represent the fluid domain. As mentioned, the approach of CFD is to represent a continuous fluid domain problem with a discrete mesh. A mesh grid is the discretised representation of the volume domain on which the physics solvers are used to provide a numerical solution. A poor quality mesh usually means the the flow especially around complex geometries are not correctly represented. Although it does not necessarily result in solver run time problems, this means the accuracy and efficiency (computation time) of the solution is affected.

4.1 Meshing Guidelines

The construction of the volume mesh has a direct influence on how the fluid flow and energy is simulated. The shape and size of the mesh grid also influences the rate of convergence and the accuracy of the final solution. In general, the following guidelines will apply to a volume mesh.

(a) A mesh should have adequate resolution in regions where spatial gradients are high. Such situations can occur in the following situations where:

- the mean flow changes rapidly. Examples are: irrigation canals, vortex shedding, forced mixing, and atmospheric flows.
- there are strong shear layers. Examples are: atmospheric flows, fluid jets, flows past solids, and flows with strong vorticity.

(b) The mesh should be aligned with the flow to improve accuracy and increase the rate of convergence.

(c) Grid sensitivity or mesh dependency study should be performed with two or more meshes (with different mesh density) to ensure simulation results are mesh independent.

(d) Turbulence has a dominant role in the transport of momentum and other scalars for most complex turbulent flows. Therefore, simulations that involve turbulent flow tend to be more dependent on the mesh resolution than simulations involving laminar flow.

(e) For external flows[1], domain convergence study should be done to make sure that the flow boundaries (i.e. inlet, outlet and the walls) do not affect the solution. For example, if the simulation has an outflow boundary close to a bluff body, the wake momentum would not be able to recover before it meets the boundary.

4.2 Meshing Strategy

A meshing strategy allows one to determine the suitability of the mesh in a systematic approach. The following approach was adopted for this report.

(a) On a mesh of a given quality and sufficient fineness, higher-order discretisation schemes yield more accurate results than lower-order ones.

[1]External flow is such a flow that boundary layers develop freely, without constraints imposed by adjacent surfaces. An example of external flow is the problem of this study - flow across an actuator disc. On the other hand, internal flow is flow that is confined by a surface, hence the boundary layer is unable to develop without being constrained. A classical example would be pipe flow.

(b) For a given cell count, the aim is to optimize the grid quality (e.g. avoid high aspect ratios ; no excessive stretching) because a better mesh gives a more accurate solution regardless of the differencing schemes that are used and other parameters.

(c) With a poor-quality mesh, the gradient limiter is invoked more often, thus affecting its nominal second-order accuracy. Grid skewing is an important contributing factor (much more than grid stretching) to the loss in nominal accuracy of the solution. Grid design (distribution of cell size, local refinement using feature edges, boundary region, or volume shapes) is important in maximizing the accuracy for a given effort. Two grids with the same number of cells may lead to discretisation errors that differ by an order of magnitude.

(d) When solving steady-state problems, a much coarser mesh should be first used, followed by successively refining the mesh. Lower under-relaxation values for the coarsest mesh may be required but the computation time within each iterations should be faster since there are lesser cells. After the stopping criteria is satisfied or when the maximum specified number of iterations is reached, the mesh is refined and the simulation is restarted. This is repeated until the there is convergence of solution results with respect to the mesh size.

"All models are wrong, but some models are useful."
George Edward Pelham Box, 1919 - 2013

6 Turbulence Models

1 Introduction

Turbulent fluid motion is characterised by a spectrum of eddy sizes or degrees of freedom. Large eddies are associated with the flow dimensions and mainly responsible for the momentum transport in the fluid. On the other hand, the size of the smallest eddies are determined by the viscous forces. For high Reynolds (Re) number flow, the spectrum of scales is almost infinite and require a computational grid resolution that is proportional to $Re^{\frac{9}{4}}$. Besides representing the entire spectrum of eddy scales, the time step chosen must be sufficiently small to resolve the fastest fluctuation. When the grid resolution and the size of the timestep is sufficient, such a computational approach is called Direct Numerical Simulation (DNS). Practically, obtaining analytical or exact solution through DNS of engineering applications is impossible as the computational effort would be prohibitive.

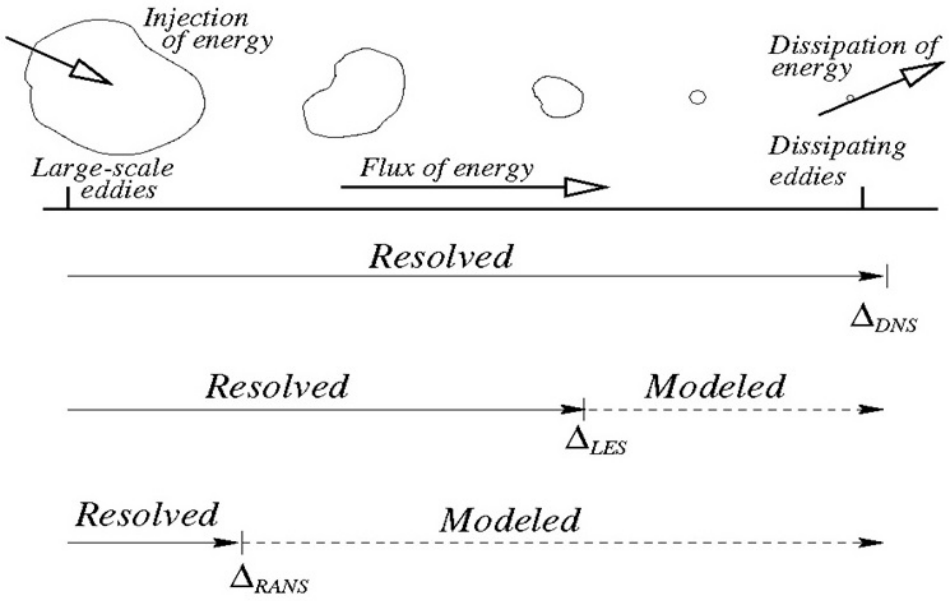

Figure 6.1: Schematic depicting the required amount of computation resources to resolve or model the flow physics by different methods.

2 Reynolds Averaged Navier-Stokes

Fortunately, for all practical problems, the engineering concern is not in resolving the instantaneous or time dependent variables. More often than not, the averaged variables or the mean flow properties are only required to understand the problem.

2.1 RANS Model

The classical manner to calculate the mean flow is to leverage on the Reynolds-Averaged Navier-Stokes (RANS) equations. In deriving the RANS equations, Reynolds Decomposition is applied where it is assumed that time varying chaotic (turbulent) fluctuation and the mean value can be separated from the instantaneous value.

$$\phi = \overline{\phi} + \phi' = \Phi + \phi' \tag{6.1}$$

The so-called averaged equations refer to time averaging for steady-state situations or ensemble averaging for repeatable transient situations. From 1st principles (see Appendix A), the RANS equations have been shown to be:

$$\rho\left(\frac{\partial V_i}{\partial t} + \frac{\partial V_i V_j}{\partial x_j}\right) = -\frac{\partial P}{\partial x_i} + \frac{\partial}{\partial x_j}(2\mu S_{ij} - \rho\overline{v_i' v_j'}) \tag{6.2}$$

where the term $\overline{v_i' v_j'}$ is known as the Reynolds stress tensor τ_{ij}. It is also interesting to note that the stress tensor is symmetric and only 6 of the components are unique. A total of 9 unknowns (6 Reynolds stress and 3 turbulent fluxes) have been thus introduced.

3 Turbulence Modelling

With only the RANS equations, there is an unclosed system of equations. Unfortunately, these equations are very difficult to solve as the set of equations is usually indeterminate (more unknowns than number of equations). It will not be possible to use Reynolds equation and the continuity condition to calculate the mean velocity $\overline{u(x_i,t)}$ and the mean pressure $\overline{p(x_i,t)}$ (in spatial and temporal terms) unless the unknown Reynolds stress tensor have been calculated. To solve the problem, additional partial differential equations are required to model these unknown expressions.

Turbulence Modelling is a process to determine the unknown turbulent quantities that have arisen from the Reynolds averaging process. A turbulence model is the set of relations or equations from which the the turbulent quantities can be directly or indirectly determined. This allows calculation of the mean flow without first calculating full instantaneous flow field. By using the RANS equations, it is indirectly implied that the turbulent behaviour is largely modelled (see Figure 6.1).

In a given simulation run, the amount of computational power devoted to obtain the flow characteristics is dependent on the resources required to either resolve or model the turbulent characteriestics. Turbulence modelling is therefore a way to reduce computational resources as more of the turbulent behaviour is modelled rather than resolved. The challenge is thus to model the Reynolds stress tensor τ_{ij} in terms of the mean flow quantities, and hence provide closure of the governing equations (RANS).

The current state of the art turbulence models can be classified by two manners: (a) the order of the model equations and (b) the required computation effort (see Figure 6.2).

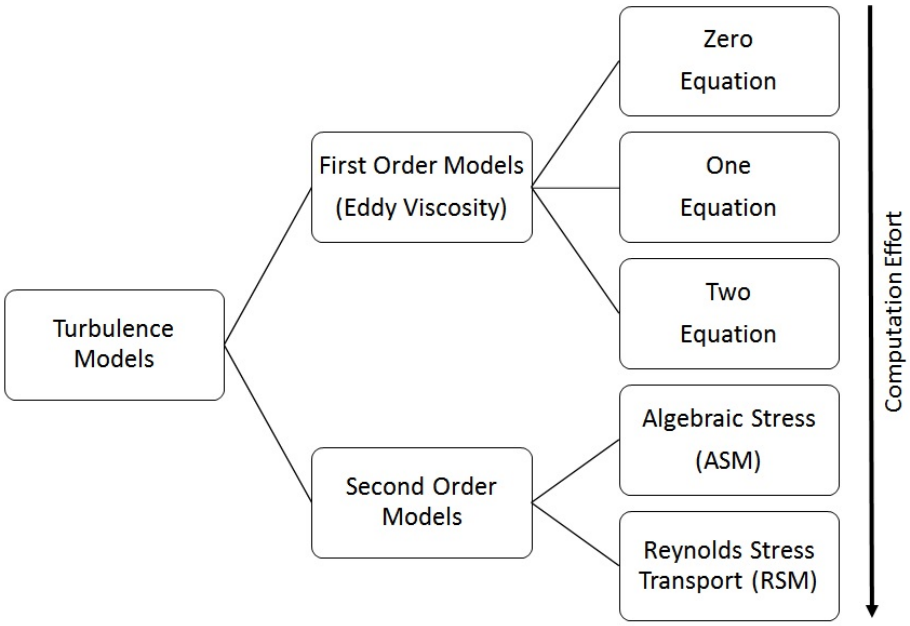

Figure 6.2: RANS Turbulence Models.

Turbulence is a natural phenomenon describing the apparently random and high fluctuating nature of fluid flow. It is associated with high Reynolds number and its physical origin is rooted in the instability of shear or viscous flows. It has been studied extensively and several classes of turbulence models have been developed in an attempt to describe the fluctuating phenomena in an analytical manner. It is widely acknowledged that turbulence models are not exact representations of the physical phenomena, and no single turbulence model is the best for every flow simulation. Consequently, the current state of the art provides a suite of models that may be more appropriate than the other in solving for the fluid dynamics. The choice of the model should then be judiciously applied according to the balance the availability of computation power and results accuracy.

This chapter will discuss the common and well-known numerical models and their respective approaches to represent turbulence.

3.1 First Order or Eddy Viscosity Models

First Order or Eddy Viscosity models are premised on the idea that the average turbulent flow field can be approximated by the corresponding laminar flow. The famous generalised Boussinesq approximation, uses this concept to model the unknown Reynolds stress tensor τ_{ij}:

$$\begin{aligned} \tau_{ij} &= 2\mu_t S_i - \frac{2}{3}(\mu_t \nabla \cdot u_i + \rho k_t) I_i \\ S_i &= \frac{1}{2}\left(\nabla u_i + \nabla u_i^T\right) \end{aligned} \tag{6.3}$$

where the subscript i denotes Einstein notation, S_i is the strain tensor, I is the turbulent intensity, k_t is the turbulent conduction coefficient and μ_t is the turbulent viscosity. From the equation, the Boussinesq approximation assumes a linear relationship between the τ_{ij} and S_i, where turbulent eddy viscosity μ_t is the proportionality constant. The terms μ_t (or ν_t) anf k_t are not physical properties of the fluid, but are quantities used in the Eddy Viscosity models to characterise the flow. In other words, their values vary from one flow to another.

Zero Equation Model or Prandtl's Mixing Length Concept

A very basic Eddy Viscosity model is the Zero Equation model, where no additional equations are introduced to calculate the turbulent quantities. Also known as the Prandtl's mixing length concept, the theory describes the 'mixing length' l_m (determined experimentally) over which there is high interaction of vortices in a turbulent flow field, where ν_t is linearly proportionate to the velocity gradient:

$$\nu_t \propto lu = l_m \left(l_m \frac{d\overline{U}}{dy} \right) \tag{6.4}$$

This results in simple algebraic relations which are used to calculate ν_t and k_t.

One Equation Model

The One Equation Model is based on an equation that calculates the unknown turbulent quantities (k_t and μ_t) as function of the turbulent kinetic energy K based on the Prandtl's mixing length concept.

$$K = \frac{1}{2} \left(\overline{u'^2} + \overline{v'^2} + \overline{w'^2} \right) \tag{6.5}$$

In turn, K is computed from another dervied set of equation. In gist, the K equation can be described as:

$$\text{Change Rate} + \text{Convective} = \text{Diffusive} + \text{Production Rate} - \text{Dissipation Rate} \tag{6.6}$$

The above equation introduces additional algebraic constants turbulent pressure D_k and turbulent diffusion ϵ coefficients, which are modelled according to the flow.

Two Equation Model

In a more sophisticated manner, Two Equation Models solve for the τ_{ij} through, as the name suggests, two partial differential equations. The idea here is to express ν_t and k_t in terms of the K and ϵ. To obtain K and ϵ, the two partial differential equations are then solved.

The first equation is the usual expression for K, like in the One Equation Model. Instead of modelling ϵ (as it was done in the One Equation Model), ϵ is calculated from another independent algebraic partial differential equation of which the algebraic constants are determined from benchmark experiments.

Two Equation Models are commonly used in rotor aerodynamics problems of which the most commonly known Turbulence Models are the k-ϵ and k-ω. k-ϵ models (ω represent the specific turbulent dissipation) are generally suited for industrial-type applications that contain multiple recirculation zones, heat transfer and flow impingement, while k-ω models are often compared to k-ϵ models due to their similarity but are often well suited for separated flows, low-Reynolds number flows or near wall flow problems.

To enjoy the advantages of both the k-ϵ and k-ω models, the k-ω Shear Stress Transport (SST) model was developed by Menter[43] by combining the former models. In gist, the k-ω is used in the inner boundary layer region and k-ϵ is applied in the free shear flow, resulting in better overall performance in flow situations with adverse pressure gradients and separated flow. The use of a k-ω formulation in the inner parts of the boundary layer makes the model directly usable all the way down to the wall through the viscous sub-layer, hence the k-ω SST model can be used as a Low-Re turbulence model without any extra damping functions[44]. The formulation also switches to a k-ϵ behaviour in the free-stream and thereby avoids the common k-ω problem where it is too sensitive to

the inlet free-stream turbulence properties. However, some authors have commented that the model does produce a bit too large turbulence levels in regions with large normal strain, like stagnation regions and regions with strong acceleration. This tendency is much less pronounced than with a normal k-ϵ model.

3.2 Second Order Models

In First Order models, the Boussinesq approximation applied to solve for τij, inherently assumes isotropic turbulence. Instead of this questionable assumption, Second Order Models introduce a large set of partial differential equations and require more computation effort as they involve many unknowns. The most famous Second Order Models are the Algebraic Stress Model (RSM) and the Reynolds Stress Model (RSM). Detailed explanation of the models are required to explain the workings of the two models. As it is not in the intent of this writing to detail the turbulence models, the reader is referred to any reputable turbulence textbooks.

4 Transient Models

In the previous section, the Navier Stokes equations has been expressed as the RANS equations. The Reynolds averaging process allows one to solve for the mean flow properties through modelling of the turbulence properties and computing its influence on the mean flow. Instead of using RANS Turbulence Models to model or prescribe almost the entire turbulence scales spectrum of the flow (see Figure 6.1), Transient models aim to resolve a large part of the turbulent motion. In this way, the Transient Models are able to deliver time-dependent results with information on the fluctuations at specific timesteps. However, this models incur very significant increase in computational cost and only suitable for low Reynolds simulations, in order to limit the turbulence spectrum. These models are primarily the Large Eddy Simulation (LES) and the Detached Eddy Simulation (DES).

4.1 Large Eddy Simulation

Large Eddy Simulation, as the name suggests, is a computational technique where large scales of the turbulence (or eddies) are solved and the small-scale motions are modelled (prescribed). The justification for doing so is the hypothesis that small-scale eddies are self-similar and their motions are universally known. It should be noted that LES delivers time dependent results.

Unlike the RANS momentum equations which are obtained by time-averaging, the momentum equations are obtained by a spatial filtering of the Navier Stokes equations. In order to solve the set of filtered equations (i.e. provide closure), the subgrid scale tensor T_t is obtained by using the well known Boussinesq approximation. In turn, to compute the T_t, a suitable Subgrid Scale turbulence (SGS) model is required to compute μ_t.

As mentioned above, turbulence models in LES are considered simple as only the small-scale turbulence is modelled. Furthermore, no equation for the turbulent length scale is required since the turbulent length scale can be taken as the spatial filter width Δ. In the context of LES, the range of length scales that need to be resolved would also depend on the Reynolds number - larger the Re, more turbulent scales need to be resolved and therefore computation time will increase.

Smallest scales of turbulent motion

In a turbulent flow, there is a range of scales of the time-varying fluid motion i.e. time in which turbulent structures occur and their sizes (lengths). The length scales of turbulent eddies usually correspond to the overall geometry of the flow. For example, in an industrial smoke stack, the largest scales of fluid motion are as big as the diameter of the stack itself.

On the other hand, the size of the smallest length scales is set by the Reynolds number. As the Reynolds number increases, smaller and smaller scales of the flow are visible. In the smoke stack example, the smoke may appear to have many very small velocity perturbations or eddies, in addition to large bulky eddies. In this sense, the Reynolds number is an indicator of the range of scales in the flow. The higher the Reynolds number, the greater the range of scales. The largest eddies will always be the same size while the smallest eddies are determined by the Reynolds number, which is a non-dimensional variable defined as

$$Re = \frac{\text{Inertial Force}}{\text{Viscous Force}} \tag{6.7}$$

A large Reynolds number indicates that viscous forces are not important at large scales of the flow. With a strong predominance of inertial forces over viscous forces, the largest scales of fluid motion are undamped (due to the larger momentum) as there is not enough viscosity to dissipate their motions. The kinetic energy must cascade from these large scales to progressively smaller scales until a level is reached for which the scale is small enough for viscosity to become important (that is, viscous forces become of the order of inertial ones). It is at these small scales where the dissipation of energy by viscous action finally takes place. The Reynolds number indicates at what scale this viscous dissipation occurs.

Subgrid Scale Turbulence Model

Subgrid-scale (SGS) modeling refers to the representation of the important small-scale physical processes that occur at length-scales that cannot be adequately resolved on a given mesh grid. In LES simulations, SGS turbulence models are used to represent the effects of unresolved small-scale fluid motions (small eddies, swirls, vortices) while equations governing the larger scale motions are resolved. The formulation of physically realistic SGS models requires understanding of the physics and the statistics of scale interactions in hydrodynamic turbulence, and is still an active research area.

Similar to RANS's Eddy Viscosity Turbulence Models, the turbulent stress tensor is also modelled using the Boussinesq approximation. This means that for LES, the applicability of Equation 6.3 is at the subgrid scale (i.e. T_t represents the subgrid stress tensor).

Several state-of-the-art SGS models are currently used. The Smagorinsky and the Wall-Adapting Local-Eddy viscosity (WALE) subgrid scale models are often the two most commonly used. To obtain the subgrid scale tensor T_t, the Smagorinsky SGS model uses the simple Prandtl's mixing length concept (computationally inexpensive), while the WALE SGS model provides algebraic equations to be solved. Both models have tuning parameters that must be set according to the flow situation. The reader is referred to advanced CFD textbooks for formulation of the various SGS turbulence models.

4.2 Detached Eddy Simulation

Detached Eddy Simulation (DES) is a combination of LES and RANS calculations. Near wall boundaries, where the turbulent length scale is less than the user-defined grid dimension, the flow is resolved

using the RANS Turbulence Model. For turbulent length scales exceeding this dimension, the flow is resolving using the LES mode. In this way, the grid resolution for DES is not as demanding as pure LES, and therefore computation cost is reduced. The challenge for DES is the mesh generation due to the hybrid RANS-LES switch.

5 Unsteady Simulations

This aim of the thesis involves investigation of the dynamic inflow phenomena, which is inherently unsteady. To this end, some remarks are noted for the unsteady flow numerical simulations.

5.1 Unsteady RANS and Large Eddy Simulation

To obtain the time dependent solution of the unsteady flow, simulations can be carried using the Unsteady RANS model or Transient Models, mentioned in previous sections. From the RANS model, solving for the flow dynamics would only yield the mean flow properties. On the other hand, LES provides high fidelity information of the turbulence fluctuations of the unsteady phenomenon. Table 6.1 compares the numerical codes between RANS and LES - both can be applied in commercial solver `Star-CCM+` which was used in this research.

Table 6.1: Comparison of RANS and LES code in `Star-CCM+`.

	RANS	**LES**
Results	mean flow	time-resolved flow
Spatial Domain	2-D or 3-D	always 3-D
Time domain	steady or unsteady	always unsteady
Spatial discretization	2nd order upwind	central differencing (non-dissipative)
Grid resolution	Average	Fine
Time discretization	1st order	2nd order (e.g. Crank-Nicolson)
Turbulence model	two-equations	zero- or one-equation
Computation effort	Average	Expensive (only appropriate for low Re)

For this thesis, the interest is in the the mean flow characteristics which would be used to benchmark against other flow models and experimental results.

5.2 Time Stepping

An implicit time-marching scheme would be implemented for the simulations used in this research. The type of time-marching scheme is known to be much more stable and handle flows at higher courant numbers.

Computation Residuals

Residuals measure the imbalance of the conservation equations (continuity and momentum) or the degree to which their discretised form is satisfied. In other words, residuals represent the solution error of a particular variable. For every equation, the residuals in each cell are known and usually normalised from the maximum of the initial few iterations. The normalised residuals would then represent the order of magnitude in which the subsequent values fall from their peak values.

For a given time instance or steady simulation, the residuals will decline as the solution converges. On the other hand, for unsteady flow the residuals for each quantity will rise and go through the same process of convergence within the time step. This would give rise to an residual plot that looks jagged or uneven.

As the size of the time-step decreases, the residuals within a given time instance typically decrease faster with the number of inner-iterations. The initial guess to the next iteration uses the final solution from the previous time-step. Since the difference in time smaller, the solution difference between the previous and current time step is expectedly smaller which means a faster convergence of the residuals. Typically, the residuals should be reduce a one to two orders of magnitudes within each time-step. Therefore, the rate of solution convergence within a time-step needs is dependent on the size of the time-step and the number of inner-iterations.

Time Step Δt

For implicit time-marching schemes, the choice of time-step is an engineering judgement (just like grid refinement) and is also dependent on the time scales of the physical phenomenon. The convective Courant Number C is a helpful indicator to select the time-step size for unsteady simulations. The parameter relates the size of the time step to the number of interval lengths of each spatial coordinate and of the maximum speed with which information can travel in the physical space. In other words, C is the dimensionless transport of the flow quantity per time step (in terms of the mesh size Δx).

$$C = \frac{V \Delta t}{\Delta x} \tag{6.8}$$

For explicit time-marching schemes, the convective Courant number should be 1.0 on average in the zone of the interest. This value implies that the fluid moves by about one cell per time step. For implicit time-marching schemes, a dependency study would be warranted to optimise the size of Δt.

"The logic of validation allows us to move between the two limits of dogmatism and skepticism."

Paul Ricoeur, 1913 - 2005

7

Setup and Validation of Actuator Disc Model

1 Actuator Disc Model

The actuator disc model is an efficient means to simulate forces on a real rotor blade into a computational flow field by distributing the forces over a permeable disc volume with an area that of the rotor swept area.

The basic actuator disc model setup in `StarCCM+` was first validated against known theoretical results. This would ensure the reliability of the model before the dynamic inflow flow cases are prescribed. In the validation study, only steady flow cases were considered i.e. constant momentum sinks (representing the actuator disc).

1.1 Mesh

The actuator disc model was implemented both in both two and three dimensions. Intuitively, a 2-D mesh would require less computation resources as there are lesser cells. Further computation time can be saved by simulating the flow using half a disc by assuming axi-symmetric flow along the rotor axis. STAR-CCM+ converts 3-D geometries to 2-D by taking a slice of the geometry on the $Z = 0$ plane. However, in the course of the study, it was later concluded that a 3-D model gave more accurate results as it would account for the 3-D effects which would affect the fluid properties at the rotor plane as well as to the wake.

The adjacent wall boundaries were set as 'slip' condition, and velocity inlet and pressure oulet were prescribed for the inlet and outlet boundaries respectively.

1.2 Numerical Model

The RANS equations is selected as the numerical model to be resolved. The turbulence model selected to simulate the Reynolds shear stresses is the k-ω Shear Stress Transport (k-ω SST) as the computation effort is reasonable and is known to perform well in separated flows, since one would expect this phenomenon to be dominant in the wake's shear layer.

The momentum sink represented by the actuator disc is introduced as a body force or source term in RANS, with dimensions of force per unit volume. Since a uniformly and axially loaded rotor is sought, source terms are only added in the axial-direction (x-axis) momentum equation. To implement the ideal actuator disc model, the thickness of the actuator disc th should be zero. As this is practically impossible, a value equivalent to the thickness of the porous discs used in the experiment would be used. The value of the source term corresponding to a desired C_T can be computed using the following:

$$\begin{aligned} C_T &= \frac{F_x}{\frac{1}{2}\rho V^2 A} \\ \iff \text{Source Term } [\text{N/m}^3] &= \frac{F_x}{A \cdot th} \\ &= \frac{C_T}{th} \cdot \frac{1}{2}\rho V^2 A \end{aligned} \tag{7.1}$$

1.3 Physics Solver

The `Segregated Flow` solver was selected, where the spatial discretisation is the second-order upwind scheme. For the validation of the actuator disc model, only steady load conditions were considered and therefore the steady RANS model was used. For unsteady simulations, a 2nd order implicit temporal discretisation was used.

2 Mesh Dependency Study

A mesh dependency study was conducted on the actuator disc model to check how the results would vary with respect to the mesh design. The mesh density and the domain size were both varied to study its correlation with the results. From the study detailed in the following, a domain size of 10D, 30D and 30D representing the upstream, downstream and inlet respectively, together with cell sizes of 0.3 m and 0.05 m for the Outside Wake and Wake regions were shown to deliver reasonable results.

2.1 Domain Size

The dependencies of the inlet, upstream and downstream sizes were investigated (see Figure 7.1). It is expected that the streamtube across the actuator disc would expand (or streamlines be compressed) due to the rotor. Since the aim is to model a wind turbine operating in an unbounded environment, the computational domain should be sufficiently large to allow aerodynamics convergence and avoid blockage effect. The distance between the boundaries should be reasonably large such that the expansion of the wake does not lead to significant flow acceleration outside the wake.

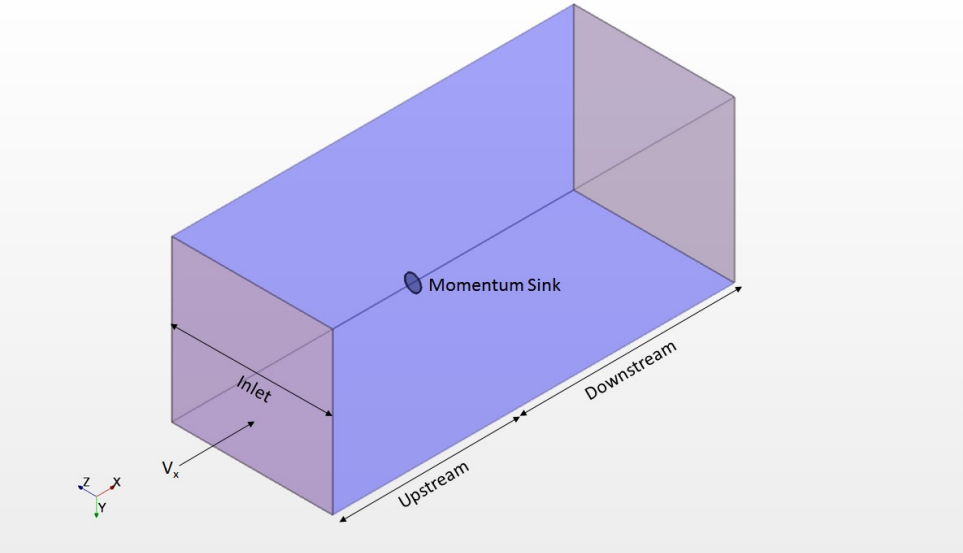

Figure 7.1: Computation Domain.

The presence of the momentum sink affects the flow downstream, as well as the rotor inflow located upstream. This is because of the generated vortex eddies in the flow due to velocity gradients, especially at the rotor edge. According to the Bio-Savart law, the influence of a concentrated vortex core on a point in the flow field reduces with distance. Therefore, to accurately resolve the near wake profiles, the domain should be sufficiently extended so that the effect of these vortices are accounted. Table 7.1 shows the test matrix used to study the domain size dependency.

Table 7.1: Test Matrix for Domain Size dependency.

Dependency Case		Inlet [D]	Upstream [D]	Downstream [D]
Upstream	a	10	5	15
	b	10	10	15
	c	10	20	15
	d	10	30	15
Downstream	a	10	10	15
	b	10	10	30
	c	10	10	50
	d	10	10	75
Inlet	a	5	10	15
	b	10	10	15
	c	30	10	15
	d	50	10	15
	e	100	10	15

A total of 11 nodal points N were evenly assigned along the radii of the disc, which in effect, spatially divides the disc into 10 annulus rings. By assuming axi-symmetric flow, the velocity induction profile sampled at each of the nodal point i was then used to compute the average induction profile according to the following:

$$a_{\text{avg}} = \frac{\sum_{i=1}^{N-1} \frac{a_i + a_{i+1}}{2} \cdot \pi \left(r_{i+1}^2 - r_i^2\right)}{\pi R^2} \tag{7.2}$$

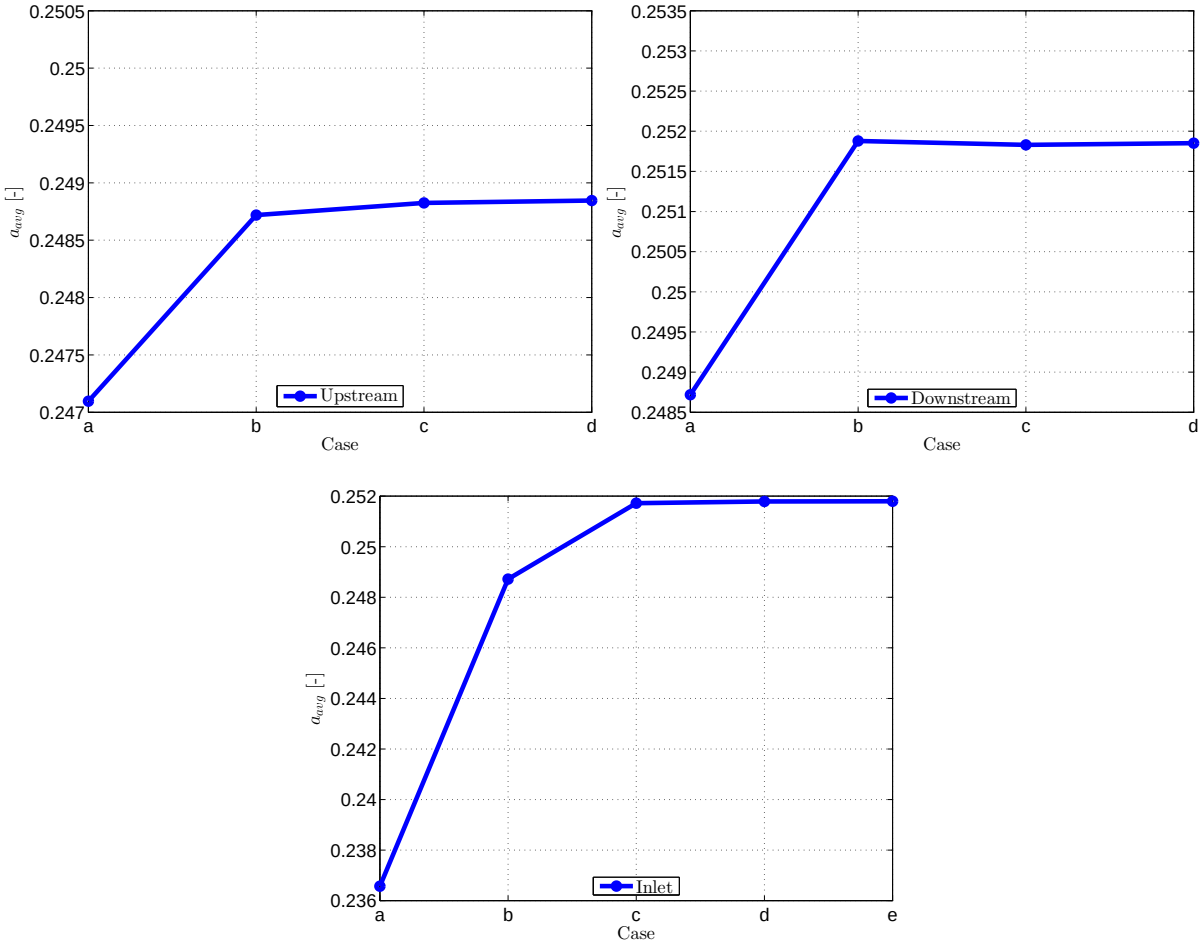

Figure 7.2: Domain Size Convergence Study on the Upstream, Downstream and Inlet.

Ideally, the computational domain should be infinitely large since the intention is to simulate the flow dynamics in a large unbounded environment. Obviously, this would be practically unachievable as the amount of computational time would scale with the domain size. As seen from Figure 7.2, a_{avg} begins to converge beyond a critical domain size. Balancing between finite computational resources and result accuracy, the upstream, downstream and inlet sizes were chosen to be 10D, 30D and 30D respectively.

2.2 Mesh Density

Mesh density refers to the number of cells present in the computational domain. A results-versus-mesh density convergence was done to determine the minimum cell size to obtain a converged output. The study was carried out by varying the number of cells in two parts of the domain - the Outside Wake and the Wake regions (Figure 7.3).

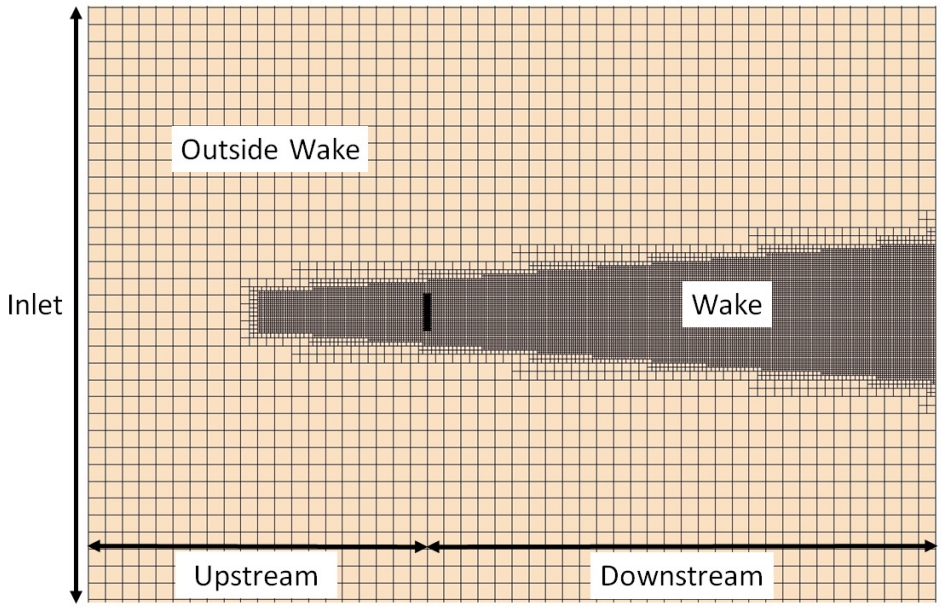

Figure 7.3: Planar side view of the Mesh of the Computational Domain.

It is important not to prescribe an excessive mesh density as more computational resources would be used to resolve the model equations at each cell, with no difference in result compared to one with reasonable mesh density. A reasonable solution was considered to be achieved with the convergence of the velocity induction a_{avg} profile, which was similarly computed using Equation 7.2. Table 7.2 shows the test matrix to study the mesh density dependency.

Table 7.2: Test Matrix for Mesh Density dependency.

Dependency Case		**Cell Size [m]**	
		Wake	**Outside Wake**
Outside Wake	a	0.05	0.6
	b	0.05	0.4
	c	0.05	0.3
	d	0.05	0.2
Wake	a	0.20	0.3
	b	0.10	0.3
	c	0.05	0.3
	d	0.01	0.3

It is expected that the flow field would be largely stable in most parts of the domain, except for the wake region. From Figure 7.4, it was noted that the mesh density in the Outside Wake region indeed had no bearing on a_{avg} and the fluctuation were likely due to numerical residuals and the number of iterations. On the other hand, the influence of cell size in the Wake region was significant as the result improved with grid refinement. Once again, the final decision on the size of the cells had to be balanced against the finite computation resources. With that in consideration, cell sizes of 0.3 m and 0.05 m were used for the Outside Wake and Wake regions respectively.

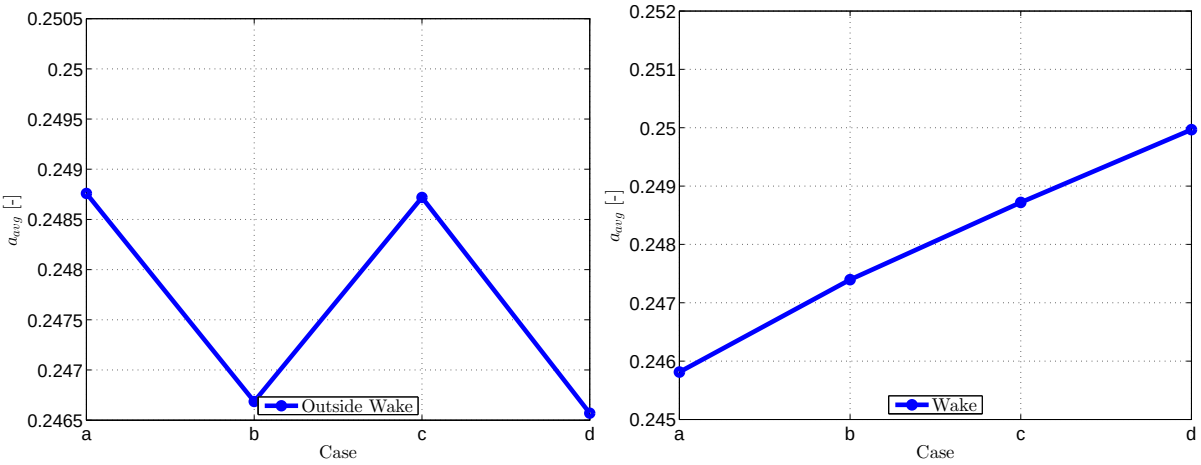

Figure 7.4: Mesh Density Convergence Study at the Outside Wake and Wake regions.

3 Comparison with Momentum Theory

According to actuator disc or axial momentum theory, the following relationship exists:

$$C_T = 4a(1-a) \tag{7.3}$$

where a is the axial induction factor used to denote the ratio of velocity loss (due to energy exchange), to the freestream value. Figure 7.5 shows several prescribed inputs of C_T and corresponding resolved a_{avg} plotted against the theoretical relationship curve. For low thrust coefficients or Windmill states, there is generally excellent agreement of the actuator disc numerical model with theoretical results.

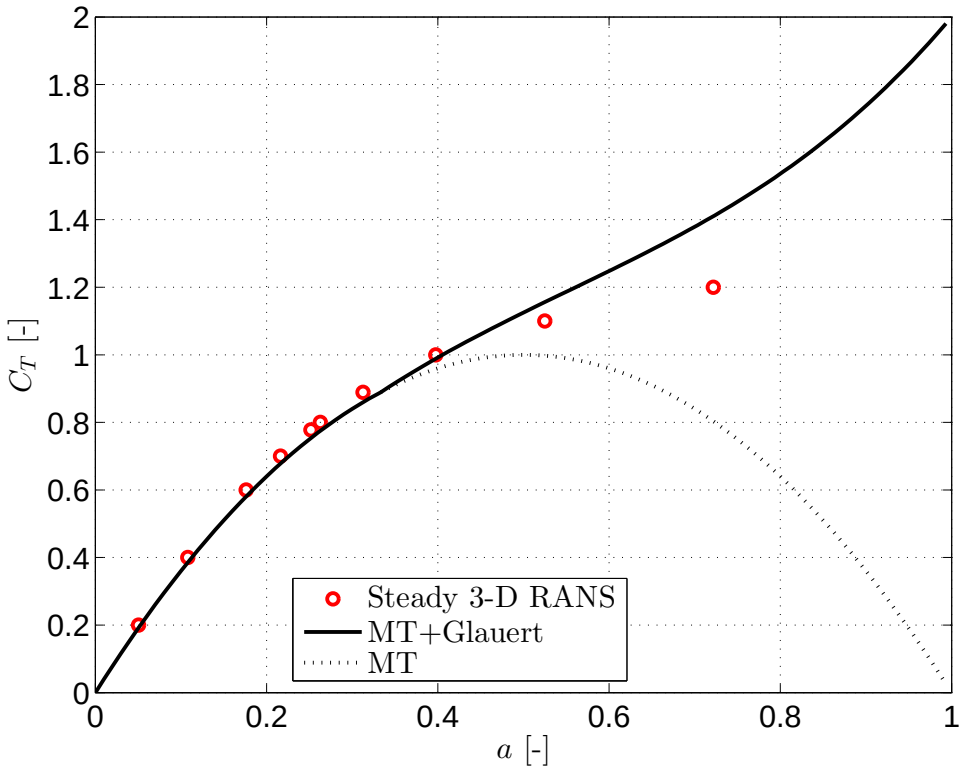

Figure 7.5: Results comparison of numerical code from StarCCM+ against axial Momentum Theory.

3.1 Low Loading - Windmill State

From Figure 7.5, it was observed that the error between theoretical and numerical results reduce at lower thrust coefficients. This (slight) under-estimation of the velocity induction can be attributed to tunnel or blockage effects. MT assumes a fluid domain which is unbounded i.e. infinitely large. This means that the freestream and the flow in the far field is undisturbed by the presence of the rotor and its wake. However, in a finite computational domain, the rule of mass conservation means a higher velocity in the Outside Wake region due to the blockage of the rotor. The over speeding is also felt in the Wake region and is similar to experimental simulations in the wind tunnel[54]. This translates to an underestimation of the induction. For a given computational domain, a larger C_T results in a larger wake, which in turn leads to greater over speeding error in the freestream.

In the context of this thesis, the focus is on wind turbines designed to operate under usual conditions or in the Windmill states. Therefore, this actuator disc model was assessed to be sufficiently reliable to investigate its unsteady effects.

3.2 High Loading - Turbulent Wake State

MT predicts that at a critical $C_T = 1$, the predicted induction at the rotor plane ($a = 0.5$) would result in zero velocity at the far wake. If this was true, there would be a collection of air mass in the wake and there would no flow aft the rotor.

As noted in the literature review, MT assumes an inviscid fluid and is thus only reliable at low induction factors, where there are low velocity gradients between the wake and freestream. As a increases beyond $\frac{1}{3}$, the RANS results significantly deviate from MT and a continues to increase with C_T. This deviation is in line with the empirical relation proposed by Glauert[26]. The so-called Glauert's correction factor accounts for rotors with high C_T, where viscous effects are apparent. At higher values of C_T, the velocity deficit in the wake increases. Due to high velocity gradient across the shear layer, eddies are formed in the shear layer increase transport of momentum from the freestream into the wake, thereby energising it (see Figure 2.4). In other words, the inviscid MT, which assumes a non-shearing fluid, is invalid at high C_T values. The turbulent eddies in the shear layer cause significant velocity fluctuations in the wake which explain the term 'turbulent wake state'.

Regarding the observable deviation of the numerical results from the Glauert's correction curve, it should be emphasised that the Glauert's correction is an empirical formulation. Glauert's formulation was derived by fitting a parabola to experimental data[39] obtained from turbines operating in the turbulent windmill state. It is noted that this data has a large scatter as it was obtained from different turbines (see Figure 7.6). Besides the uncertainty caused by the curve fitting, the deviation could also be due to the differences in flow characteristics (e.g. blade tip losses) of a real rotor with finite number of blades.

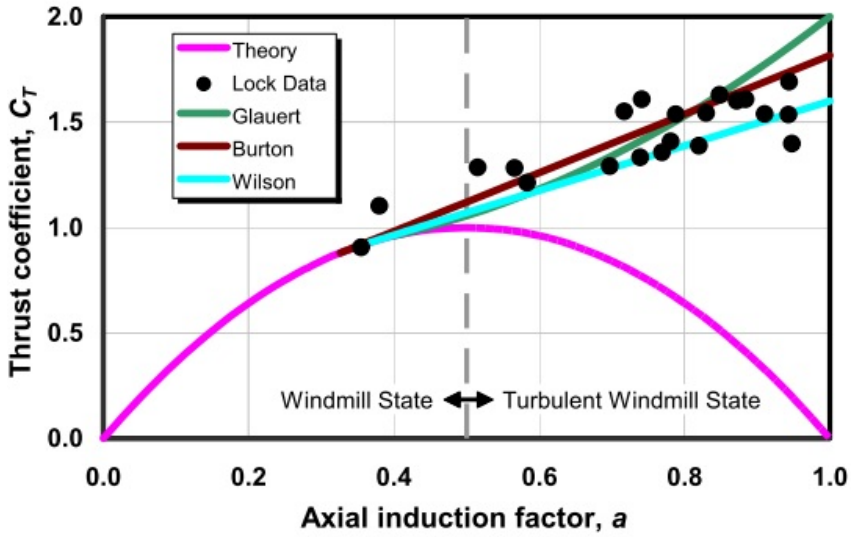

Figure 7.6: Fitting of correction curves on experimental data for turbines operating in the Turbulent Wake state[15].

4 Velocity Field

The flow velocity at various streamwise planes were compiled from the 3-D RANS computations. This section analyses these profiles at low and high C_T and examines the influence of ambient turbulence towards the steady state results.

4.1 Upstream

Far upstream of the rotor, the flow expectedly assumes the properties of the undisturbed freestream. However, near the rotor, the flow begins to react to the presence of the rotor as seen in Figure 7.7. Given a distance, higher velocity deficit is apparent in the flow. In tandem with the slow down of the flow, the wake has started to take shape - denoted by a region where the velocity is less than the value of the freestream.

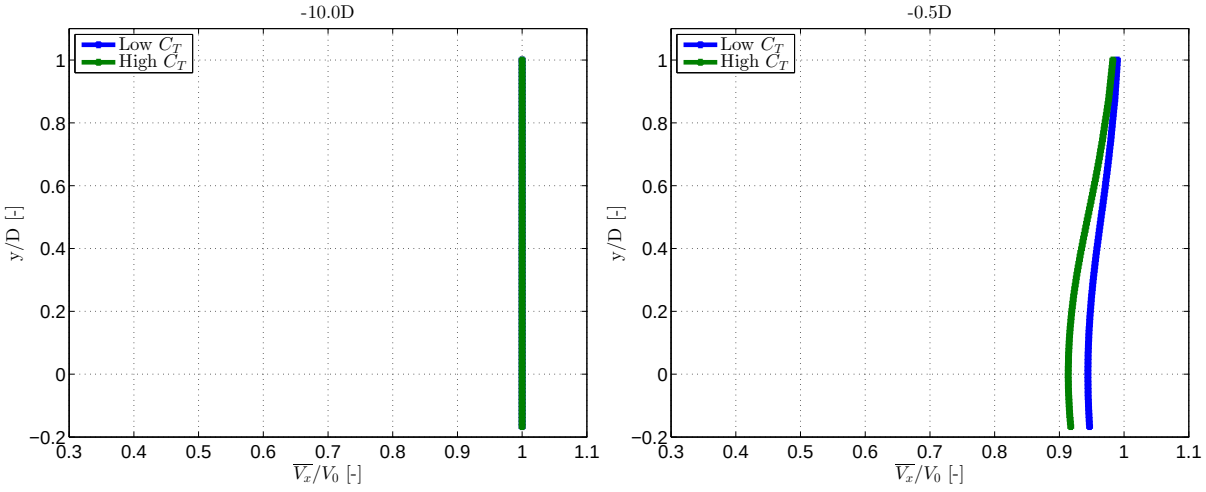

Figure 7.7: Upstream Velocities for low and high C_T.

4.2 Near Wake

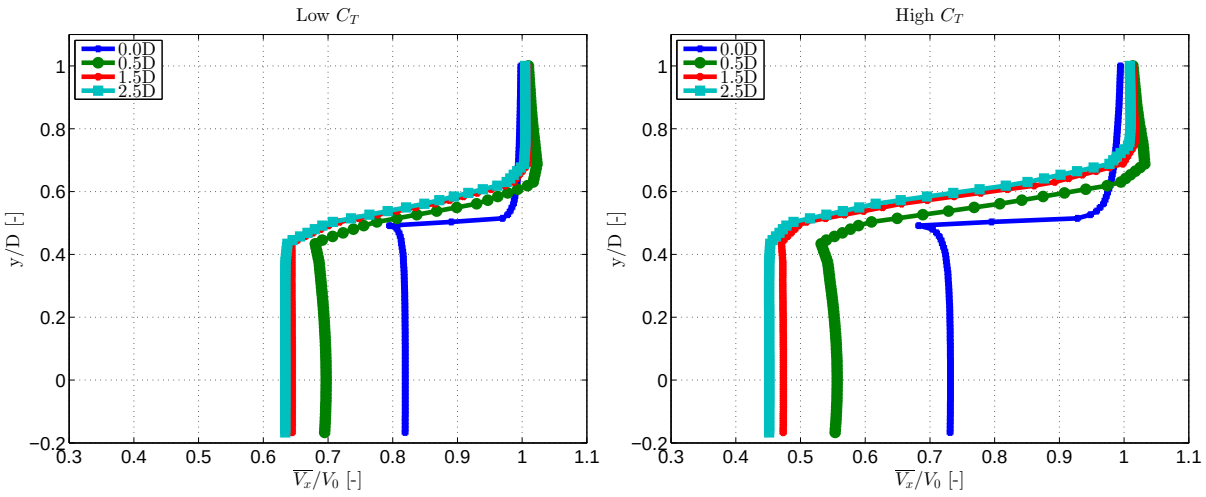

Figure 7.8: Near Wake Velocities for low and high C_T.

From Figure 7.8, interesting observations were noted between rotors of low and high C_T. Firstly, it is obvious that the velocity deficit at the rotor plane increases with C_T. The inflow velocity profile (0D) is also more convex at higher C_T. This is due to the higher velocity gradients at the disc edge which generates stronger vortices in the shear layer. The presence of these strong vortices induces velocity in the general upstream direction, which therefore explains a sharper concave profile. Secondly, for the high C_T rotor, the velocity decrease rate in the near wake occurs is more for the same downstream distance. In other words, it could be argued that the the wake field of rotors with higher C_T attains the global minimum velocity within a shorter space.

4.3 Far Wake

At 5D, momentum recovery has started to take effect as shown in Figure 7.9. Comparing both rotors, the wake of rotors of low C_T is relatively stable for longer distances. On the other hand, the a higher loaded rotor achieves faster velocity recovery allow with rapid shear layer expansion (region of velocity gradient).

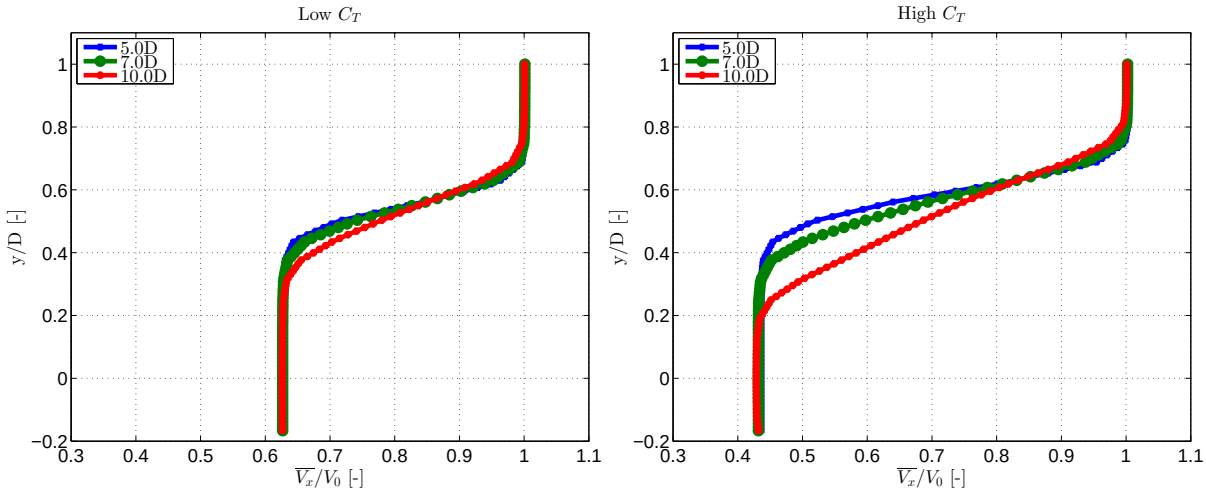

Figure 7.9: Far Wake Velocities for low and high C_T.

The velocity deficit decay can also be seen in Figure 7.10. Here, one can observe that recovery process occurs spatially earlier for the high C_T rotor and that it occurs from the outer towards the inner wake.

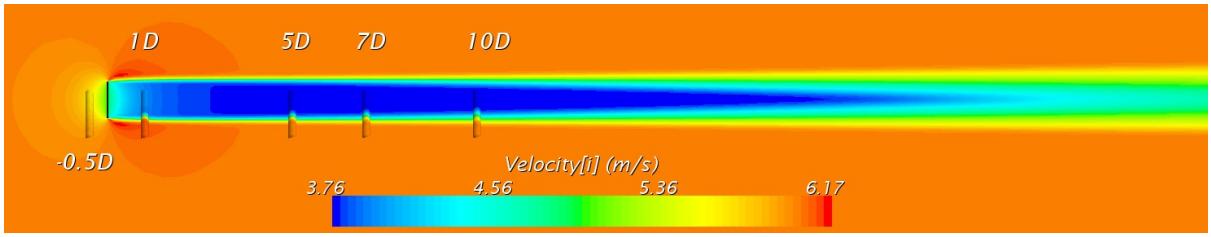

(a) Low C_T.

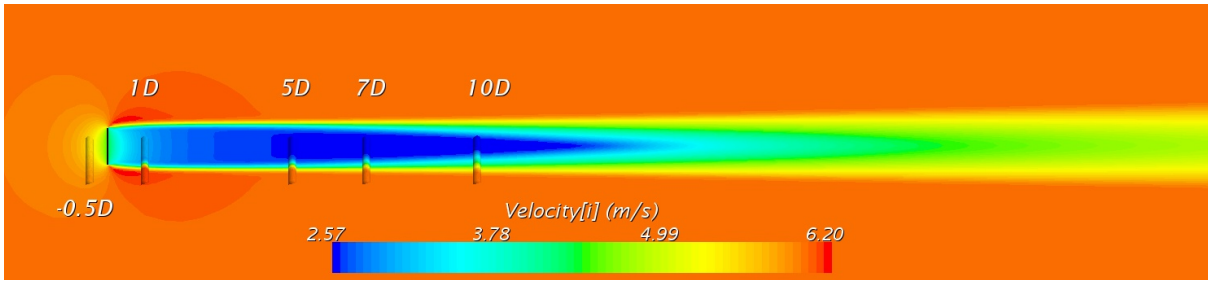

(b) High C_T.

Figure 7.10: Velocity contour maps for low and high C_T.

5 Vorticity and Turbulent Intensity Field

5.1 Vorticity production and its influence on inflow velocity

In Figure 7.11, the strength of the shed vortices are strongest at the disc edge, which is the production area. Looking at the contour scales, the strength of the generated vortices increases with C_T. This is expected since there is a larger pressure gradient at the rotor edge.

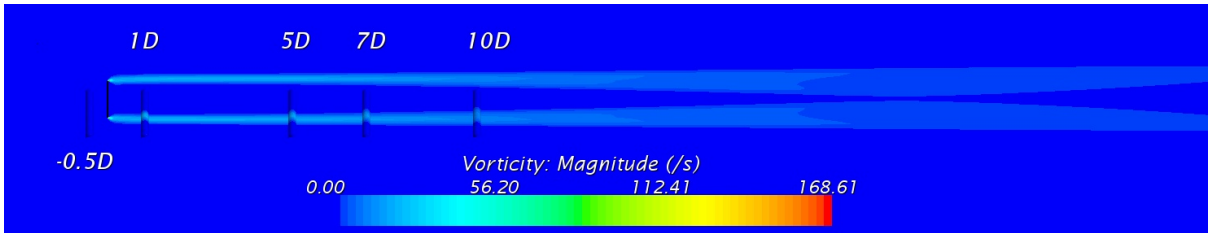

(a) Low C_T.

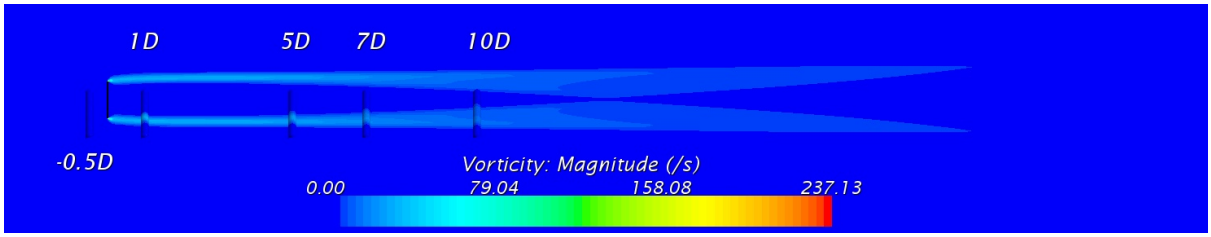

(b) High C_T.

Figure 7.11: Vorticity contour maps for low and high C_T.

The shed vortices for the case of high C_T are also less stable and breaks down earlier. This is explained by the more vigorous entrainment and mixing with the freestream which contributes to the earlier breakdown and diffusion. It is also noted that vorticity production only at the edges is only peculiar here as there is uniform loading. Appendix B derives this effect from the NS equations. In blade rotors, while vorticity production may be present along the blade span due to non-uniform loading, the generation is still predominantly at the blade tip and root.

For an actuator disc, the shed vortices diffuse faster than the case of a bladed wind turbine rotor (see Figure 7.12). For a wind turbine rotor, the spatial distance between vortex cores is dependent on the number of blades and rotation frequency. In this manner, it is known that the instability onset of the shear layer of a three-bladed rotor would be earlier than that of a two-bladed machine. An actuator disc is akin to a wind turbine rotor with infinite number of blades (or a bladed rotor spinning at high speed). This would explain why the concentrated vortex core shed at the tip of an actuator disc rapidly decreases downstream.

The formation of distinct vortex cores (see Figure 7.12) in the case of a blade rotor, which is absent from an actuator disc flow. In the figure, the breakdown of the shear layer is illustrated. The tip vortices interact with each in a 'leap-frogging' manner and eventually coalesce together. This results in the subsequent break down of the distinct shear layer. If one would imagine the blade rotor to have an more number of blades or is spun at high speeds, the spacing between subsequent tip vortices would be very small. One would also expect an earlier onset of instability as the coalescing of the tip vortices would be earlier. Given an unlimited number of blades, the blade rotor assumes a disc rotor. Therefore, one would expect the shear layer of a blade rotor to be more stable and persistent compared to an actuator disc flow.

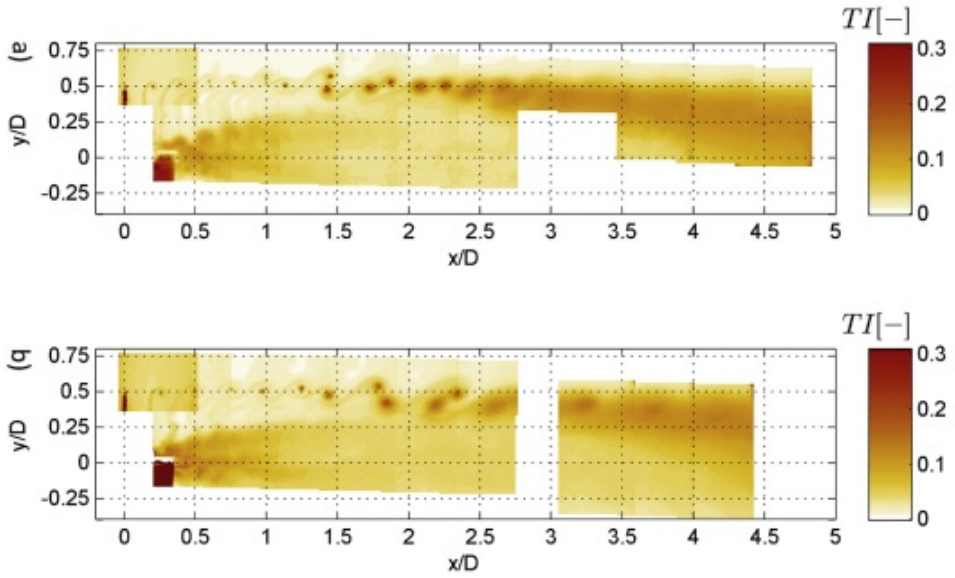

Figure 7.12: Turbulent intensity contour images post processed from a phase-locked PIV experiment[37] showing the instability and subsequent breakdown of the shear layer of a two-bladed wind turbine model.

5.2 Turbulent Intensity

In Figure 7.13, the turbulent intensity contours demonstrate that higher loaded rotors contribute to larger velocity fluctuations in the wake. This turbulence in the flow is wake-induced and caused by the presence of the actuator disc rotor, since ambient turbulent is negligible. The spread or increase of TI towards the inner wake is also in tandem with the shear layer breakdown and recovery of the mean flow. In the context of windfarms, this would be of concern as downstream wind turbines would be subjected to more fatigue damage.

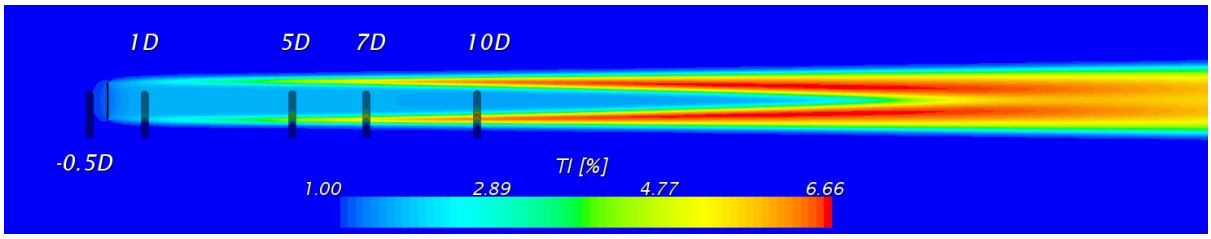

(a) Low C_T.

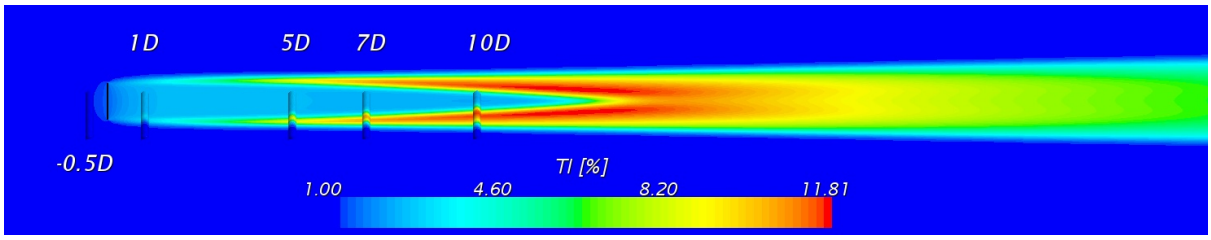

(b) High C_T.

Figure 7.13: Turbulent Intensity contour maps for low and high C_T.

6 Effect of Ambient Turbulence

Other than the influence of C_T on the onset of shear layer instability, the ambient turbulence of the incoming flow is also known to affect the wake development. Higher ambient turbulence further enhance the momentum mixing process and accelerate the velocity deficit decay.

6.1 Near Wake

As seen in Figure 7.14, it is observed while the inflow velocity profile is thus largely driven by C_T, there wake velocity profile is certainly being influenced especially for large values of ambient TI. More importantly, it could said that there would be discrepancy of the velocity induction at the rotor plane under real ambient conditions and that predicted by the inviscid MT. Away from the rotor, the dominant influence of C_T on the velocity profile quickly diminishes. In Figure 7.14, one can clearly observe that velocity recovery has already begun at 1D with low ambient TI of 5%.

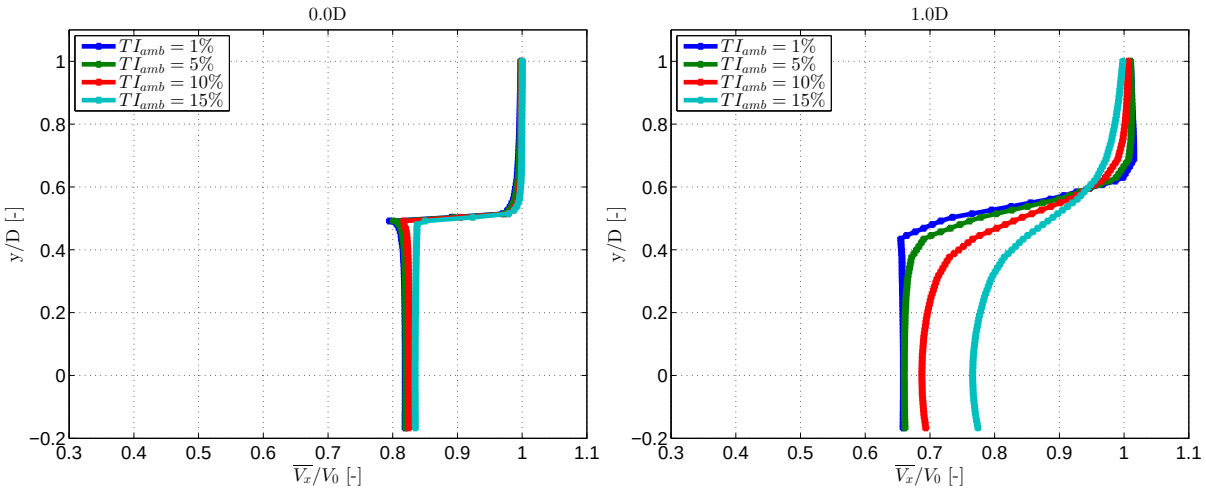

Figure 7.14: Near Wake Velocities under different ambient TI conditions.

6.2 Far Wake

The behaviour observed in the near wake generally holds for the far wake (see Figure 7.15). However, it is interesting to note that there appears to be a plateau in the recovery rate as the velocity profile between 7D and 10D do not appear to have significantly changed at an ambient TI of 15%. It is hypothesized while the turbulent intensity can positively influence the wake recovery, there is a maximum rate at which this occurs.

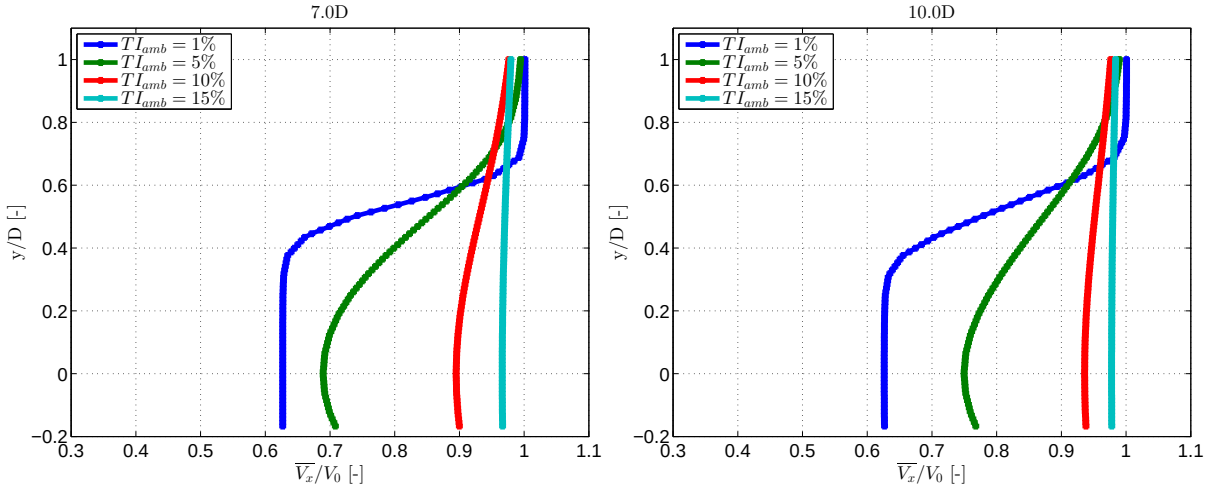

Figure 7.15: Far Wake Velocities under different ambient TI conditions.

In cases with higher ambient TI, the onset of the shear layer breakdown occurs farther upstream due to more vigorous momentum mixing between the wake and the freestream. The velocity contours in Figure 7.16 further illustrate this effect. From this analysis, it was concluded that the while the momentum recovery process is influenced by both the ambient and wake-induced turbulence, but is driven by the former. From the perspective of power production in a wind farm, high ambient TI could be desirable as the downstream turbines would receive a faster inflow.

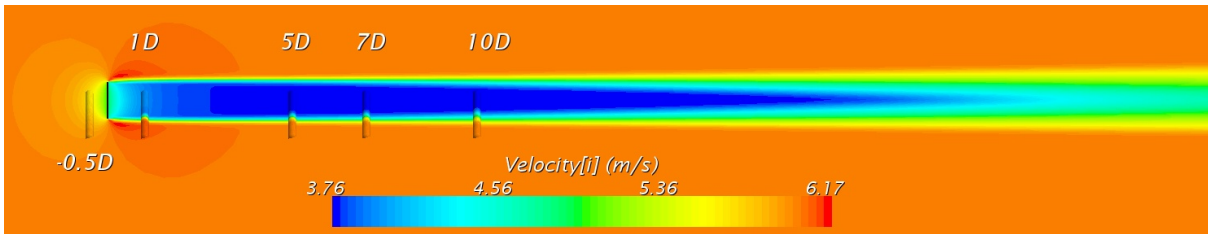

(a) TI=1%.

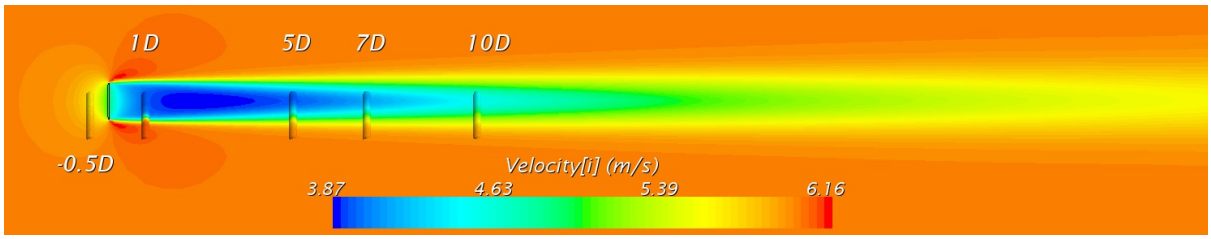

(b) Ambient TI=5%.

Figure 7.16: Velocity contour maps under low and high ambient TI.

Part III: Experimental Work

"There is nothing new to be discovered in physics now, All that remains is more and more precise measurement."

The Lord Kelvin (1824 – 1907)

8 Flow Measurement Technique

This chapter describes the working principles behind the technique used during the two experimental campaigns. The hot-wire anemometry (HWA) was used in the first and second campaigns to measure the characteristics of the rotor's wake field.

1 Concept of Time-Averaged and Time-Resolved Data

While it is possible to measure the instantaneous velocity field, more characteristics of the flow can be derived by computing the average or mean velocity field. This is done by averaging the results from several (e.g. hundred or thousand or more) instantaneous velocity fields of the same phenomenon. Likewise, the root-mean-squared quantity is usually useful to understand how the flow is varying over time, in an average sense. To avoid long computation times, an optimal number of velocity fields is sufficient instead of relying having an excessive amount. For calculating average and RMS velocity, it is recommended to use velocity fields that are not correlated in time, meaning that the flow structures from one capture to the next have 'moved on' and are no longer visible in a given field of view (FoV). For this reason, data capturing will typically occur at a 'slow' rate, where the term 'slow' is relative to the flow in question. A co-relation analysis would be required to determine the time delay between samples.

Should information on the flow development be desired, time-resolved data is required. This involves the capturing of a series of velocity fields that are correlated, or related, to each other in time. Typically, this means that the same fluid structure can be seen in multiple consecutive velocity fields within a given FoV. The data is often analysed by watching a 'movie' or animation of the velocity fields, so that the viewer can see how fluid structures move from frame to frame and how they are interacting over time. Because fluid structures move at different rates (or known as the time-scale) in different fluids or flow situations, the capture rate of 'timeresolved' data can vary. In other words, the rate of capture must be faster that the time duration of a phenomenon which is being observed.

2 Hot Wire Anemometry

The hotwire anemometer (HWA) system is a technique to measure the flow speed. In this experiment, the TSI IFA 300 thermal anemometry system was used. The working principle of a HWA is that varying current is sent across a very fine piece of film or wire placed in the flow, and depending on the flow speed, the amount of current required to maintain the wire/film at a constant temperature is known. By measuring the voltage across the wire/film, this information is then matched against the calibration curve (done prior to the actual flow measurement), which then gives the flow speed 'seen' by the hotwire.

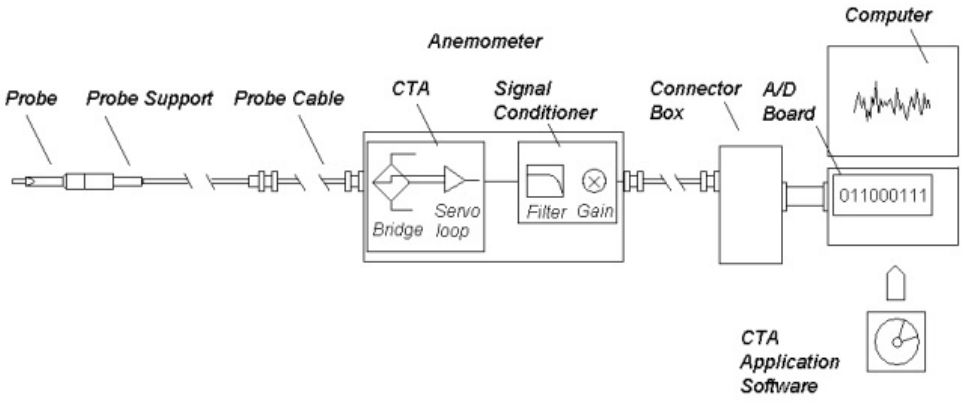

Figure 8.1: Work Flow Process of the Hot Wire Anemometry System[14].

From the hot-wire voltage, the raw output voltage E_o signal from the hot-wire is conditioned by a power amplifier to be between -5V and +5V (range indicated for the type of acquisition card used) for optimal signal-to-noise ratio, and is known as the bridge voltage E_b (see Equation 8.1).

$$E_b = \frac{E_o}{\text{Gain}} + \text{Offset} \tag{8.1}$$

Data acquisition from the IFA 300 system is performed through a analogue-to-digital card (with a known 12 bit rate) to a PC. The bridge voltage is converted to binary numbers B (digital) signals according to Equation 8.2.

$$\begin{aligned} B &= 2^{12} \cdot \frac{E_b - 5}{5 - (-5)} \\ \implies E_b &= \frac{B \cdot 10}{2^{12}} + 5 \end{aligned} \tag{8.2}$$

Therefore, by reading the binary signal from the computer, the bridge voltage can be obtained.

2.1 Temperature and Pressure Correction

Before E_b can be used to compute the corresponding velocity, the flow properties during the measurement campaign maybe different from the conditions present during the calibration process. The temperature correction is accounted to obtain the corrected bridge voltage $E_{b,corr}$. In Equation 8.3, T_w is the operating temperature of the hot-wire and known from the manufacturer to be 250°C, while T_{amb} is the mean flow temperature during the sampling time.

$$E_{b,corr} = E_b \sqrt{\frac{T_w - T_{calib}}{T_w - T_{amb}}} \tag{8.3}$$

With $E_{b,corr}$, the corresponding velocity V is computed from the calibration curve and then corrected for the difference in pressure between the measurement campaign P_{meas} and the calibration process P_{calib} using Equation 8.4.

$$V_{corr} = \frac{P_{calib}}{P_{meas}} V \tag{8.4}$$

2.2 Calibraton of the HWA

Calibration of hot film would allow the user to express the the flow speed V of the bridge voltage E_b. The hot film probe is fixed to the probe support and mounted onto the `TSI Model 1127 Manual Velocity Calibrator` (see Figure 8.2). The calibrator's pressure vessel is connected to a secondary nozzle, then to a settling chamber and finally the exit nozzle. The calibrator system comes with three different sets of secondary nozzle to optimally calibrate different velocity ranges using the same pressurised air system. In this experiment, only the `Nozzle 1 set` (a straight pass attachment) was used as the secondary nozzle, as the recommended velocity range was suitable for the expected values (between 1 and 8 m/s) to be measured.

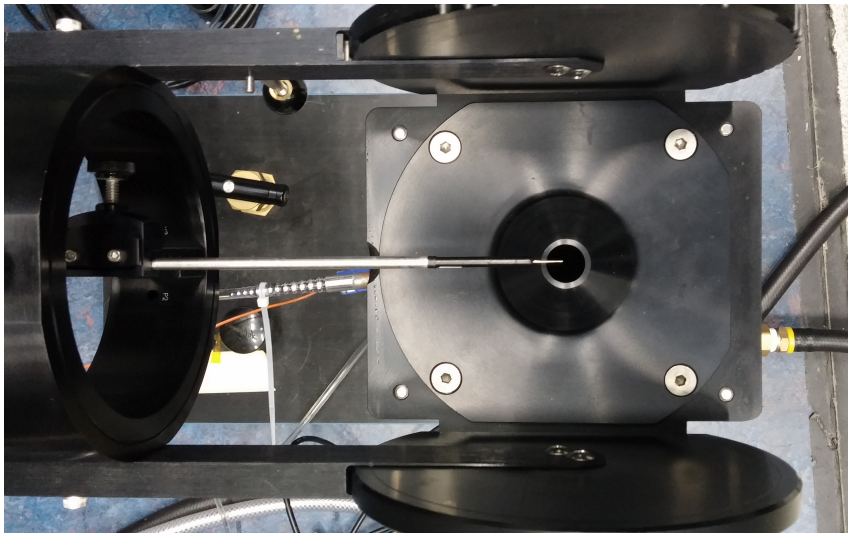

Figure 8.2: Hot Film Calibration using the TSI Model 1127 Manual Velocity Calibrator.

The flow speed at the nozzle is indirectly varied by through the adjustment of the pressure in the pressure vessel. By measuring the difference in pressure ΔP of the flow in the settling chamber and the exit nozzle using a digital manometer, and the temperature of the flow with a thermocouple, the nozzle velocity can be derived through the use of isentropic relations (see Equation 8.5 to Equation 8.7), where γ and R are known constants.

$$M = \sqrt{2\,\frac{\left(\frac{p+\Delta p}{p}\right) - 1}{\gamma - 1}} \tag{8.5}$$

$$a = \sqrt{\frac{a_o^2}{1 + \frac{\gamma-1}{2}M^2}} \quad \text{where} \quad a_o = \sqrt{\gamma R\,(T + 273.15)} \tag{8.6}$$

$$\Longrightarrow V = Ma \tag{8.7}$$

In the HWA calibration process, the reference nozzle flow velocity was varied between about 0.5 m/s and 10 m/s and the optimal gain and offset was set in the accompanying official software `ThermalPro`

that works with the hot film. The hot-wire bridge voltage response was recorded at different nozzle velocity using an in-house LabVIEW calibration program which also plots the calibration curve, E_b as a function of the reference velocity.

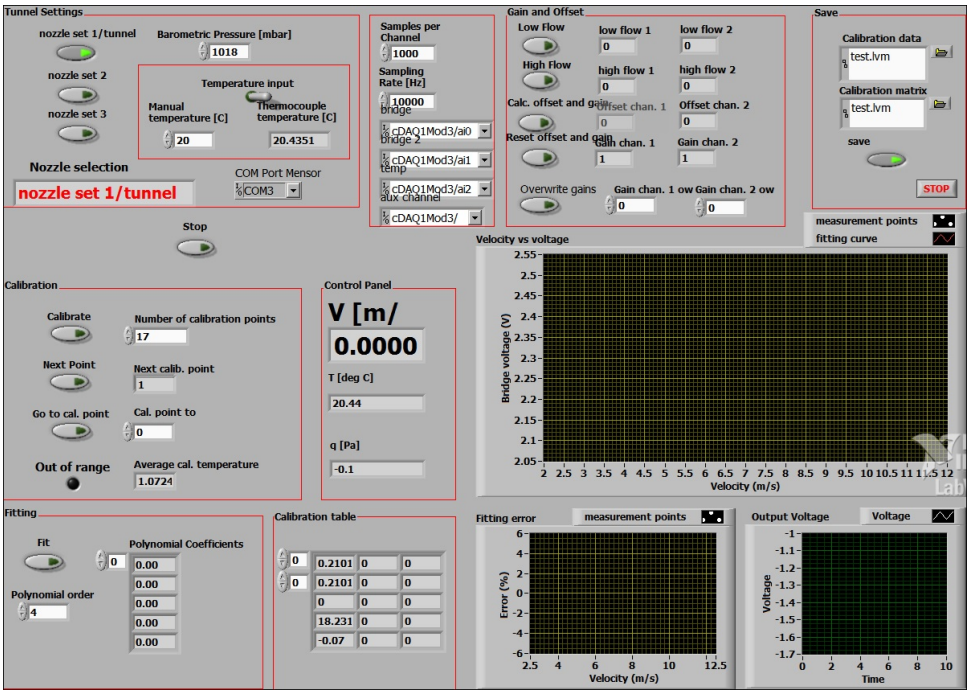

Figure 8.3: Dials of the Front Panel of the LabVIEW Calibration Program.

4th order polynomials were used to fit the measurement points. As an example, the calibration curve obtained during on 22 January 2015 is shown in Figure 8.4. It was assessed that the calibration fit is acceptable as the offset errors of the measurement points to the curve fit are less than 0.1%.

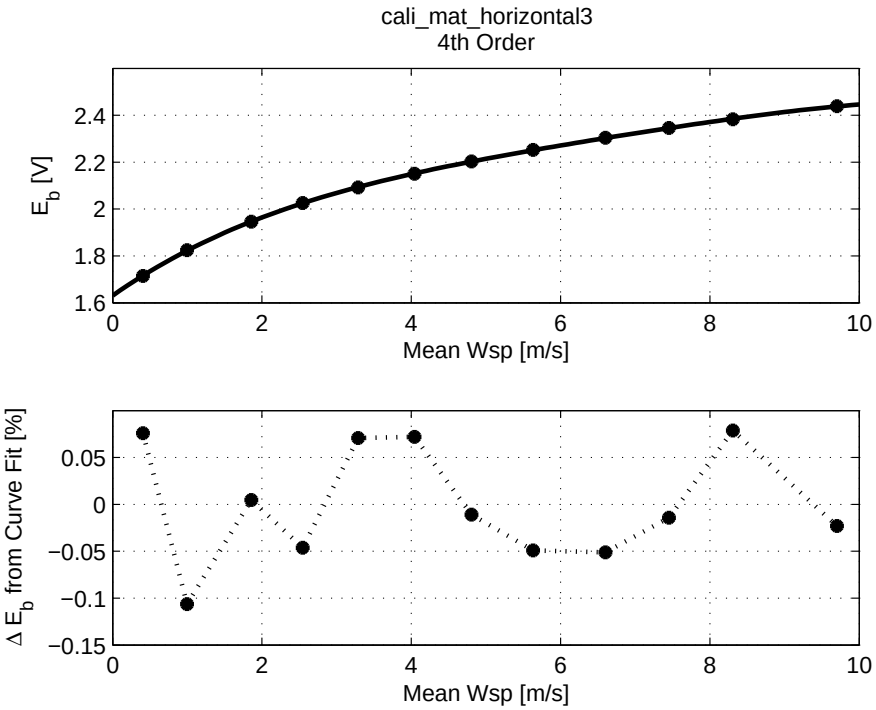

Figure 8.4: Example of a 4th order curve fit on the measurement points from the calibration data.

"Design is not just what it looks like and feels like. Design is how it works."

Steve Jobs (1955 – 2011)

9 Experimental Setup

This chapter will describe the experimental setup: namely, the considerations behind the design of the disc rotor, the wind tunnel and equipment used in the load and flow measuring techniques.

1 Design of the Porous Disc Rotor

Since actuator disc models only exists in theory, the experimental representation of such rotors would be realised through the use of porous discs. Within the timeframe of this thesis work, two porous discs of different mesh designs were tested in separate measurement campaigns.

1.1 Design Principle

From a theoretical perspective, the actuator disc represents a body force in the flow and acts on a region of the fluid is infinitely thin. In a practical sense, this would not be possible to achieve as a rotor disc would be finitely thick. The disc should also not be too thin such that the rotor becomes too flexible and yield due to the incoming flow.

Experimentally, the actuator disc is represented by a porous disc, where the axial force (or drag force) is directly influenced by the design of the holes. Since the intention of this study is to simulate a uniformly loaded rotor, the size and position of the hole placements, which have a direct influence on the load profile, have to be considered. To simulate real-world wind turbine rotors, porous disc designs to achieve thrust coefficients ranging between 0.5 and 0.9 were targeted. Aubrun, in his works [8] and [9], used metal wire meshes to create porous disc rotors, while Medici[42] and Sforza[55] used metal plates with perforated holes.

In order to study dynamic inflow effects, load variation was invoked by varying the disc's porosity. To achieve this practically, it was decided that the rotor would comprise of two thin porous discs mounted close together - where one of them would be relatively moving in front or behind the other. The magnitude and rate of porosity change would be controlled by the moving disc's displacement and speed. While two discs were used, the gap clearance between both both discs should be minimal as the aim is to simulate a single rotor.

1.2 Porous Disc Rotor in First Experimental Campaign

In the first campaign, the design of the porous disc focused on the theoretical achievement of uniform load profile in the radial directions. The disc was divided into annulus rings and azimuthal sectors, which would indirectly affect the size of the punctured holes. As the aerodynamic properties was influenced by several variables (e.g. size of holes, number of annulus and sectors etc), an iterative approach (see Table 9.1) was used. Ideally, although the number of annulus and sectors should be as high and possible to achieve continuous load uniformity, there was a practical limit due to the size of the cutting tools. In both designs, the porosity within each annulus was kept constant in order to maintain uniform loading in radial directions.

Table 9.1: Porous Discs tested in the 1st Experimental Campaign.

Material	Mesh Design	Annulus Rings	Azimuthal Sectors	Thickness [mm]	Porosity [%]
Aluminium Plate	1a Small Holes	18	36	2.0	39.6%
	1b Additional holes in 1a	18	36	2.0	46.5%
	1c Large Holes	5	12	2.0	57.0%

Mesh Design 1a

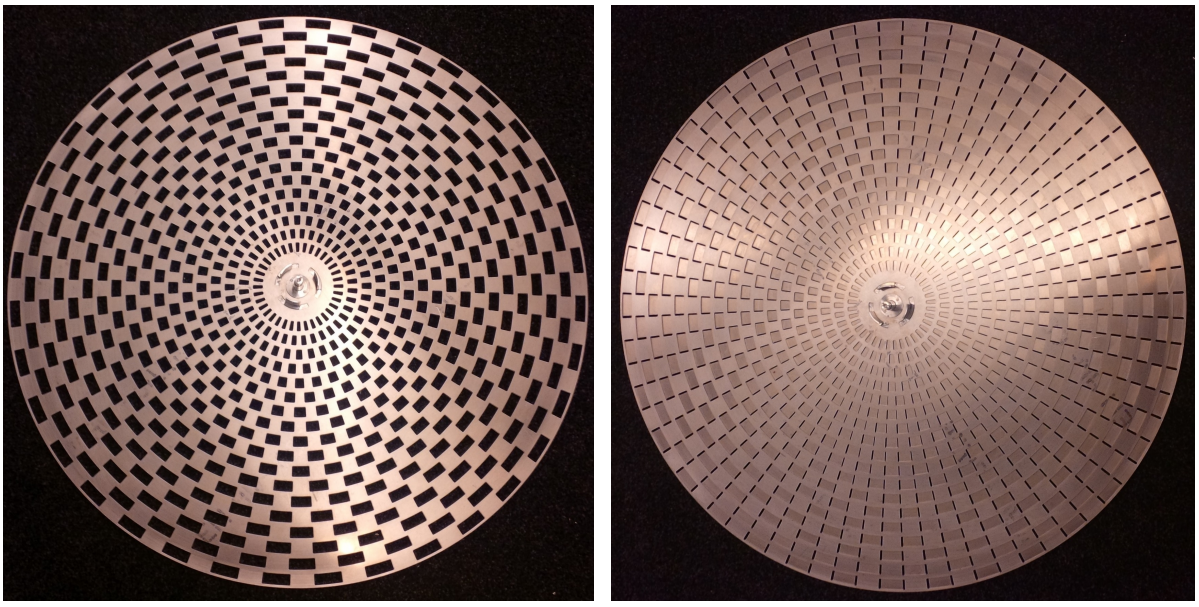

(a) High Porosity state. (b) Low Porosity state.

Figure 9.1: Mesh Design 1a: Porous Disc with small punctured holes.

Mesh Design 1b

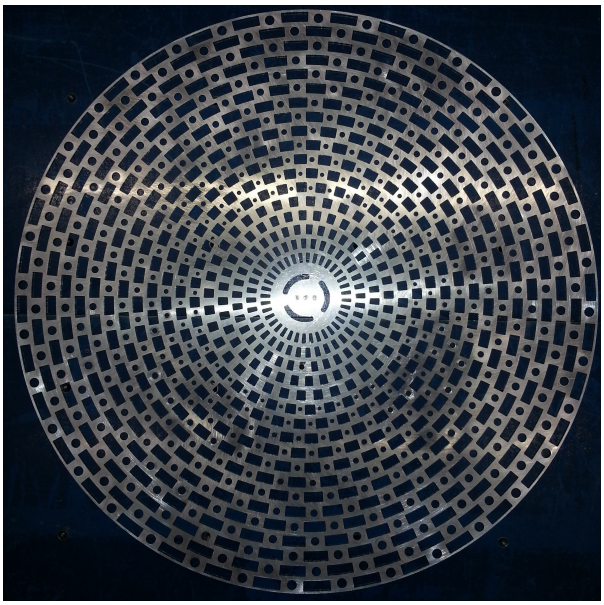

Figure 9.2: Mesh Design 1b: Porous Disc after modification of Mesh Design 1a.

Mesh Design 1c

Figure 9.3: Mesh Design 1c: Porous Disc with large punctured holes.

Wind tunnel tests showed that Mesh Design 1a exhibited a high C_T (resulting in reverse flow in the some regions of the immediate near wake), and had almost indifference to that from a non-porous disc. There was no noticeable change in the measured axial load given a maximum change in porosity. In a limiting sense, a porous disc essentially remains as a bluff body as the number of annulus and azimuthal sectors becomes infinite. This is because the holes become too small and impede the flow passage, which therefore reduces the axial loading C_T. A slight modification to Mesh Design 1a to obtain Mesh Design 1b, also did little to increase the air flow.

Thus, major design modifications were made which resulted in Mesh Design 1c, where the design was large referenced from similar work in [40]. To reduce the axial loading, the number of annulus and azimuthal sectors were reduced (see Figure 9.3). Based on the measured loads, Mesh Design 1c gave a C_T of 0.69, which was lower due to significant enlargement of the holes.

1.3 Porous Disc Rotor in Second Test Campaign

The porous discs in the first campaign were in-house manufactured by punching holes on an aluminium sheet. Their performances were compared to a earlier similar work in[36], where a porous disc rotor was constructed using 3 layers of fine wire meshes (see Figure 9.4). Interestingly, even with an effective porosity of 32%, its C_T was only 0.93 which is lower than Mesh Design 1a, which has a relatively less refined mesh.

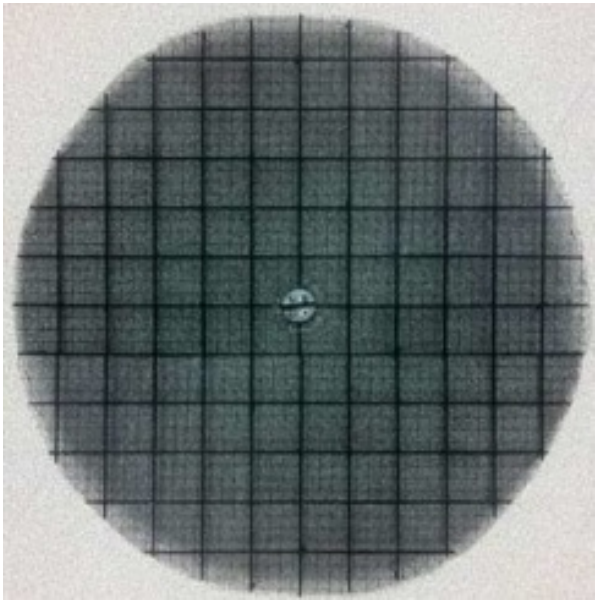

Figure 9.4: Porous Disc rotor of 3 layers of wire mesh giving an effective porosity of 32%[38].

Learning points were drawn from the porous discs used in the first test campaign. Compared to [36], it initially seemed that porosity bears no significant impact on C_T. Given that the porosity distribution was fairly uniform, it is hypothesised that the hole distribution and sizes has an influence on the drag force. From an aerodynamics viewpoint, large turbulent structures would be produced as the flow flows through a porous disc with large holes. In addition, a disc with large holes is likely to have non-uniform loading.

For the aforementioned considerations, wire meshes and plates with finer hole distribution were tested for the second experimental campaign (see Table 9.2). As opposed to the first campaign, commercial off-the-shelf products were sought as they were affordable and had an extensive range of choices for quick testing.

Table 9.2: Porous Discs tested in the 2nd Experimental Campaign.

Material	Mesh Design		Diameter [mm]	Aperture [mm]	Thickness [mm]	Porosity [%]
Stainless Steel Wire	2a	Welded	1.5	12.5	1.5	79.7%
Polyester Wire	2b	Woven	0.8	2.0	0.8	51.0%
			Hole Size [mm]	**Hole-to-Hole Space [mm]**	**Thickness [mm]**	**Porosity [%]**
	2c	Punctured	5.0	2.5	2.0	44.4%
Aluminium Plate	2d	square	10.0	4.0	2.0	51.0%
	2e	holes	10.0	2.0	2.0	69.4%

Mesh Design 2a and 2b

Stainless steel wire meshes were tested. It was initially thought this design would be appropriate for this study as structure of the stainless steel disc would be sufficiently stiff and provide a rather high porosity within a fine mesh. However, during the shaping and cutting of the wire mesh into a disc, there was invariably some deformation which caused uneven gap clearance between the fixed and moving discs.

Using wire meshes, there were practical difficulties in mounting both fixed and moving discs with minimal gap clearance, whose distance was of the same order of magnitude as the aperture. The influence of the gap clearance between discs vis-a-vis the hole size, on the C_T was confirmed by wind tunnel tests. It was noted that there was almost no load change response, even in the case of a maximum change in porosity.

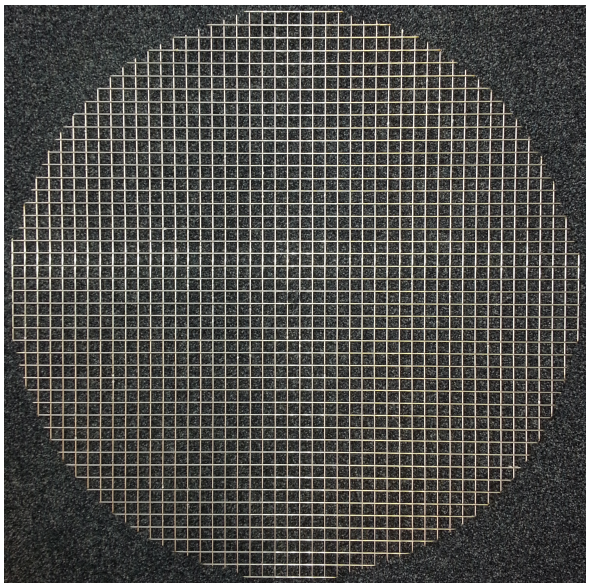

(a) Mesh Design 2a: Stainless steel wire mesh - High Porosity state.

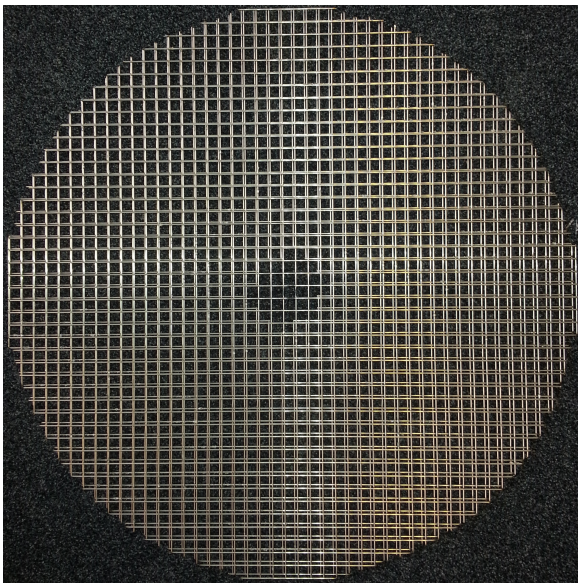

(b) Mesh Design 2a: Stainless steel wire mesh - Low Porosity state.

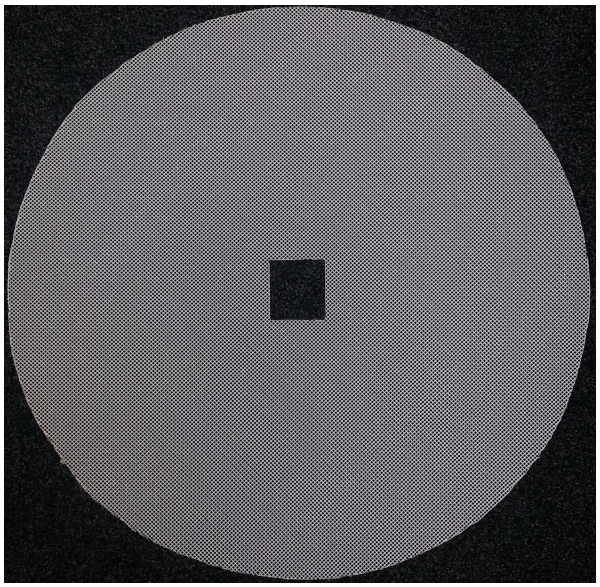

(c) Mesh Design 2b: Polyester wire mesh.

(d) Mesh Design 2a+2b: Polyester wire mesh supported by Stainless steel wire mesh.

Figure 9.5: Unsuitable Mesh Designs 2a and 2b tested in the 2nd Experiment Campaign.

Mesh Design 2c and 2d

The second campaign also sought the use of aluminium plates with square holes uniformly distributed in the z-y directions. Porous discs made using this material were of good fidelity as the gap clearance between fixed and moving discs were kept to 1 mm or less, which was about 1 order of magnitude lower than the hole size. For Mesh Design 2c, the C_T was still too high as reverse flow in the immediate near wake was detected using tuft visualisation. While the C_T of Mesh Design 2d was reasonable at the high porosity configuration, it was still unsuitable as reverse flow was detected at the low porosity state.

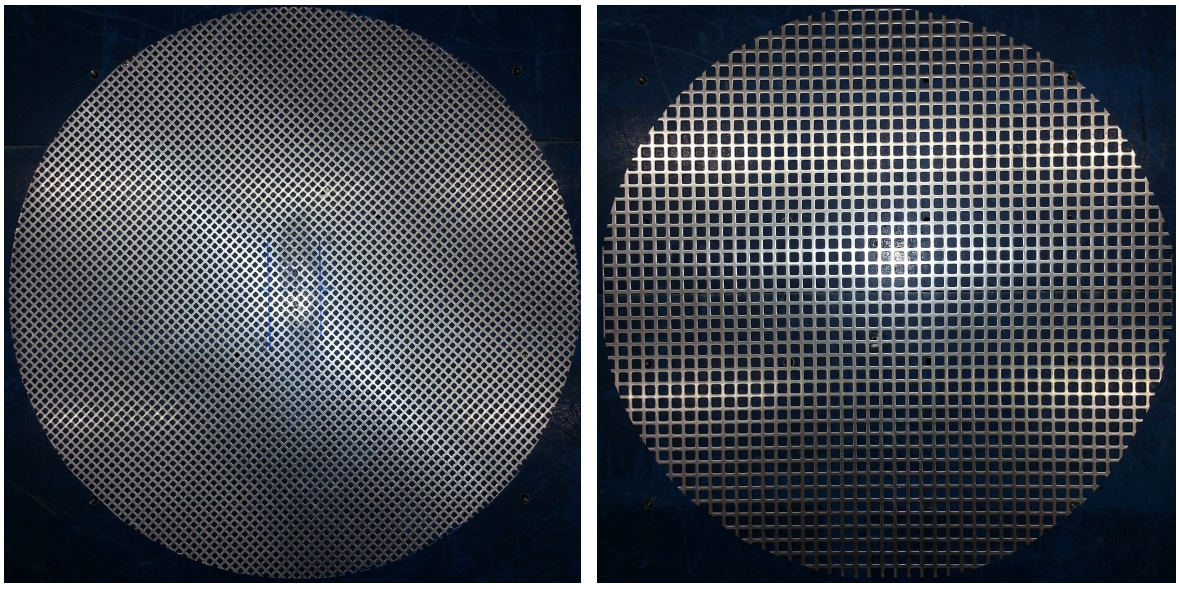

(a) Mesh Design 2c: Aluminium plate with 5 mm uniform squared holes and 2.5 mm hole-to-hole spacing.

(b) Mesh Design 2d: Aluminium plate with 10 mm uniform squared holes and 2.0 mm hole-to-hole spacing.

Figure 9.6: Unsuitable Mesh Design 2c and 2d tested in the 2nd Experiment Campaign.

Mesh Design 2e

To alleviate the problem of reverse flow during the low porosity configuration, Mesh Design 2e was used, but with a 100% increase in hole-to-hole spacing compared to Mesh Design 2d. This effectively increased the porosity by 18% to almost 70%. With this design, no reverse flow in the near wake was detected at the low porosity state. Wind tunnel measurements later confirmed the thrust coefficients of the porous rotor to be 0.61 (high porosity state) and 0.82 (low porosity state).

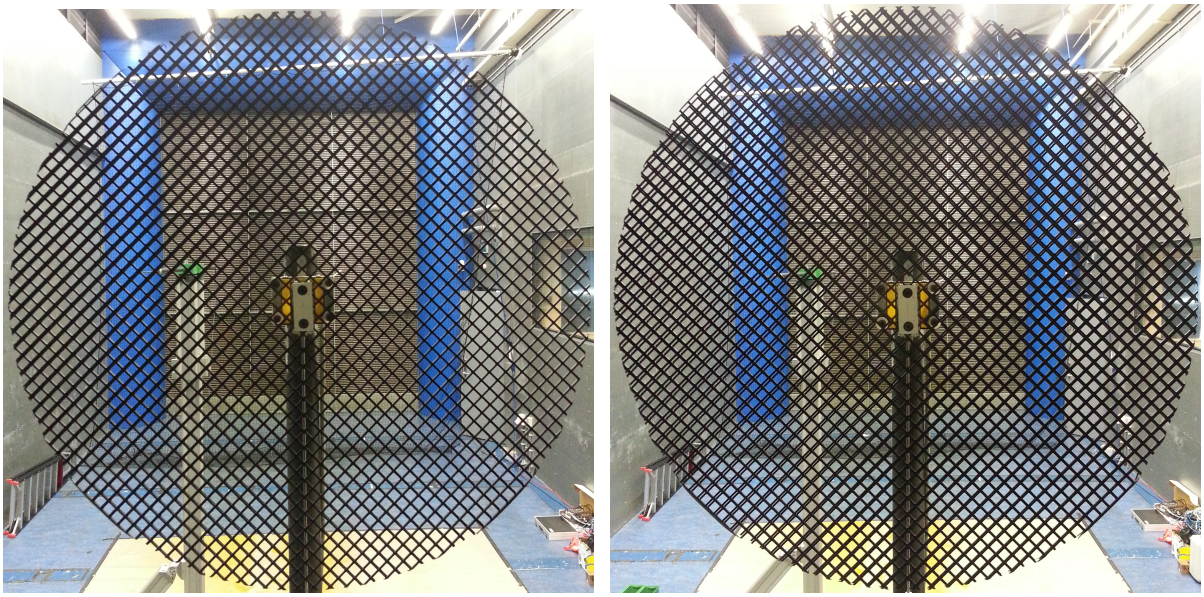

(a) High Porosity state.

(b) Low Porosity state.

Figure 9.7: Mesh Design 2e: Aluminium plate with 10 mm uniform squared holes and 4.0 mm hole-to-hole spacing.

2 Wind Tunnel

2.1 Overview

Measurements were performed in the Open Jet wind tunnel Facility (OJF). The schematic of the OJF in Figure 9.8 describes the flow acceleration by a large fan along a long diffuser and is rotated by 180 degrees using two rows of corner vanes. The flow then enters a second, but shorter diffuser before arriving in the settling chamber, where there are several dense wire meshes to reduce flow turbulence. After a smooth contraction, the flow is blown through an octagonal nozzle of size 2.85 x 2.85 m^2 to produce an even air jet stream into the test section hall of 18 m (L) x 14 m (W) x 8 m (H). The flow is then cooled by a radiator located just after the test section before being guided back to the fan[1].

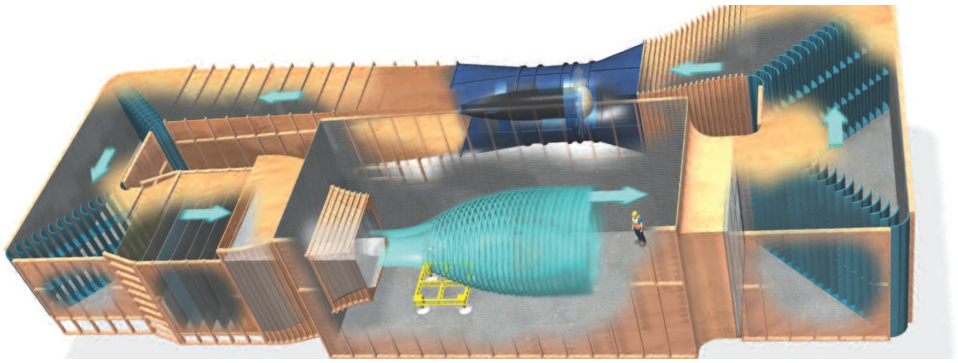

Figure 9.8: Schematic layout of the OJF.

There are two primary considerations that influence the choice of the wind tunnel type in testing rotors. Firstly, the size of the test section will affect the model scale and therefore the Reynolds Number (Re). To simulate actual flow behaviour, the Re of the test flow should be close to the actual operating conditions or above a critical number. Secondly, due to the presence of the test model, the adjacent air streams which flow past are forced away and compressed. Performing test in bounded or walled test sections results in the so-called blockage effect as the wake expansion will affect the adjacent flow outside the wake. For these two reasons, the OJF is an excellent candidate for this tests as the open-jet facility has a relatively large test section, with less than 3% blockage at the nozzle exit.

[1] http://www.lr.tudelft.nl/en/organisation/departments/aerodynamics-wind-energy-flight-performance-and-propulsion/facilities/wind-tunnel-lab/open-jet-facility-hsl/

(a) Octogonal Nozzle. (b) 500 kW Electric Fan Motor.

Figure 9.9: Components of the OJF.

The OJF is capable of produce flow a flow velocity at the nozzle of up to 35 m/s using a 500 kW electric motor. In comparison, the wind speeds of most tornadoes are less than 50 m/s.

2.2 Inflow Quality

To determine the inflow quality, the flow from the nozzle jet was measured using a hot wire anemometer at different downstream distances for several rpm settings of the OJF motor. The time-averaged axial speeds and the corresponding turbulent intensities are plotted in Figure 9.10.

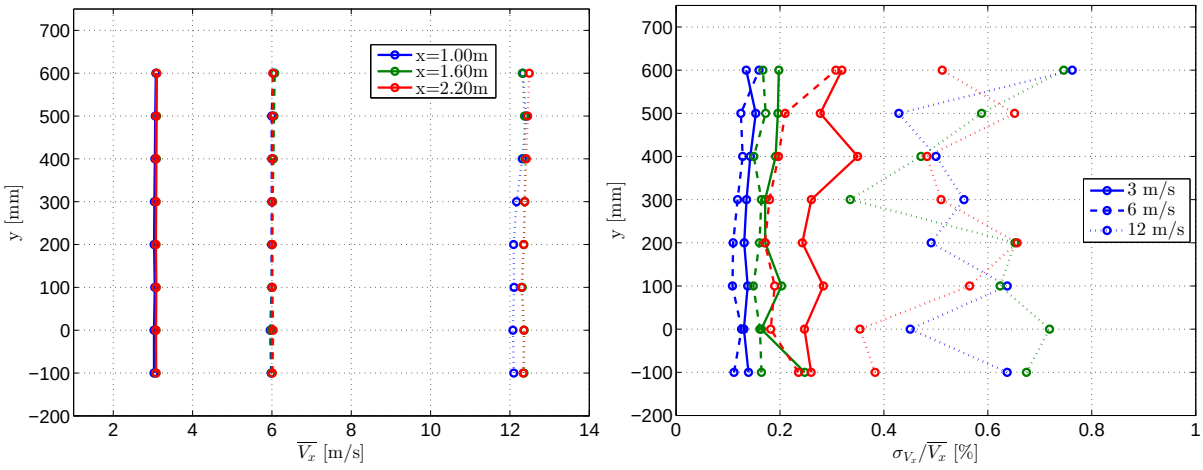

(a) Time-Averaged Velocity profiles. (b) Turbulent Intensity profiles.

Figure 9.10: Undisturbed mean velocities measured at several downstream planes from the nozzle.

3 Aerodynamics Measurements

3.1 Velocity

Hot Wire Anemometer

To accurately measure fluctuating behaviour of a flow, the sampling rate of the measuring system should be sufficiently high to avoid signal aliasing. To achieve this, the Hot-Wire Anemometer (HWA) is used. Calibration of the HWA is required to determine its response at the prevailing environmental (atmospheric pressure and temperature) settings. This means a re-calibration should ideally be conducted when there is a significant change in the ambient environment and after a period of time, since the response of the wire may change overtime. Within a day, the atmospheric pressure largely remains constant but the flow or air temperature can vary significantly due to for e.g. heating of the fan motor and the differences between the day and night air temperatures.

To reduce the need for repetitive calibration within a day, the OJF is equipeped with a heat exchanger which keeps the flow temperature stable. This will also remove the need of adjusting the fan speed in order to achieve a constant flow velocity.

Particle Image Velocimetry

The Particle Image Velocimetry (PIV) method was initially planned as the primary flow measurement technique to be used in the second campaign. Using a high speed laser, sampling rates of up to 5000 Hz could be achieved. However, during the wind tunnel experiment, the laser system encountered inherent technical faults which translated in low quality laser output. This resulted in low and uneven light intensity which was insufficient for reasonable illumination of the seed particles to show up in the photographed images. Unfortunately, the fault could not be rectified in time.

3.2 Force

The force measuring system used in the test campaigns is the `OJF External Balance B8604`. The OJF Balance was manufactured for TU Delft by the Dutch National Aerospace Laboratory and delivered in November 2008. A total six wheatstone bridges are within, which act as load sensors for the forces and moments in the three orthogonal axes (see Figure 9.11). The readings are also temperature compensated with sensors connected in a 4-wire configuration.

The balance is placed on the ground with the rotor and tower system mounted on it. The balance is capable for measuring six components, namely the forces and moments in the three orthogonal axes. Load measurements were carried out in the axial direction (streamwise) and the balance was considered to be fairly accurate with a mean error of $\pm 6\%$. The balance is contains six wheatsone bridges or load cells (two for each axis) and thus, the readings would be temperature compensated. The OJF External Balance was already pre-calibrated with the calibration coefficients given in [4]. With these coefficients, the output readings were again verified by exerting axial forces at the rotor centre using known weights.

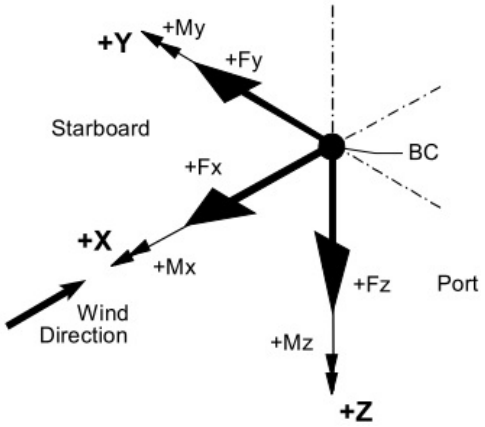

Figure 9.11: Axis Reference System for the OJF External Balance.

Under no wind conditions, it was found that the vertical movement of the motor shaft and the disc was causing mechanical loads in the streamwise direction. Since the OJF Force Balance was attached to the tower's bottom, its load measurements signals would be inherently affected by the tower's movement.

In the second experiment, a load cell mounted directly behind the rotor centre to prevent contamination of the rotor's load signals from the tower's oscillations. In this way, the load signals due to the tower's movement could be isolated. To enhance the isolation of mechanical from aerodynamic loads, the tower's structural stiffness was increased by clamping it at its mid-section.

3.3 Traverse System

A traverse system (as seen on the wind tunnel's floor in Figure 9.13) is used to mechanically traverse the measurement probe to the point of interest. Up to 3D aft the rotor was scanned to give a comprehensive insight into the wake field. Figure 9.12 depicts the measurement points taken during the experimental campaign. A spatial interval of 100 mm was taken between measurement points in the radial direction. In the shear layer, the resolution was increased to 50 mm to lend clarity on the flow field in the high turbulent region.

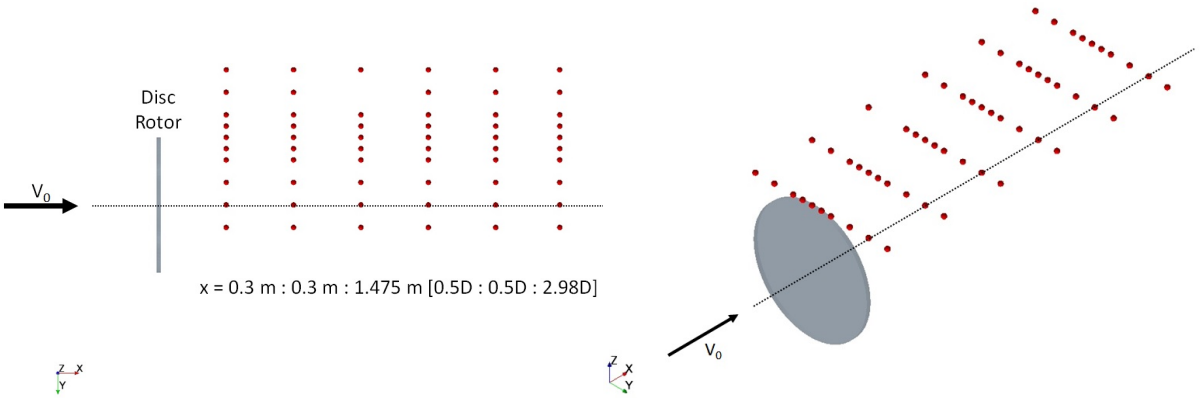

(a) Top view.

(b) Isometric view.

Figure 9.12: Schematic depicting the measurement points taken in the test campaigns.

4 Experimental Layout

Different components of the experimental setup have been explained in the previous sections. This section will describe the overall layout of these components in both campaigns.

4.1 1st Campaign

In the first test campaign, the porous discs are mounted at their centres to the motor shaft which is housed in a nacelle like structure fixed at the top of the tower. The tower is 100 mm in diameter and placed 1.5D from the exit of the wind tunnel nozzle. Made of solid steel, the tower was firmly fixed onto the free moving top of a table structure (see Figure 9.13). This movable table top has only a single degree of freedom in the axial direction, where other movement directions have been mechanically prohibited. A stiff metal rod is used to connect between the table top structure and the OJF force balance. The design of this structure ensures that the loads on the tower and rotor system is transferred, with minimal energy absorption, so that the force can be accurately measured.

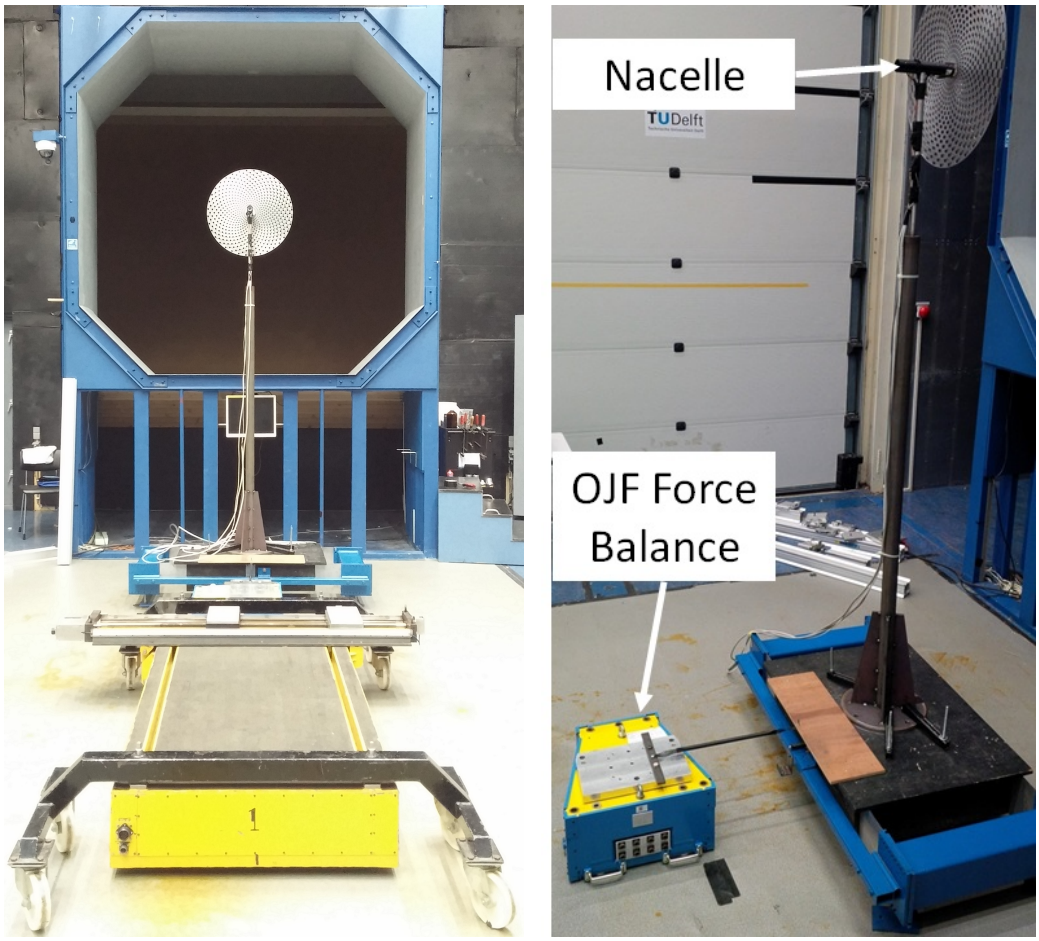

(a) Overview of setup in the 1st Test Campaign.

(b) Load transfer from the tower to the OJF Force Balance system.

Figure 9.13: Experimental Layout in 1st Test Campaign.

Porosity Control

The porous disc was mounted at the hub centre (diameter of 90 mm) to the nacelle, which is fixed on the top of a steel tower. The moving disc would be displaced by rotation on its centre axis using a FAULHABER Type 3564 K012B brushless DC-servo motor. The moving disc would rotate on the same axis of the fixed disc and the gap clearance between the fixed and moving discs was about 1 mm.

4.2 2nd Campaign

The first campaign had several shortcomings which was improved in the second campaign. Firstly, the free moving table top structure was vibrating excessively, which caused highly random fluctuating loads. These vibrations would also be undesirable as this would mean dissipation of the energy as a result of the load on the rotor, which could to lead to inaccurate force measurements.

Secondly, the porosity change actuation system was also revamped. The amount of displacement begin actuated to cause a porosity change was in the order of 0.1 mm. The rotary motor used in the previous campaign was inherently lacking in three key areas: (a) The rotary motion was subjected to shaft play. This was undesirable given the low actuation displacement and a slight change would result in an significant deviation from the prescribed value. (b) The dynamic inflow time scale $\tau = \frac{D}{V_0}$ was in the order of 0.1 s. To test under dynamic inflow conditions, a time scale of below 0.5τ[54] was suggested to observe this phenomenon. This means an actuation time of less than 0.05 s, corresponding to accelerations of about $6g$. Current market surveys suggested that no brushless servo motors would be able to achieve such a performance. (c) The default controller for the FAULHABER motor could only afford displacement-time sampling intervals of 0.1 s. This is of course not sufficient, given the short actuation time.

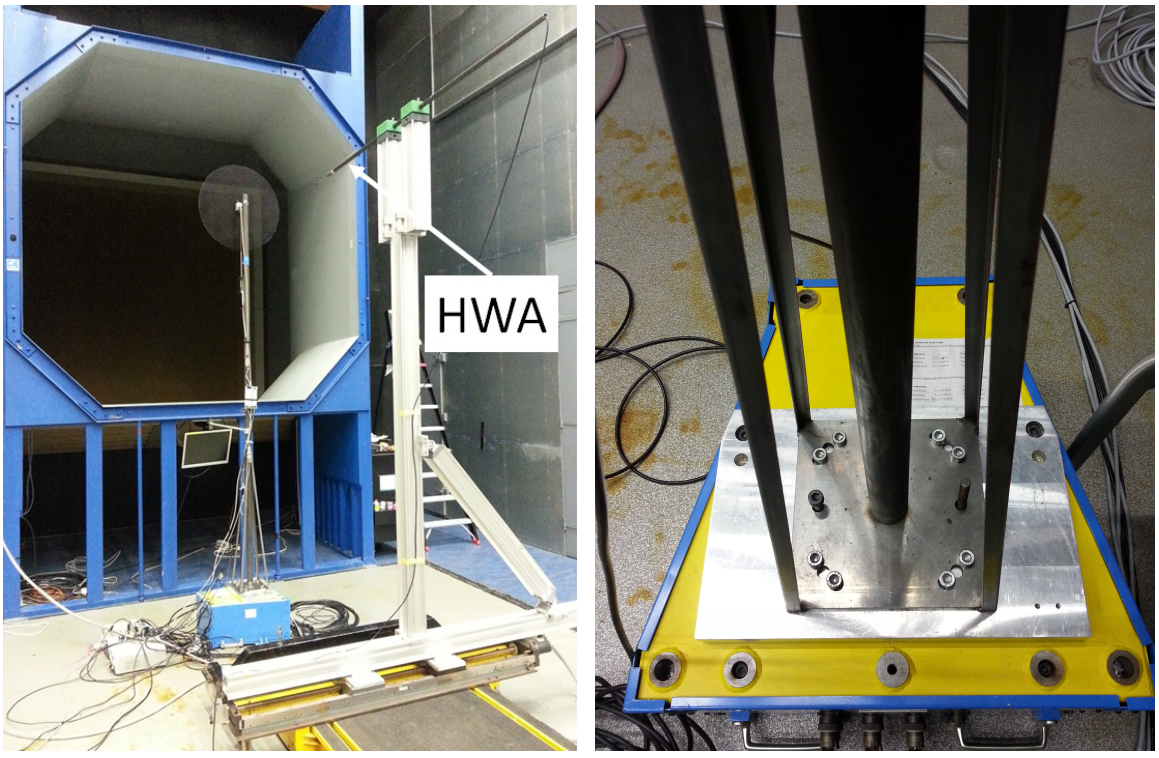

(a) Overview of setup in the 2nd Test Campaign. (b) Tower mounted directly on the OJF Balance.

Figure 9.14: Experimental Layout in 2nd Test Campaign.

Porosity Control

To dynamically control the rotor's porosity, the moving disc's displacement was actuated vertically using the SMAC LCA31-012-62CS voice coil actuator. The force provided by the motor shaft is magnetic whose magnitude is varied by the amount of current being supplied. The displacement of the rotor was highly precise, up to 0.1 μm and the control system could afford sampling intervals of up to 0.2 ms (5 ms recording intervals was chosen). The moving disc was mounted on a slider mechanism and from the slider, a rod was fixed to motor's moving shaft. The slider mechanism itself is mounted on the nacelle on which the fixed disc was also mounted.

To reduce the problem of the vibration of the table top structure, it was decided that the tower would be mounted directly on the OJF External Balance. As there is a force limit in the z-axis of 500N, the tower had to be redesigned for a lighter weight, and a diameter of 40 mm. In addition, to minimise the influence of periodic load fluctuation caused by the tower's natural vibrating frequency, a load cell was installed at the rotor axis (see Figure 9.15) and is capable of sensing uni-axial loads up to 500 N.

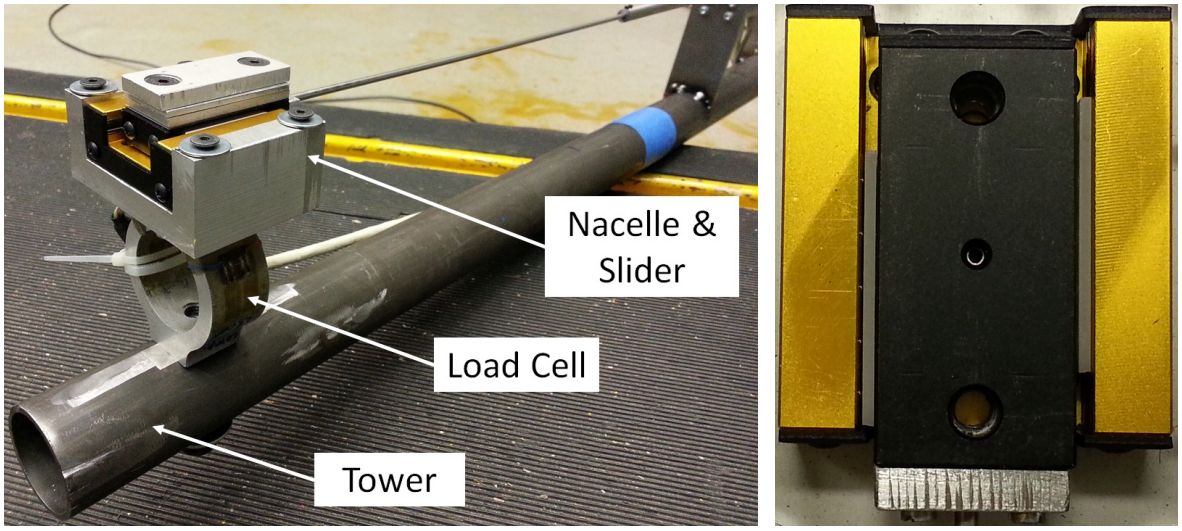

Figure 9.15: Close-up view of the rotor hub components.

Part IV: Results, Discussions and Conclusions

"Watch every detail that affects the accuracy of your work."
Arthur Charles Nielsen (1897 – 1980)

10 Description of Load Cases

1 Unsteady Load Profile

For the purpose of comparison and benchmarking, the unsteady change profile for both experimental and numerical cases were kept the same. A ramp-like change profile was prescribed in all cases, with δt representing the ramp time. In dynamic inflow speak, δt^* is the ramp time non-dimensionalised by the dynamic inflow time scale τ.

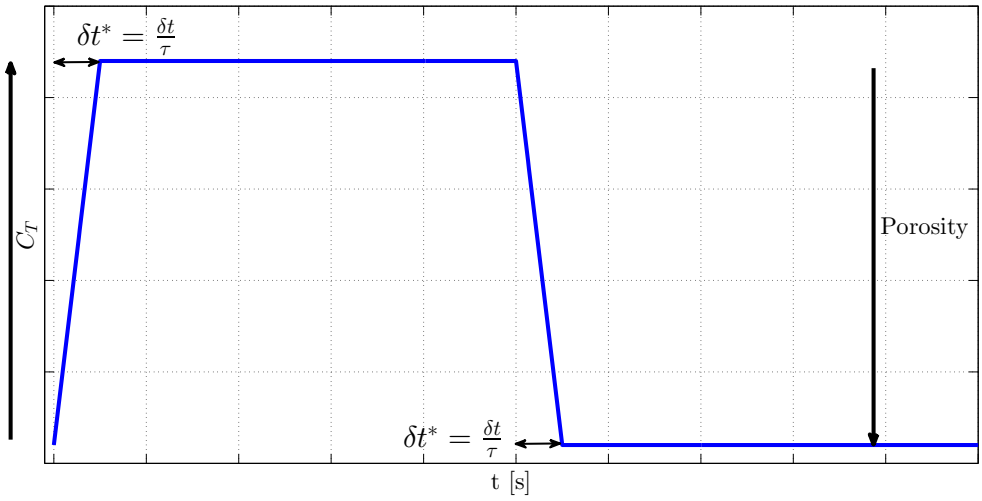

Figure 10.1: Profile of the Unsteady Load Cycle.

Table 10.1 summarises the various methods that have been adopted in this thesis. Except for the porous disc rotor, unsteady loading of the rotor is invoked by directly prescribing the value of C_T to the RANS equations or engineering models. For comparison, the result of a vortex method - the FWVR[71] is also included.

Table 10.1: Description of Unsteady Load Cases in 1st and 2nd Campaigns.

Campaign	Method	Output	Unsteady Parameter	$\Delta\theta$ [°]	δt^*
1st	Experiment: Rotory - Mesh Design 1c	Wake Velocity	Porosity	2, 4	0.1, 0.5, 1.0
2nd	Experiment: Linear - Mesh Design 2e	Wake Velocity	Porosity	N.A.	0.2, 0.4, 0.6
	3-D RANS CFD	Wake & Inflow Velocity	C_T		
	Pitt-Peters and Øye Models	Inflow Velocity	C_T		
	FWVR	Inflow Velocity	C_T		0.2

2 Low Fidelity Data from 1st Experimental Campaign

Based on Table 10.1, it was duly noted that the rotary actuation method to control the porosity was useful in creating a significant diversity in load profiles - different azimuthal rotation $\Delta\theta$ meant different unsteady load which could be permutated with different δt to give multiple test cases. While this was ideal, the movement of the rotary servo motor was unreliable as the precision and reliability of the movement steps were affected by the internal shaft play. Furthermore, the motor controller system was not capable of recording multiple cycles at high frequency so as to provide knowledge of the porosity (loading) at different phases of the unsteady load cycle. Therefore, for these reasons, only selected data from the 1st campaign was cursory analysed for general flow behaviour.

3 Quantitative Analysis on 2nd Campaign

Unlike the rotary servo motor, the unsteady load cycles invoked by the voice coil linear actuator motor were found to be highly repeatable - which was therefore suitable for the ensemble averaging technique. More importantly, the linear actuation movement could be recorded at a high sampling rate to give an accurate determination of δt^*. As such, measurement data from the 2nd campaign could was used for quality quantitative analysis. Analysis results from the measurement data could then be confidently compared against their numerical counterparts.

"Behavior is the mirror in which everyone shows their image."
Johann Wolfgang von Goethe (1749 – 1832)

11

Results and Discussion on the 1st Campaign

As explained in chapter 10, measurement data from the 1st campaign was assessed to be unsuitable for quality quantitative analysis as the porosity control and its sampling frequency was insufficient. Therefore, only general flow behaviour analysis on the wake was performed.

1 Analysis Approach

The power spectral density (PSD) estimate of each signal was computed by using the `periodogram` function in `MATLAB`. In essence, a PSD analysis measures the periodicity strength of a time series signal by decomposing the signal into harmonic signals of different frequencies. It is expected that most of the spectral energy would be concentrated at the peak frequency of around 0.05 Hz, as load cycles of period around 20s were imposed. This is shown in the PSD plots of the force time series measurement on the rotor. In the PSD analysis of the velocity time series, some of the plots did not show a distinct peak corresponding to the PSD plot of the force. For example, the flow measured at the $x/D = 0.5$ $y/D = 0$ position is directly behind the nacelle. Due to the nacelle shadow effect, high velocity gradients are created resulting in turbulent flow behaviour and flow separation across the nacelle. As a result, no distinct periodic flow is observed in the PSD plot. Further downstream away from the nacelle, the nacelle and tower shadow effects are diminished and a spectral energy peak is also observed at the corresponding frequency.

The expansion of the wake's shear layer could be inferred when one compares between Figure 11.1 and Figure 11.2. Flow in the shear layer is highly fluctuating due to the formation of turbulent eddies. As the wake progresses downstream, these coherent eddies energise the wake by entraining momentum from the outer faster moving flow. Eventually, the the distinct coherent eddies break down and the shear layer expands. This shear layer expansion also entails the increase of turbulent intensity in the flow. Since a largely uniformly loaded rotor disc is tested, vortices and shear layer is mainly produced at the disc edge. For a given radial position at $y/D = 0.42$, it can be observed that the power spectral density at the peak frequency (of around 0.05 Hz) is reducing downstream. The reason behind this phenomenon is due to the aforementioned expansion of the shear layer.

The coherence and phase differences were also derived to illustrate the co-relation of the magnitude and direction change. Using `mscohere` available in `MATLAB`, the coherence values between F_x and V_x at various points in the flow were computed. As for the phase difference, the phasor value between

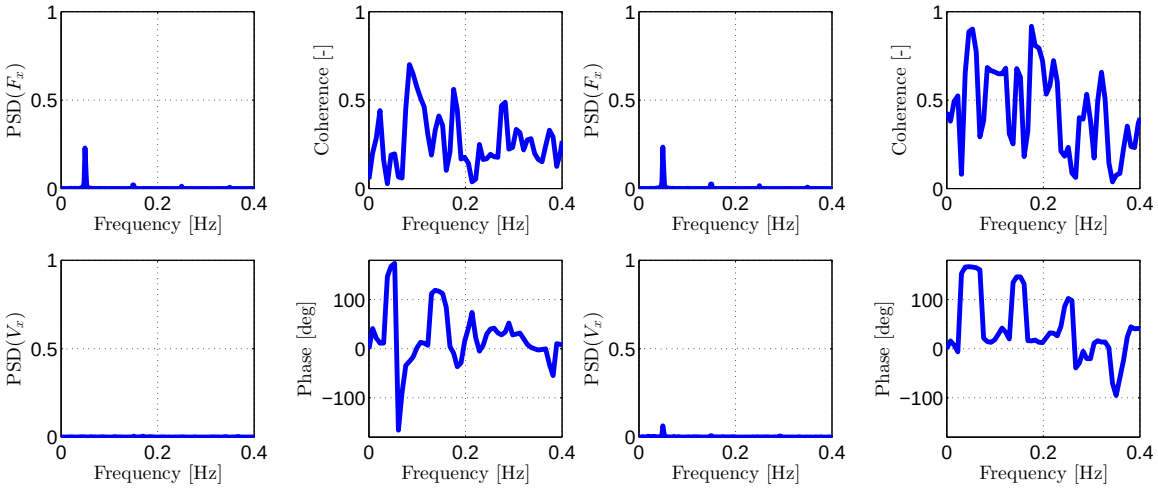

(a) y/D=0. (b) y/D=0.33.

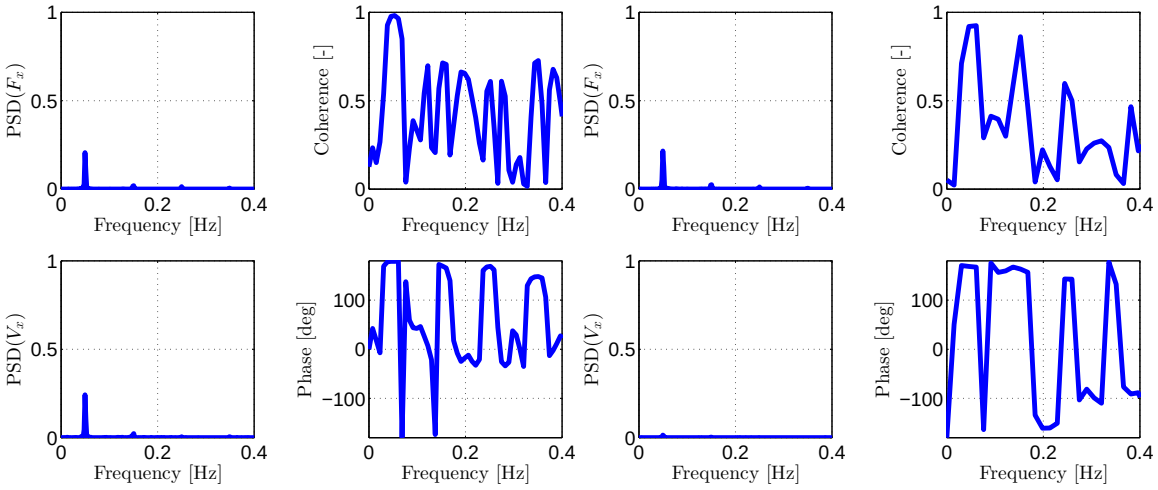

(c) y/D=0.42. (d) y/D=0.50.

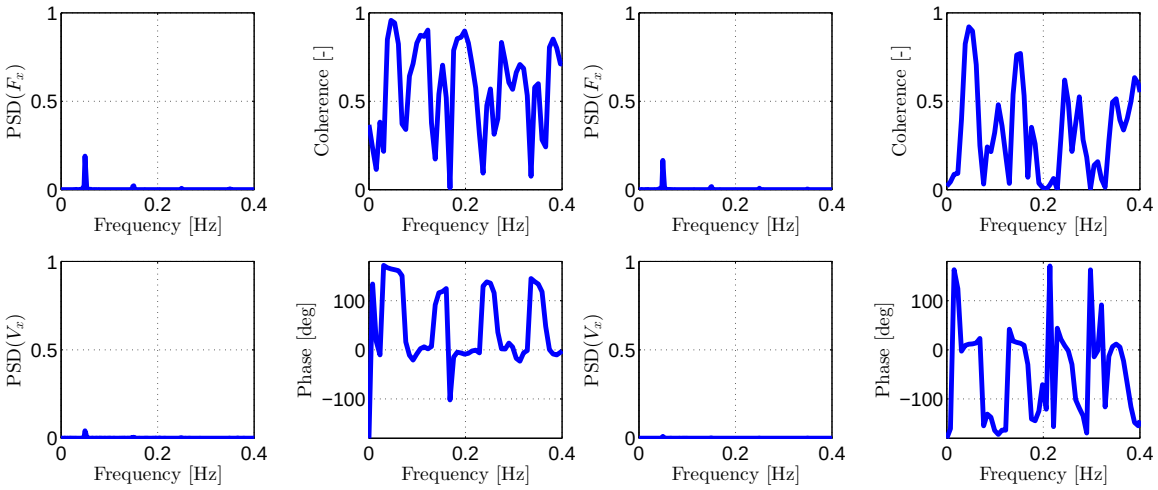

(e) y/D=0.58. (f) y/D=0.67.

Figure 11.1: Analysis between F_x and V_x at $x/D = 0.5$ of measurement data from the 1st Campaign.

the two quantities were found using cpsd and dimensionalising it in degrees °. The exact frequency of the highest spectral content from the PSD of F_x was used to determine the corresponding coherence

and phase difference at each measurement point. As an example, the values at the measured radial positions for $x/D = 0.5$ and 2.5 are plotted in Figure 11.1 and Figure 11.2 respectively.

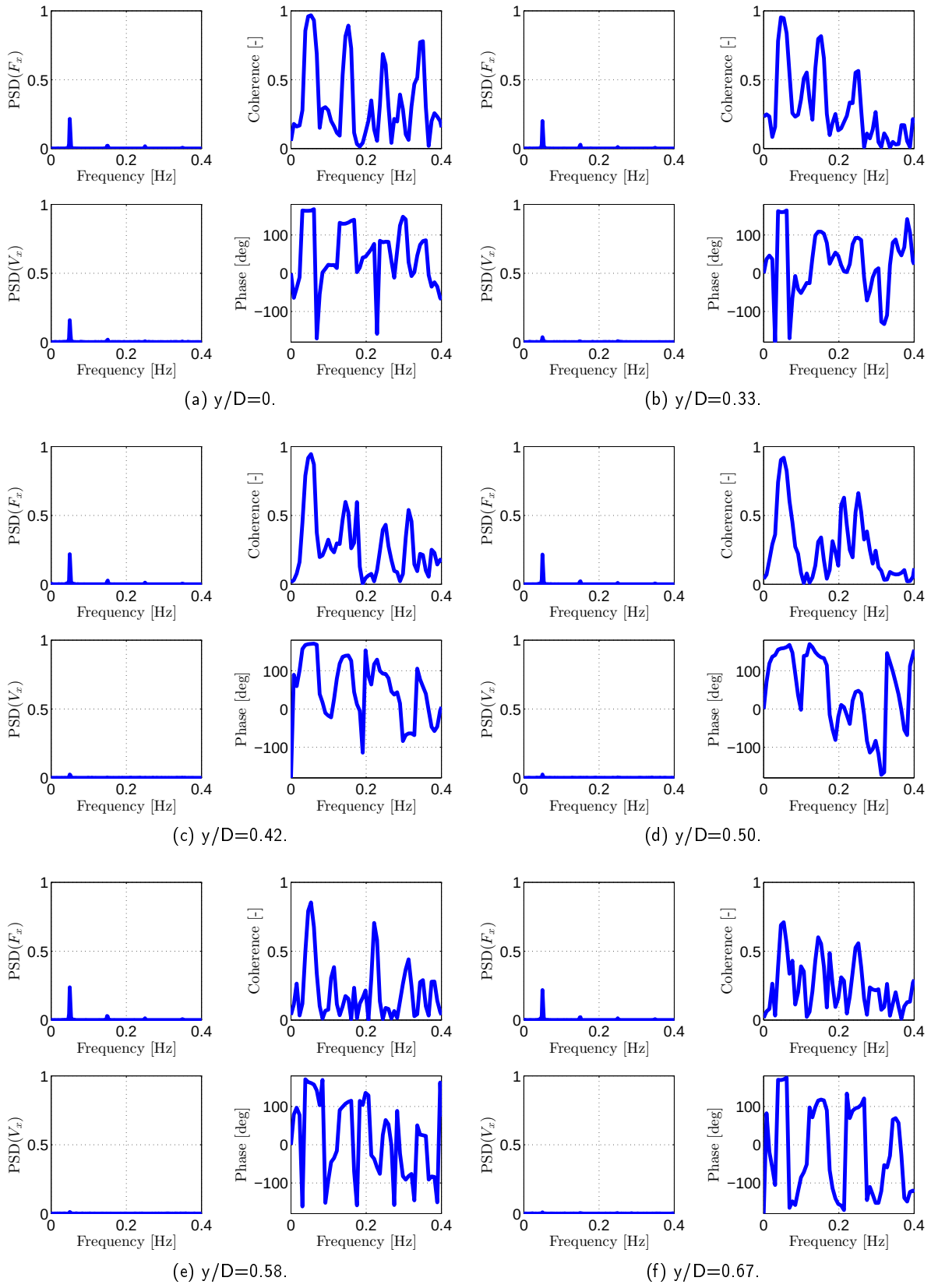

Figure 11.2: Analysis between F_x and V_x at $x/D = 2.5$ of measurement data from the 1st Campaign.

2 Results and Discussion

From the approach stated above, the corresponding coherence and phase values at the frequency maximal of succeeding downstream planes ($x/D = 0.5$ to 2.5) were plotted. The plotted results in Figure 11.3 largely corroborate to what has been earlier explained. Within the rotor's wake, there is generally high coherence between the F_x and V_x. However, at locations close to the rotor centre, there is expectedly low coherence due to the nacelle and tower shadow effect. The presence of the disc rotor causes the flow outside or inside the wake to accelerate or decelerate. This is translated into high coherence values, clearly seen between $x/D = 0.5$ and 1.5. Further downstream, the wake begins to recover, starting from wake edge towards the rotor axis, which therefore explains for the less coherence at the outer radial positions from $x/D = 2.0$ onwards.

The phase values show that the change of the flow speed in the wake is generally 180 degrees out of phase with the change of the thrust force. This negative correlation is expected since an increase in C_T would lead to a a lower speed wake. Outside the wake, the increase in the rotor's thrust on the flow leads to a larger wake expansion. With a larger blockage effect, the flow outside the wake is accelerated which translates to a positive correlation between thrust and the flow velocity.

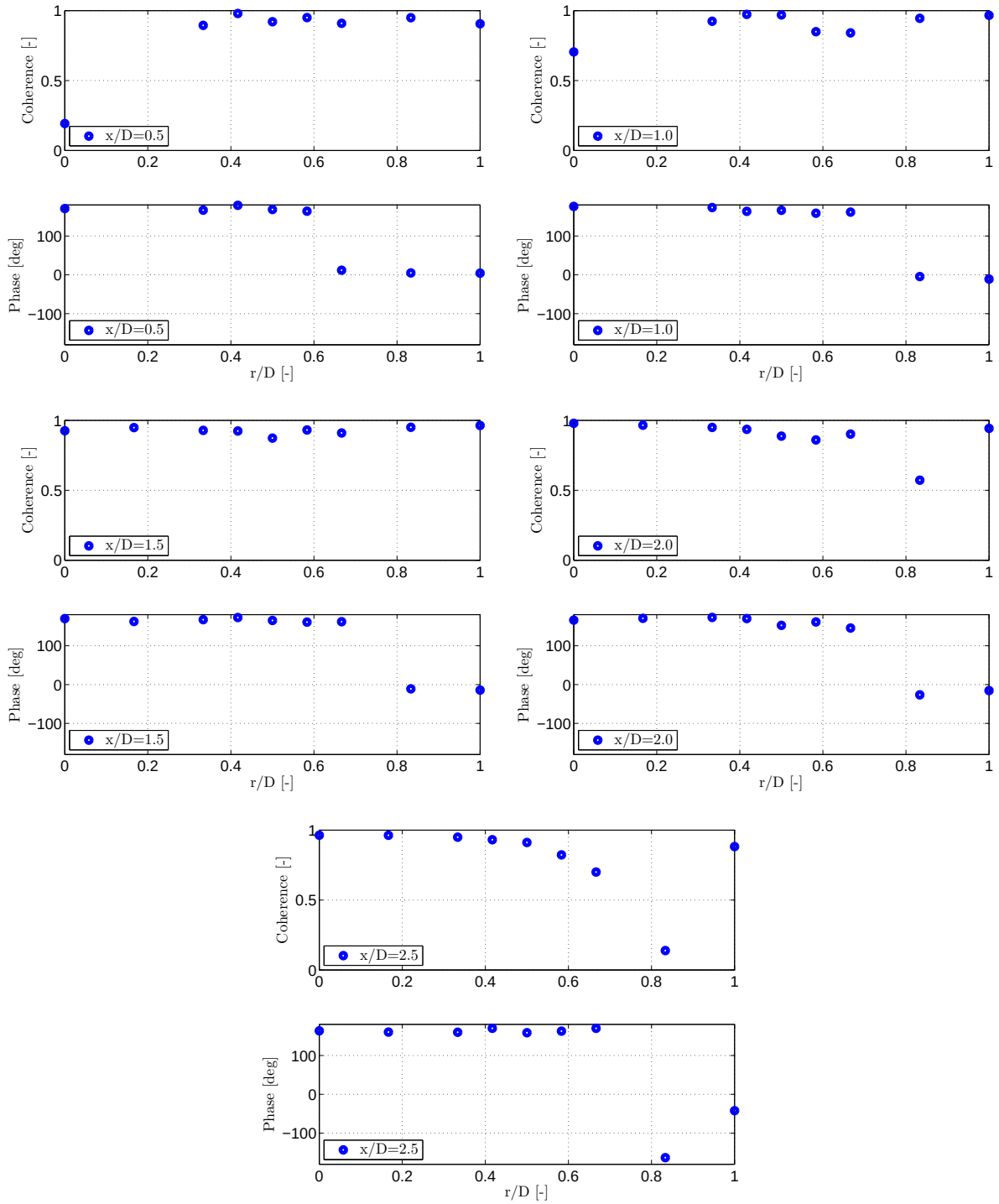

Figure 11.3: Coherence and Phase values between F_x and V_x on measurement data from the 1st Campaign.

"After a certain high level of technical skill is achieved, science and art tend to coalesce in esthetics, plasticity, and form. The greatest scientists are always artists as well."

Albert Einstein (1879 – 1955)

12

Results and Discussion on the 2nd Campaign

A comprehensive quantitative analysis was conducted for the 2nd Campaign. As the measurement data set was reliable (see chapter 10), it could be confidently used to derive the parameters (C_T and δt) to serve as inputs to the various numerical methods.

1 Steady Loading

From the experimental design, there are C_T corresponding to two porosity states. At different positions, the axial velocity was measured for 20 seconds at a sampling rate of 2000 Hz. The time-averaged velocity and turbulent intensity profiles were computed using the following two equations and plotted in Figure 12.1 and Figure 12.2 respectively.

$$\overline{V_x} = \frac{\sum_{i=1}^{N} V_{x,i}}{N} \tag{12.1}$$

$$TI = \frac{\sigma_{V_x}}{\overline{V_x}} \tag{12.2}$$

The velocity wake profile confirms what has been theoretically discussed earlier. From Figure 12.1, the velocity profile is actually non-uniform, with the region around $y/D = 0$ having a lower velocity compared to other radial positions. This significant reduction in flow speed is due to the tower shadow effect. Furthermore, the non-uniform profile is due to the effect of shed vortices released at the disc edge, causing higher velocity induction in the region near $y/D = 0.5$.

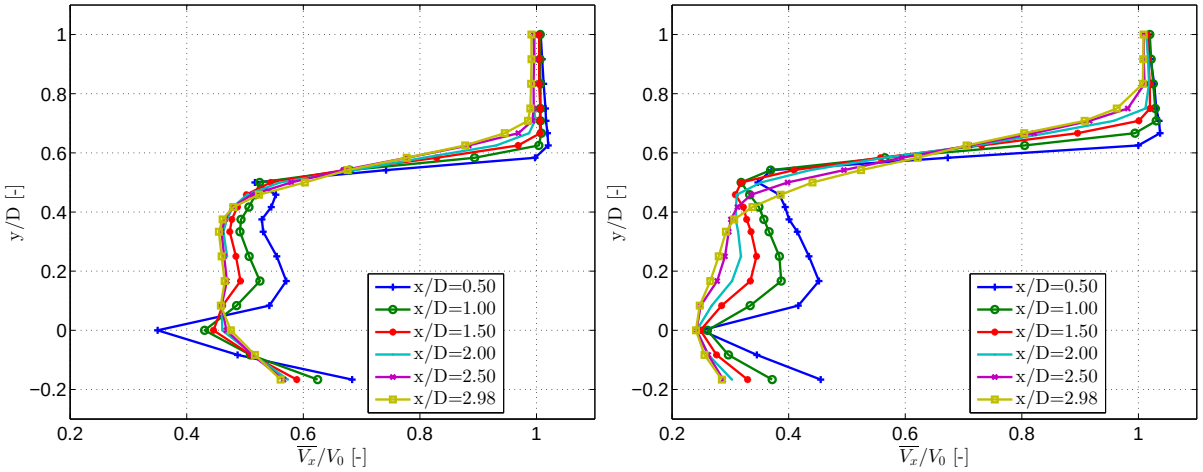

(a) High Porosity configuration: $C_T = 0.61$. (b) Low Porosity configuration: $C_T = 0.82$.

Figure 12.1: Time-Averaged Velocity Profile of the Wake of the Porous Disc under Steady Loading.

The presence of vortex particles in the shear layer is visibly present before $x/D = 2.0$, as seen in the abrupt dip in $\overline{V_x}$ beyond rising to the value corresponding to the undisturbed freestream. Beyond this plane, the spot effect has been smeared as the velocity profiles at $x/D = 2.5$ and 3.0 appear less abrupt and have lower velocity gradients at the disc edge region. The behaviour is consistent with the breakdown and expansion of the shear layer, leading to increase of turbulent intensity in the wake region. As seen in Figure 12.2, the kurtosis in the turbulent intensity begin to decrease as the wake progresses downstream. Notably, the shear layer of the rotor with a lower thrust coefficient persists longer and is relatively stable. The opposite is seen in the rotor with a higher load, which can be explained by the earlier onset of the shear layer breakdown.

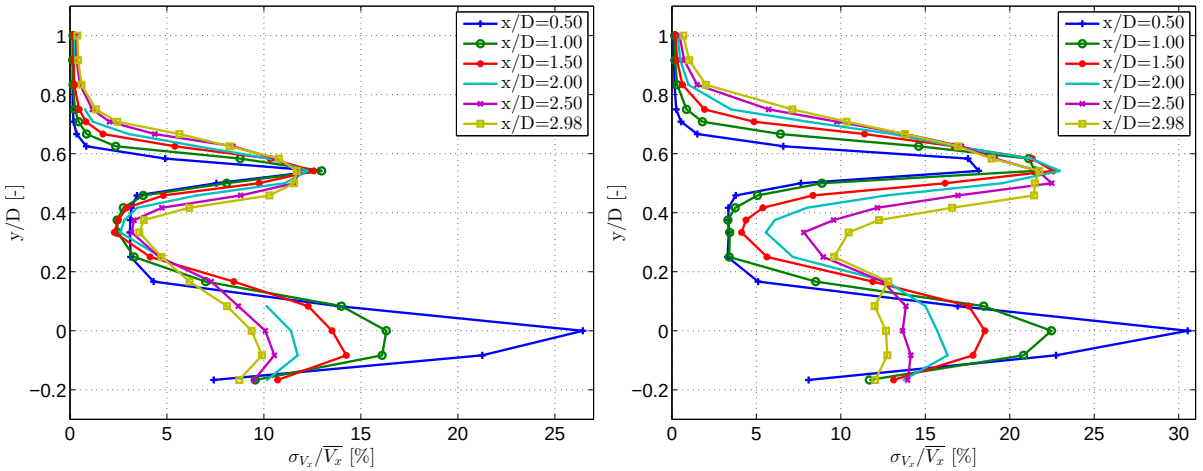

(a) High Porosity configuration: $C_T = 0.61$. (b) Low Porosity configuration: $C_T = 0.82$.

Figure 12.2: Turbulent Intensity of the Wake of the Porous Disc under Steady Loading.

The wake recovery process of rotors under different load conditions can be observed. Although no clear momentum recovery is observed even at $x/D = 3.0$, it can be argued that the wake velocity has likely approached the global minimum as the rate of velocity change in the downstream direction has decreased. Up to a critical distance (denoted as x_{crit} in Figure 12.3) from the rotor plane, the wake velocity decreases to a minimum as the flow pressure recovers to the value corresponding to

the undisturbed freestream. Beyond this distance, the momentum mixing effect becomes dominant and the wake velocity eventually recovers.

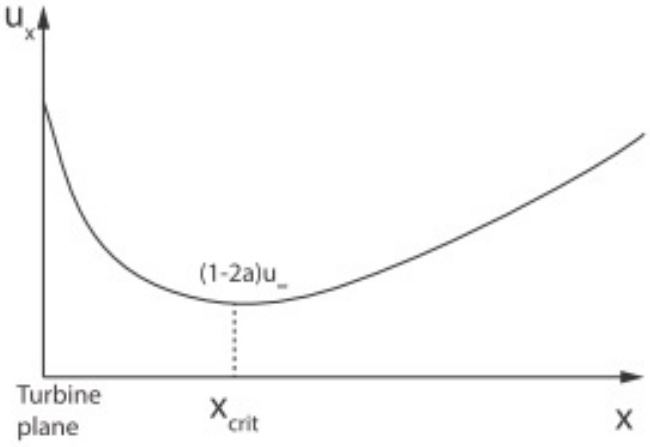

Figure 12.3: Typical wake velocity profile depicting the maximum deficit and the recovery downstream.

In Figure 12.1, some velocity recovery can already be observed at the disc edge region, which corroborates with the fact that the momentum mixing is supported by the turbulent eddies present in the shear layer which therefore results in earlier velocity recovery in the immediate adjacent region. For the low porosity configuration, which means a higher thrust coefficient, the onset of velocity recovery takes place relatively earlier when different downstream profiles are compared. This observation can be explained by the formation of the stronger turbulent eddies in the shear layer for a rotor with a higher thrust coefficient. The more turbulent eddies are more adept in entraining momentum from the freestream, which results in an earlier onset of velocity recovery in tandem with the shear layer breakdown, as mentioned in the preceding paragraph.

1.1 Comparison between Experiment and 3-D RANS

Figure 12.4 compares the wake profiles measured from the second experimental campaign and those resolved from the 3-D RANS model. Like in the aforementioned subsection, the tower imposes a significant velocity shadow in its immediate wake, whose effect is felt up to 1.5D when compared to the rotor-only computational environment. Generally, the velocity profiles predicted by numerical computations generally track experimental measurements, but with some slight global overestimation. This global overestimation could bw caused by experimental errors such as erroneous measurement of the rotor's C_T, whose value served as an input to the numerical simulations. In the measuring the rotor's C_T, it was assumed that the rotor area remains unchanged during both low and high porosity states. While the moving disc's displacement was limited to 3 mm, or 0.5% of the rotor's diameter for all measurement cases, the error in rotor area is of the 2nd order to the displacement.

At the wake edge region, numerical computations of the rotor with $C_T = 0.61$ showed relatively better agreement. This difference is likely caused by excessive flow separation at the non-uniform edges of the porous disc, whose apparent influence increase as the edges become more incongruent due to the physical displacement of the moving disc over the fixed disc (see Figure 9.7).

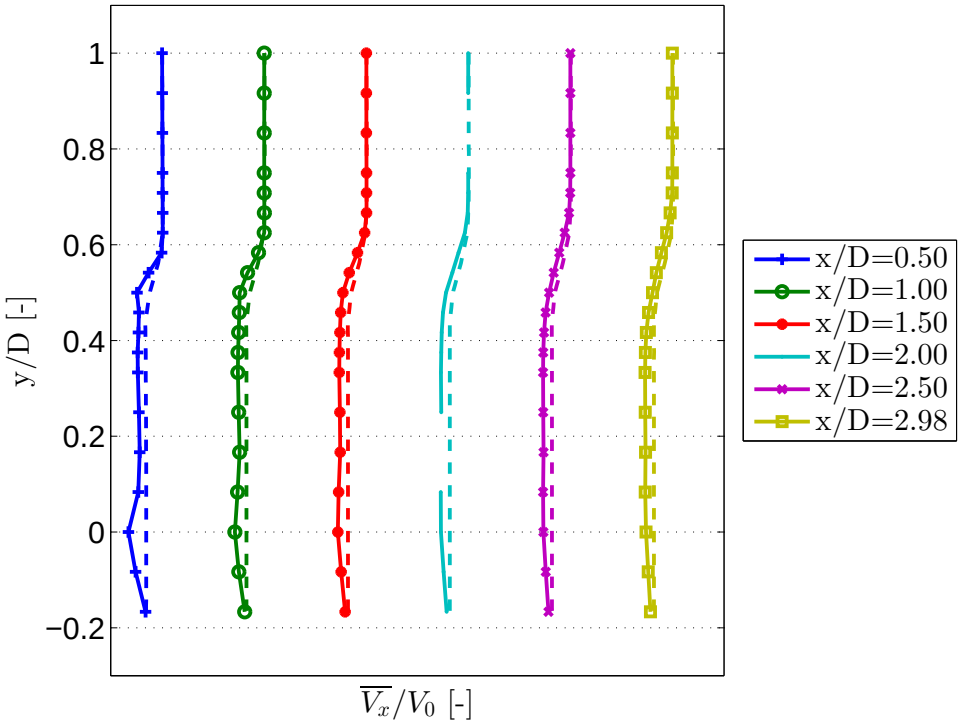

(a) $C_T = 0.61$.

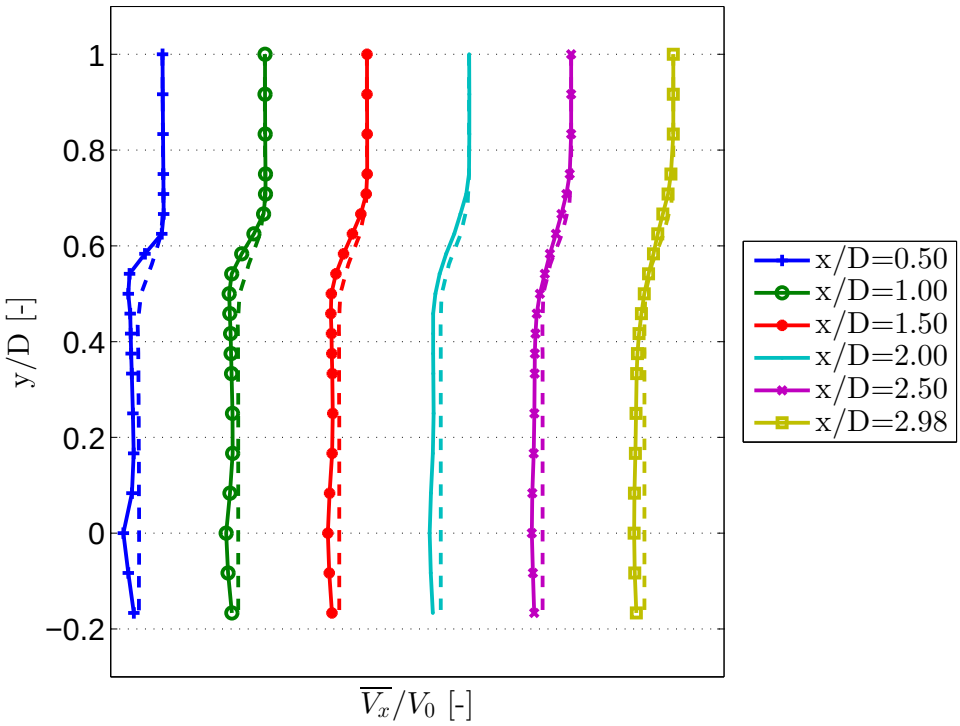

(b) $C_T = 0.82$.

Figure 12.4: Wake velocity profiles from the Experiment (−) and 3-D RANS (−−).

Comparing Figure 12.2 to Figure 12.5, one can see that the predictions of the 3-D RANS model has clearly underestimated the experimental result. This discrepancy is likely due to difference in the model setup in experimental and numerical simulations. The presence of the tower and additional perturbation due to the flow passing through holes of the mesh disc has significantly contributed to the turbulent intensity of the wake field.

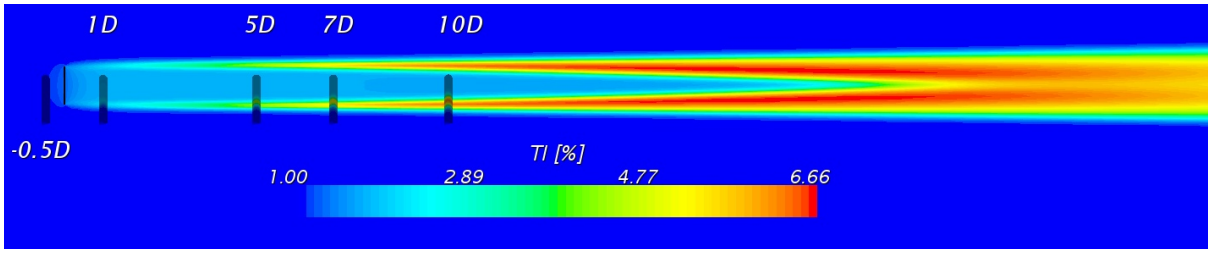

(a) $C_T = 0.61$.

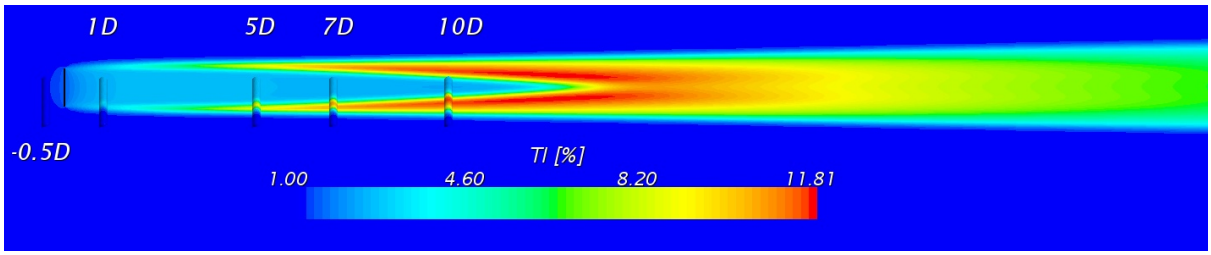

(b) $C_T = 0.82$.

Figure 12.5: Turbulent intensity contour maps predicted by 3-D RANS of rotors under steady loading (dark/translucent lines are position indicators).

1.1.1 Wake Meandering

It is widely understood that the flow over a bluff body would experience a drag force and give rise to the vortex shedding. This phenomena was studied extensively by Von Karman for 2-D cylinders or plates. For 3-D bodies such a disc, vortex shedding would also appear and has been studied by many such as Cannon[17], a Strouhal St of 0.15 was reported for solid circular discs.

A power density spectral analysis using the time resolved velocity data was done to ascertain the meandering frequency f_s. Since strong vortices were shedded at the the disc edge, it was expected that a dominant frequency would be observed from the data in and outside the wake. However, this was not case from the data that was measured in the wake, which was also reported for similar work performed in [67] and [41]. The reason for this would be likely due to the contamination of the dominant frequency by the small scale flow structures as a result of the porous mesh, and more importantly, the tower shadow effect. In Figure 12.6, power spectral plots from the downstream flow outside the wake showed a clear and discern-able dominant frequency.

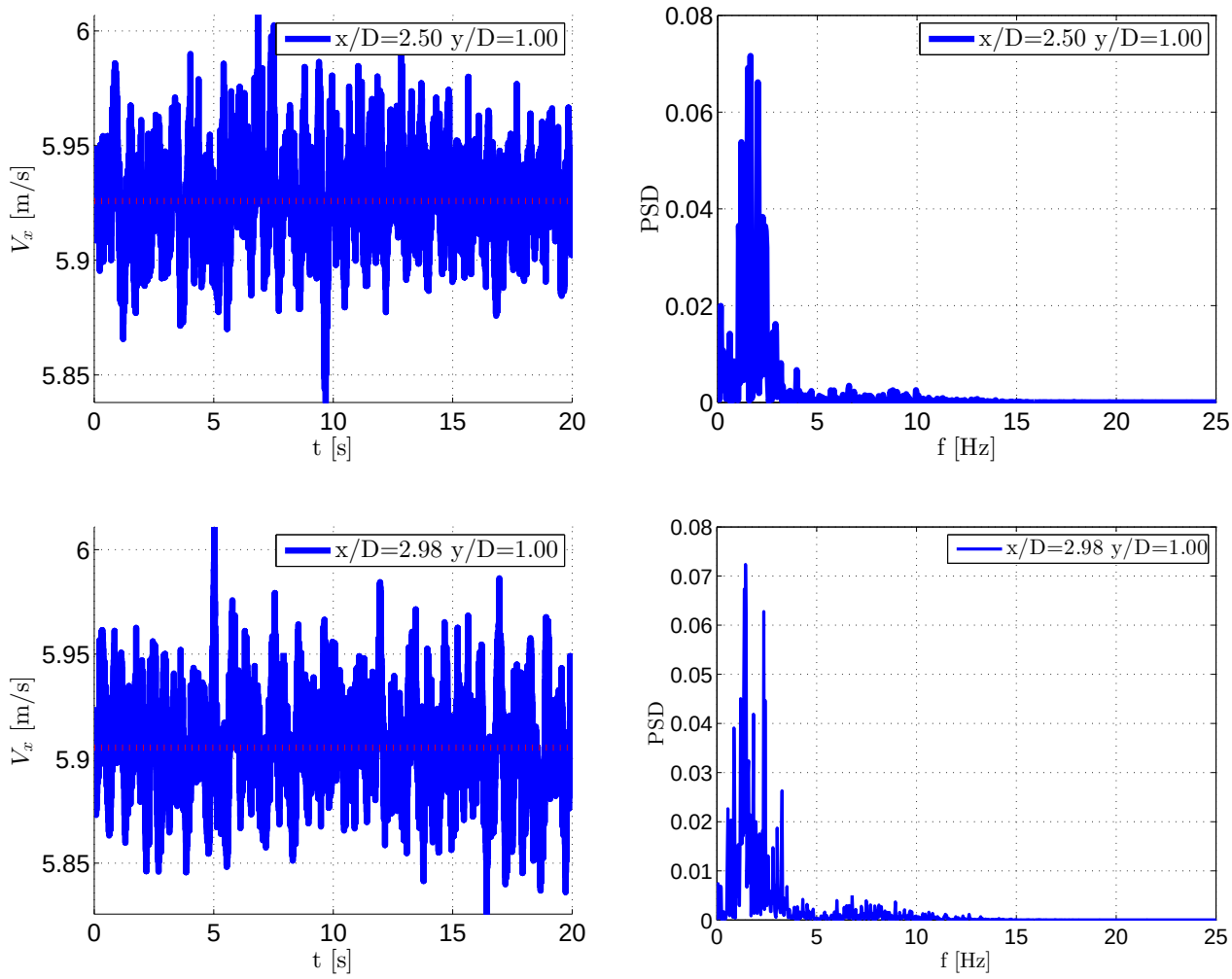

Figure 12.6: Time resolved velocity at measurement points outside the wake and the corresponding power spectral analysis showing a dominant vortex shedding frequency.

In Figure 12.6, the sub-plots on the left are the time-resolved velocity, with the right showing corresponding power spectrals. The peak frequency was found to be 1.65 Hz and 1.43 Hz at $x/D = 2.50$ and $x/D = 2.98$ respectively. Using the averaged value of 1.54 Hz, this gave an St of 0.16. This close agreement of the St for porous discs with previous experimental work for blade rotors[41] strongly suggests the periodic movement or meandering of a wind turbine wake can be closely modelled by a disc rotor.

2 Unsteady Loading

2.1 Isolating Aerodynamic Load Signals

From preliminary measurements, it was observed that sudden accelerations and decelerations of the motor shaft during porosity changes was causing vibrations in the tower structure which were also present even under no wind conditions. This was undesirable as this behaviour made it difficult to discern if the sharp overshoot in the loading of the rotor was as a result of the motor shaft's movement or an aerodynamic effect. The aim of the research was to study the aerodynamics phenomenon which

meant that the signals from mechanical or structural nature should be isolated as far as possible. To eliminate or somehow reduce this influence, the tower was further stiffened by mechanically clamping down its mid-section. Load measurements using the OJF Force Balance showed a significant damping of the transient overshoot (see Figure 12.7) during the motor shaft movement.

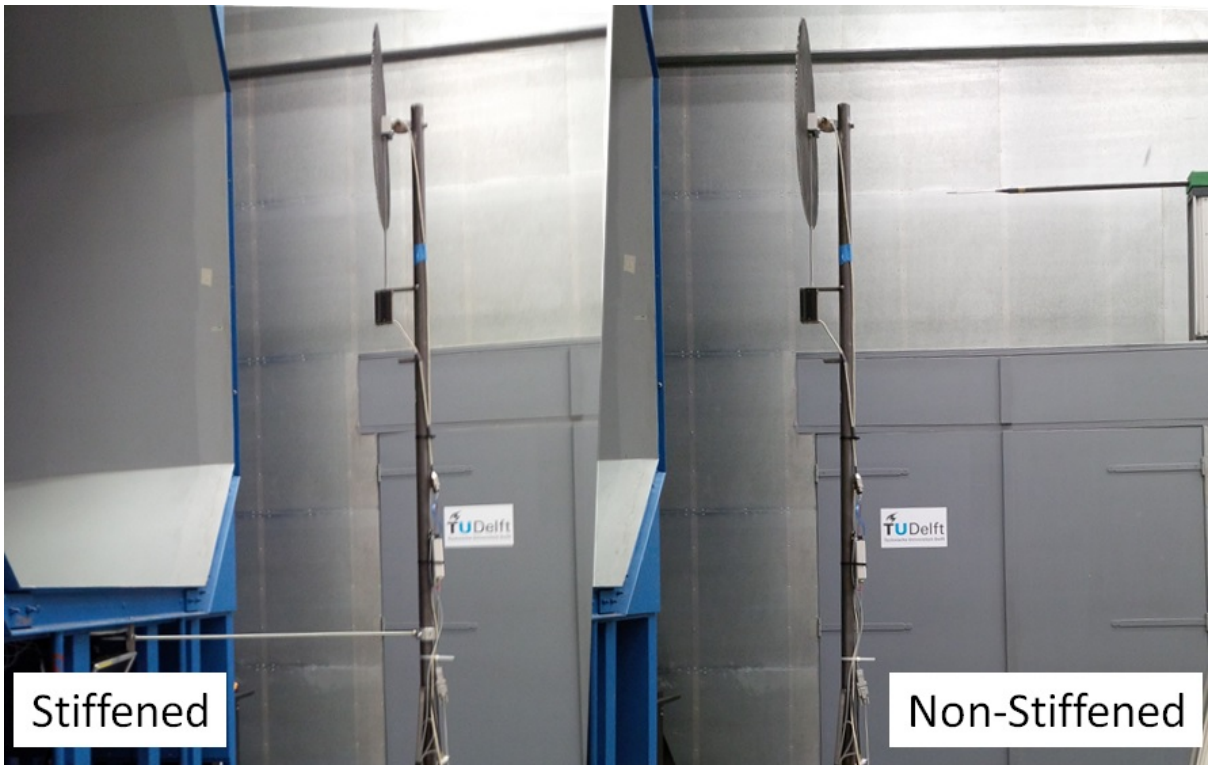

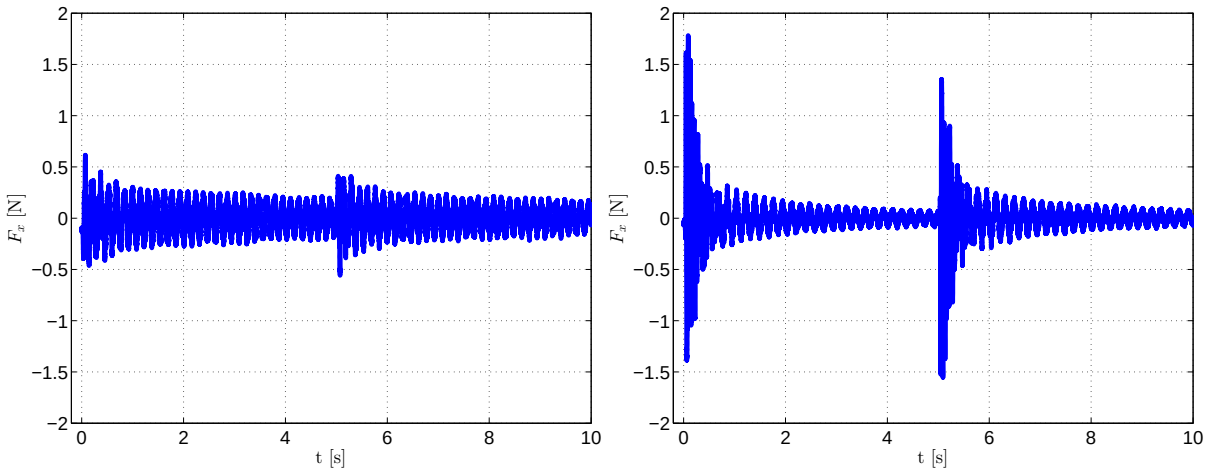

(a) Stiffened Tower. (b) Non-Stiffened Tower.

Figure 12.7: Load signals during motor operations for unsteady load cases with stiffened and non-stiffened tower under no wind conditions.

2.2 Ensemble Average Data

In the experimental campaigns, unsteady load measurements were performed by dynamically changing the porosity of the disc. Multiple unsteady load cycles were conducted consecutively, from which, the ensemble average was derived to determine the time-averaged flow and ascertain its repeatability. Ideally, a large number of cycles should be performed to the true mean values. This would be

especially important for regions with high turbulence. An error of the mean value to number-of-cycles dependency was studied at $y = 0.50$ - the shear layer region where turbulence would be significant (see Figure 12.8). Considering the limited availability of wind tunnel time, ensemble averaging of 10 cycles was decided to be reasonably sufficient as the error was less than 0.5%.

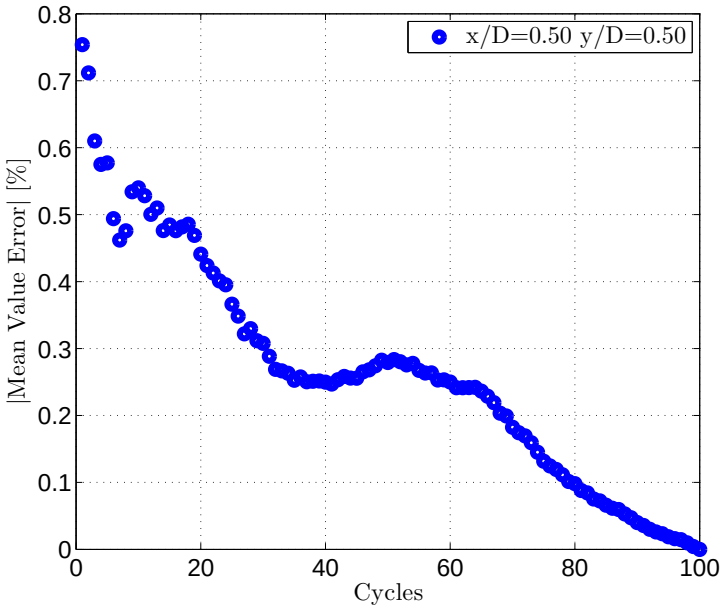

Figure 12.8: Dependency of the mean value error to the number of cycles.

As aforementioned in chapter 9, the unsteady loading of the rotor is triggered by the displacement of the moving disc which is fixed to the voice coil motor's vertically moving shaft. From the in-built sensor's readings, the displacement precision of the motor's shaft was observed to be very repeatable over the 10 unsteady load cycles during the entire test case. Figure 12.9 shows the measured shaft displacement of the motor and corresponding C_T change of the porous disc rotor.

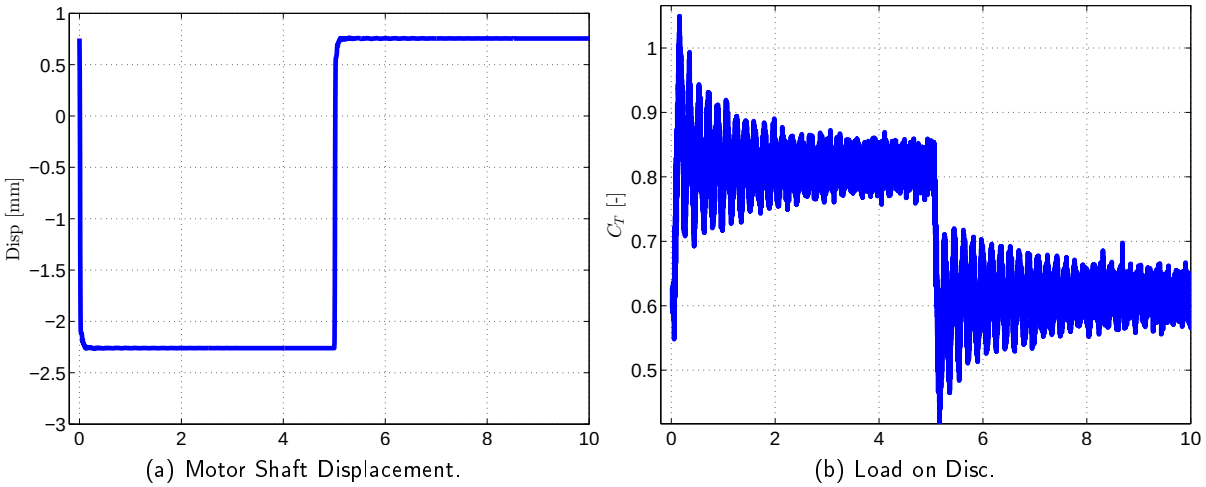

(a) Motor Shaft Displacement.

(b) Load on Disc.

Figure 12.9: Ensemble Average Time Resolved Signals for the unsteady load cycle.

Tower Resonance Frequency

In the above figure, one can clearly observe a very periodic frequency in the force measurements during the unsteady load change. The unsteady load change has excited the natural structural frequency of the entire system (mainly the tower) and thus resulting in the sinusoidal waveform that is seen in the C_T plot. The load time series of the structure under steady loading was also compared, as it is expected that the tower vibrations should also occur in both steady and unsteady load cases. This was indeed found to be true through a frequency spectral analysis and the system's resonance frequency was found to be approximately 6.5 Hz.

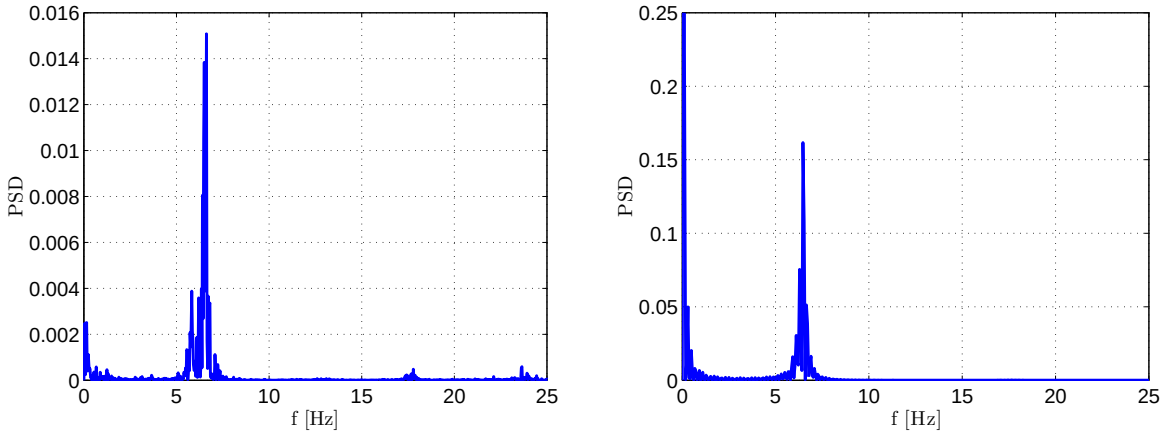

(a) Steady Load Case at $V_0 = 6$ m/s.

(b) Unsteady Load Case at $V_0 = 12$ m/s.

Figure 12.10: Power spectral analysis to determine the tower's structural natural frequency.

The time resolved velocity was measured at various points in the wake (see Figure 9.12 for measurement matrix). The time-resolved axial velocities, non-dimensionalised by V_0, are plotted in the following which will be used to describe the unsteadiness nature of the wake for a rotor under unsteady loading. The following plots serve to highlight the characteristics in three main regions of flow aft the rotor: (a) in the inner wake, (b) in the wake's shear layer and (c) just outside the wake.

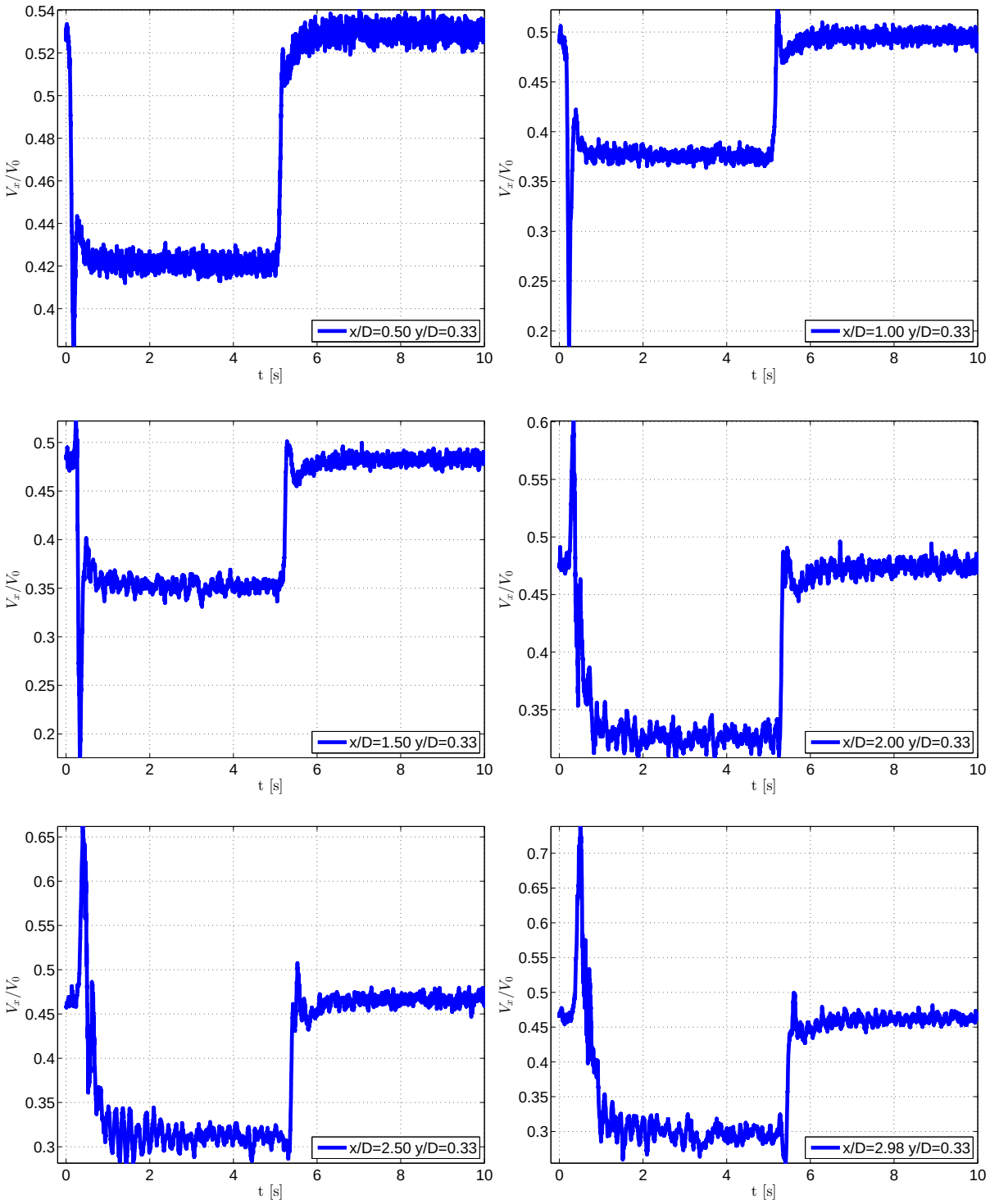

Figure 12.11: Experimental Results in the Inner Wake ($y/D = 0.33$).

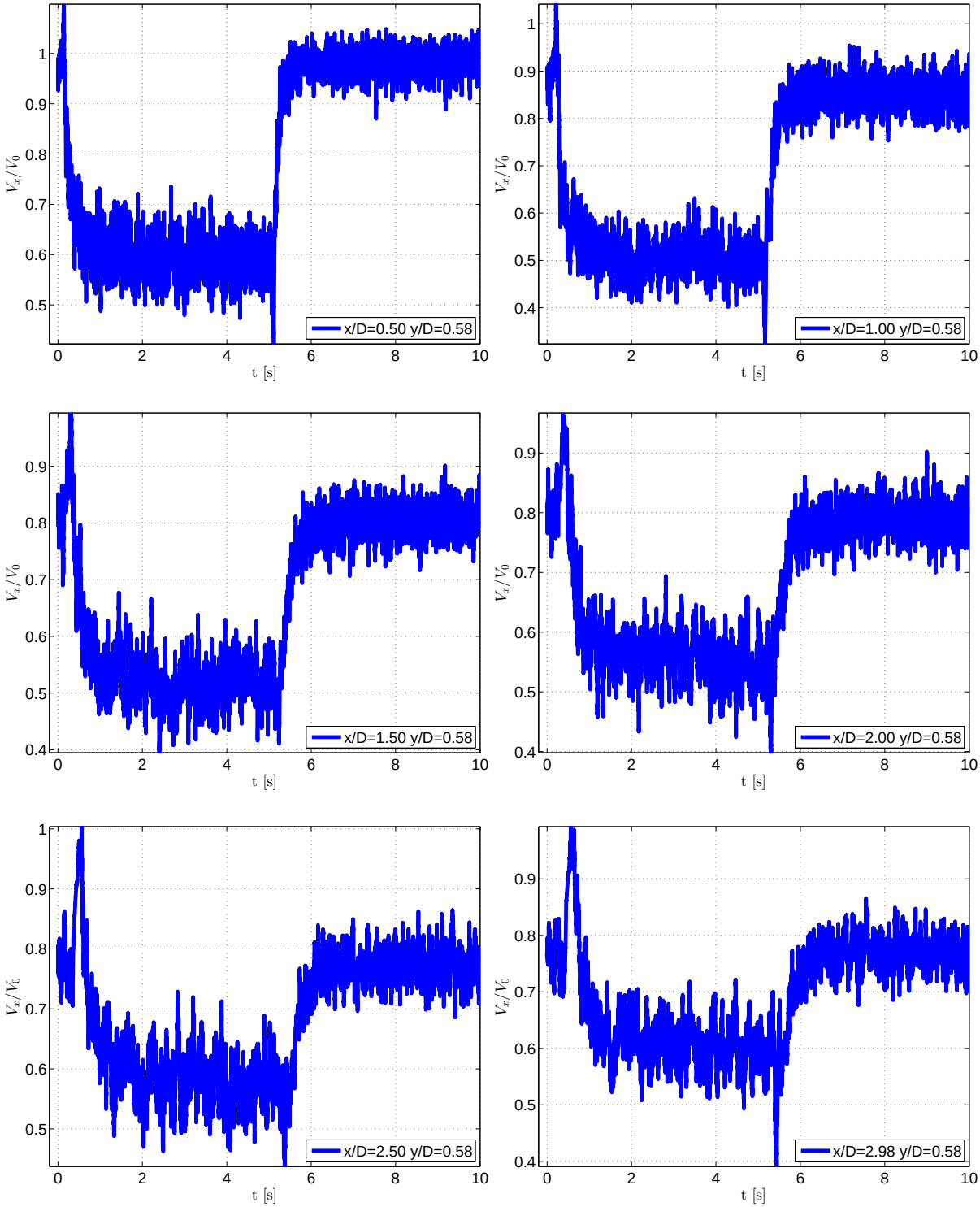

Figure 12.12: Experimental Results for the wake's Shear Layer ($y/D = 0.58$).

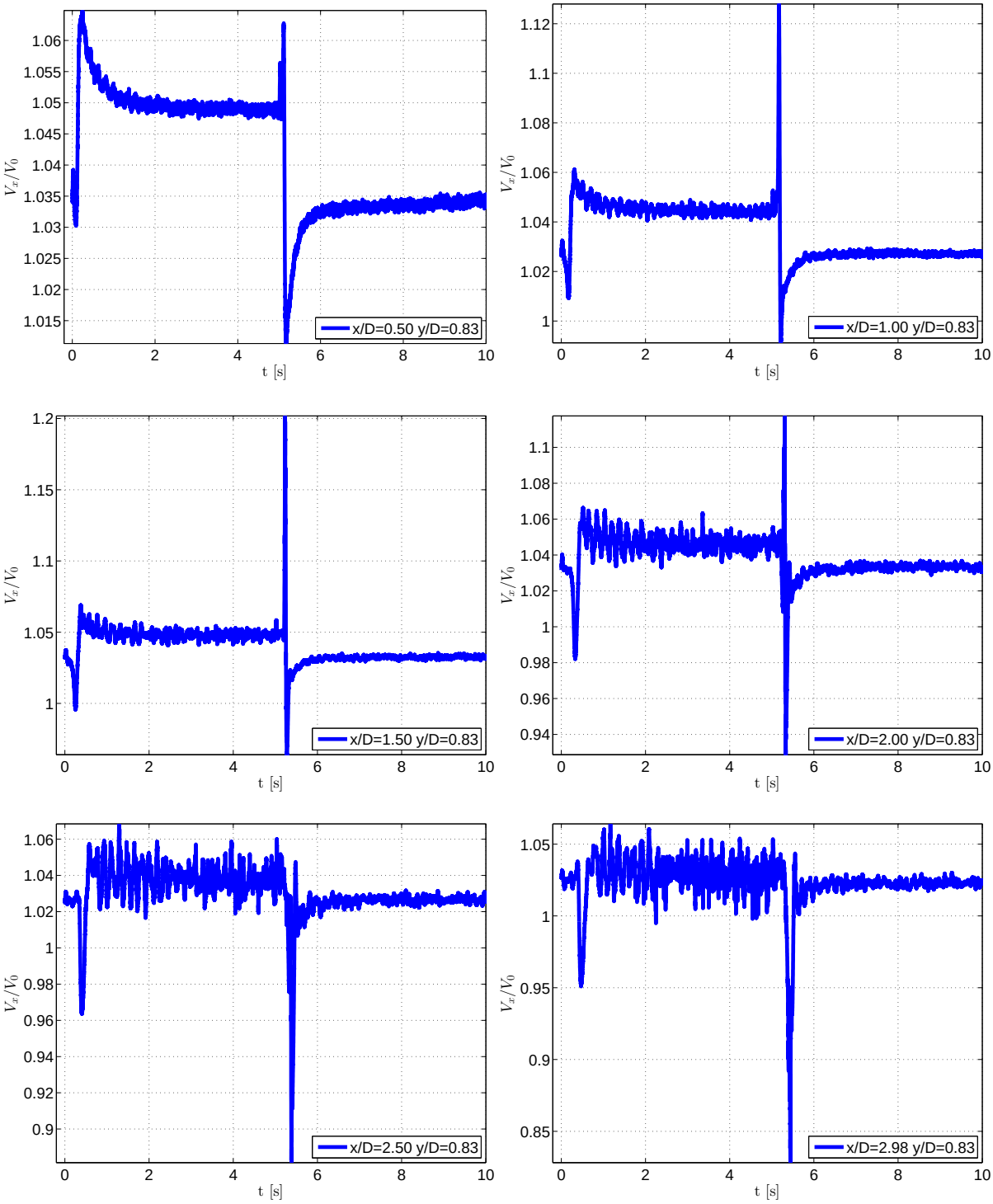

Figure 12.13: Experimental Results outside the Wake ($y/D = 0.83$).

General Remarks

From Figure 12.11 to Figure 12.13, it can be generally remarked that the number of unsteady load cycles sampled could be ideally larger in order to obtain an accurate value of the mean flow. While this could be possible if there was less time constraint, the mean flow characteristics under steady load conditions (i.e. generally between 3-5 s and 8-10 s of the unsteady loading cycle) have been, nevertheless, discussed in the previous section. Here, the discussion will focus on the transient

behaviour during the load change.

The flow in the shear layer is the most turbulent, with clearly more fluctuations compared to inner wake and outside wake regions. The shear layer is characteristics by the transport of the shed eddies, whose effect continues to manifest to the far downstream. In the inner wake, the flow through the holes of the porous disc is also likely to have small scale turbulent structures generated. Including the tower shadow effect, these two turbulent sources should be noted.

Of all regions, the flow in the outside wake is the least turbulent. This is expected since the flow is relatively undisturbed and the flow turbulence in the OJF had been earlier found to be low. Interestingly, by looking at the measurement points beyond $x/D = 2.00$, one can see that the flow during the high C_T part of the unsteady cycle, is more turbulent. This behaviour was not observed in the earlier upstream planes - which shows that the shear layer of the wake has begun to expand, due to the process of momentum entrainment. On the other hand, during the low C_T part of the unsteady cycle, there is still no apparent increase in velocity fluctuation, even at $x/D = 2.98$. This is due to the relatively stable shear layer - of which the onset of instability is delayed due to a lower velocity gradient across the shear layer.

From the above plots, the effect of C_T and its associated change of the flow inside and outside the wake can be seen. With an increase in C_T, the flow velocity inside the wake is predictably lower, but the velocity adjacent and just outside the wake also increases. This is due to the increase blockage effect afforded by the rotor with the higher C_T, with a corresponding larger wake diameter. This causes acceleration of the freestream - otherwise the mass conservation law would be violated.

Wake Velocity Overshoot

A key observation is the overshoot (or undershoot) of the flow velocity before the subsequent decay to the steady state value. This behaviour was observed in both the experimental and 3-D RANS simulations. Notably, in the wake region, the overshoot magnitude is relatively higher when the rotor is dynamically increased. It is hypothesised that the overshoot was caused by the passage of vortices as the thrust coefficient is changed. The fact that measurements show the overshoot occurrence having a delay proportionate to the downstream distance, suggest a travelling and momentous 'one-time' phenomena that has propagated from the rotor upon the sudden load change.

During the constant phase of the unsteady load cycle, the strength of the shed vortices in the shear layer is constant at a given downstream distance. Upon the unsteady onset, the loading condition across the rotor changes which causes the strength of vorticity to change. The 'new' vortices are shed at the disc edge and are subsequently convected by the mean flow. The passage of the 'old' and 'new' vortices pass the HWA probe causes an overshoot peak in the mean velocity.

A (positive or negative) overshoot is dependent on the position of the measurement probe with respect to the convection path of the 'old' and 'new' vortices upon the momentous change of loading. From the measurement results, the velocity overshoot effect is easily apparent, especially in the shear layer region and just outside the wake. Along the different downstream planes but at the same radial positions, the fact that the velocity overshoot is at positive or negative seem to suggest that the travel path of the shed vortices is not straight. This is corroborated by the vorticity contour maps, from the 3-D RANS model plotted at various multiples of the dynamic inflow timescale $\tau = \frac{D}{V_0}$, in Figure 12.14 and Figure 12.15. In both sudden load increase of decrease situations, one can observe the highly interactive nature between the 'old' and 'new' shed vortices.

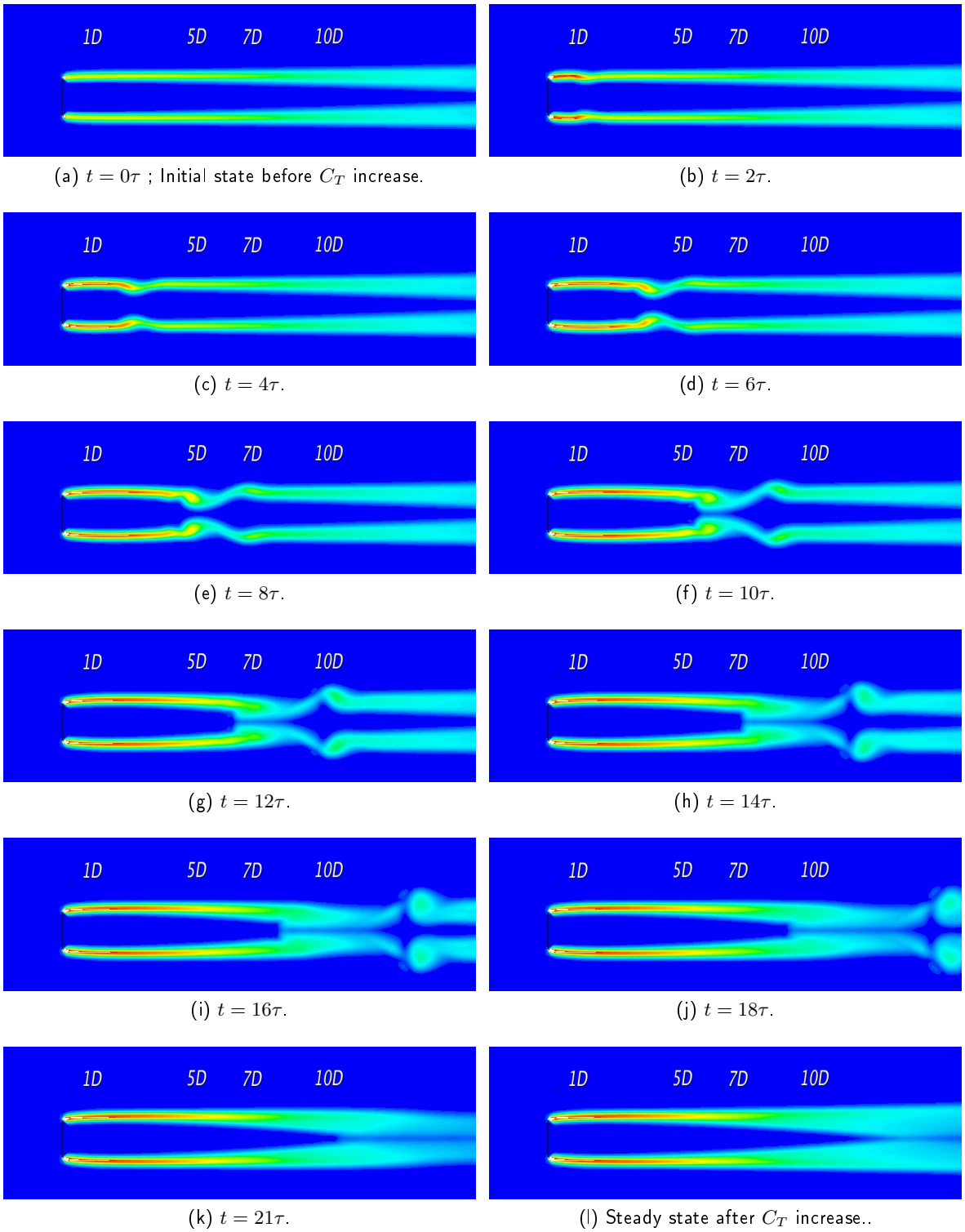

(a) $t = 0\tau$; Initial state before C_T increase.

(b) $t = 2\tau$.

(c) $t = 4\tau$.

(d) $t = 6\tau$.

(e) $t = 8\tau$.

(f) $t = 10\tau$.

(g) $t = 12\tau$.

(h) $t = 14\tau$.

(i) $t = 16\tau$.

(j) $t = 18\tau$.

(k) $t = 21\tau$.

(l) Steady state after C_T increase..

Figure 12.14: 3-D RANS vorticity contour maps after a sudden increase in C_T.

In sudden load increases cases, there is a larger wake expansion and a resulting lower mean speed convects the 'new' shed vortices, which are stronger in magnitude. From Figure 12.14, it can be seen that the lower speed 'new' wake lags behind the higher speed 'old' wake upon the sudden load change. As the wake expand and adjusts to a slower mean flow, the 'old' and 'new' vortices become 'detached' and roll up in a self-induction process. The passage of this complex vortex structure past a given a measurement point causes a what is seen as a overshoot. As the rolled up 'new' vortices are

convected, they are drawn towards each other due to the inter-induction process and finally interact downstream. The meet-up or interaction of the 'new' vortices at the edge of the 'new' wake is propagated downstream and are eventually diffused due to turbulent and viscous dissipation.

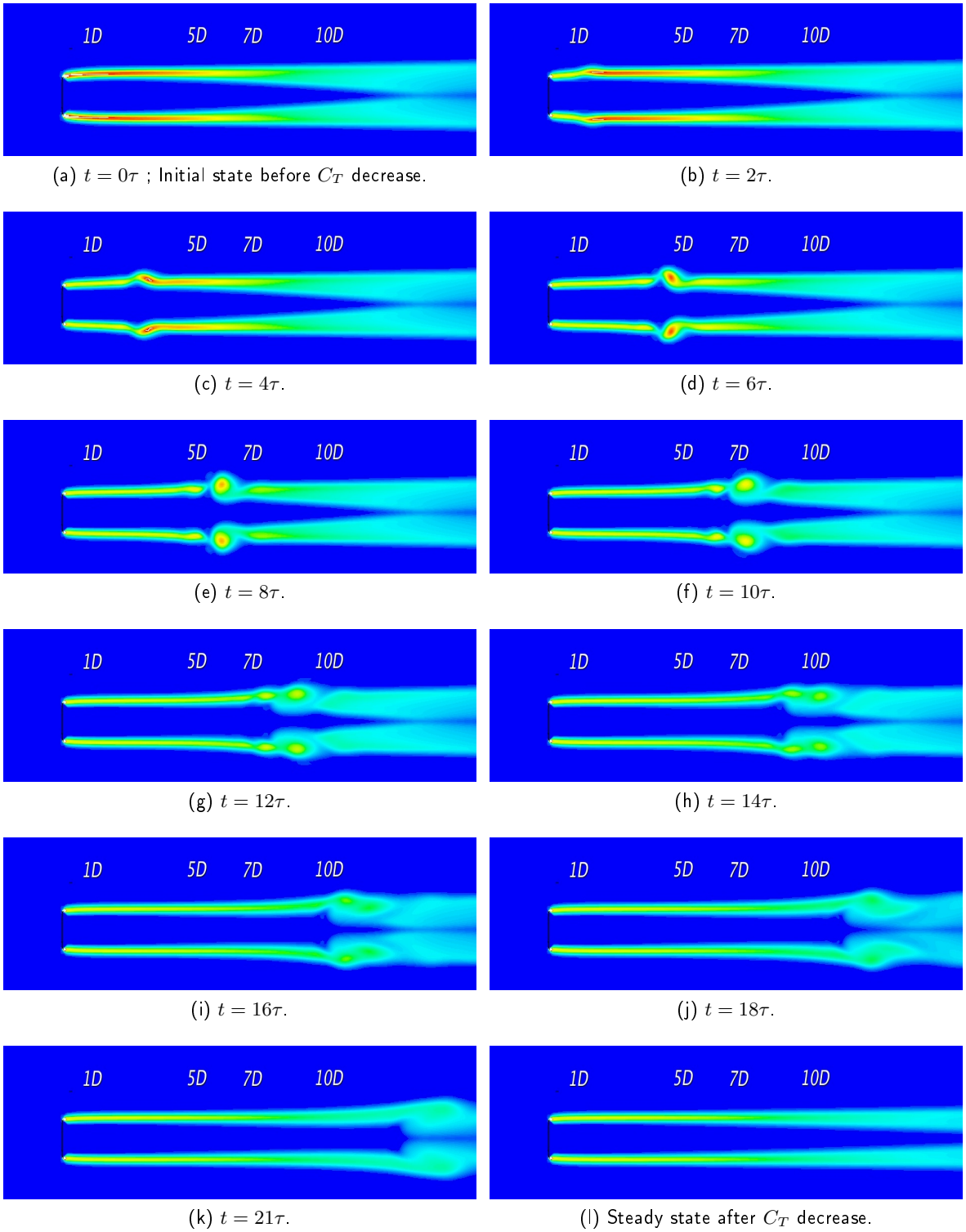

(a) $t = 0\tau$; Initial state before C_T decrease.

(b) $t = 2\tau$.

(c) $t = 4\tau$.

(d) $t = 6\tau$.

(e) $t = 8\tau$.

(f) $t = 10\tau$.

(g) $t = 12\tau$.

(h) $t = 14\tau$.

(i) $t = 16\tau$.

(j) $t = 18\tau$.

(k) $t = 21\tau$.

(l) Steady state after C_T decrease.

Figure 12.15: 3-D RANS vorticity contour maps after a sudden decrease in C_T.

In cases of sudden load decrease, the 'new' shed vortices are convected at a higher speed than their 'old' counterparts. In such scenarios, the 'new' vortices are leading the 'old' vortices. In a 'leap-

frogging' manner, which has been similarly observed in tip vortices interaction of blade rotors (see Figure 3.7), the 'old' and 'new' vortices eventually roll into each other to form rather distinct vortex cores. Similarly, the passage of a vortex core past a given measurement point causes a velocity overshoot. However, the existence of distinct vortex cores are momentous as their breakdown appear to take place almost immediately with its generation. The breakdown instability occurs due to the vortex stretching mechanism and as a result of the momentum entrained from the freestream. The vortex core is smeared, breaks down to smaller length scales and eventually to heat at the far downstream (about 10D in this load case). The exact distance of the formation and instability of the vortex core is hypothesized to vary and depends on the magnitude difference and the rate of change between the rotor's initial and final C_T.

For both load increase and decrease cases, the decay of the wake field to the 'new' equilibrium state is dependent on the rate of convection of the 'new' shed vortices. The near wake region for sudden C_T decrease cases is expected to attain the 'new' equilibrium state faster because of the faster mean flow convecting the 'new' shed vortices to the far field. This is also the likely explanation for the higher velocity decay rate at the inflow plane (discussed later in subsection 3.5). As the 'old' and 'new' shed vortices are convected away, the mean flow adjusts to the eventual equilibrium.

Important implications can be drawn based on what has been espoused in the preceding paragraph. The inflow and wake aft an unsteady loaded rotor is highly unsteady. For the upstream rotor, the unsteady inflow velocity means a fluctuating load response - meaning more fatigue damage. In a windfarm setting, rotors positioned downstream (10D is typical of many offshore windfarms) would be affected by the upstream wake. Subjected to non-uniform velocity in space and time, loads on downstream rotors would also be highly fluctuating during transient load changes on upstream rotors. This increase in fatigue damages would lead to shorter than expected operational lifetimes.

3 Benchmark of Dynamic Inflow Models

3.1 Methodology

In this section, the task is to benchmark the performance of the dynamic inflow engineering models of Pitt-Peters[49] and Øye[47] against the results derived from:

(a) Experimental porous disc used in the second test campaign

(b) Numerical RANS simulation

(c) Free Wake Vortex Ring (FWVR) model[71]

With the above in mind, it is important to realise that the output of the engineering models of Pitt-Petters and Øye is the inflow velocity response (at 0D), under unsteady load conditions. For the experimental simulations, it was not possible to place the measurement probe close to the rotor. Therefore, a transitive relation argument approach is proposed in order to benchmark the performance of the engineering models with experimental and numerical results. The transitive relation argument is such that:

$$\begin{aligned} &\text{If } a = b \text{ and } b = c, \\ &\text{then} \quad a = c. \end{aligned} \tag{12.3}$$

Using this argument, assuming all the results agree with each other, a and b represent the experimental and numerical results, while c is the Dynamic Inflow and FWVR models.

Even if it was practically possible to do so to measure the velocity just after the rotor, the comparison between the measured velocity response and other methods may be doubtful as the flow aft and close

to the rotor plane is susceptible to the small scale turbulent structures generated by the porous disc. Therefore, it is suggested that a better comparison basis would be the flow just upstream of the porous rotor, which could be measured by instead a PIV system. Alternatively, there are suggested analytical methods, such as one proposed by Wilson[68], which can predict the velocity induction at the rotor plane by using information of the flow velocity and its position along the rotor axis ($y = 0$). This was however, decided as inappropriate as the experimental data at $y =$ would have also been affected the vortical structures generated during the physical shift of the moving mesh (discussed at Figure 12.16). Furthermore, from the steady loading plots (see Figure 12.1), it is already known that the steady-state measured velocity values have slight discrepancies from the numerical computations. Hence, it was decided that it would be more appropriate to compare the normalised relative change of the flow velocity using:

$$\widetilde{\Delta V_x} = \frac{V_x - V_{x,s1}}{|V_{x,s2} - V_{x,s1}|} \tag{12.4}$$

The subscripts $s1$ and $s2$ represent the initial loading (before load change) and steady state (after load change). In this way, the self-normalised transient responses from the various methods could be compared.

3.2 Profile comparison between Experimental and 3-D RANS

Inner Wake

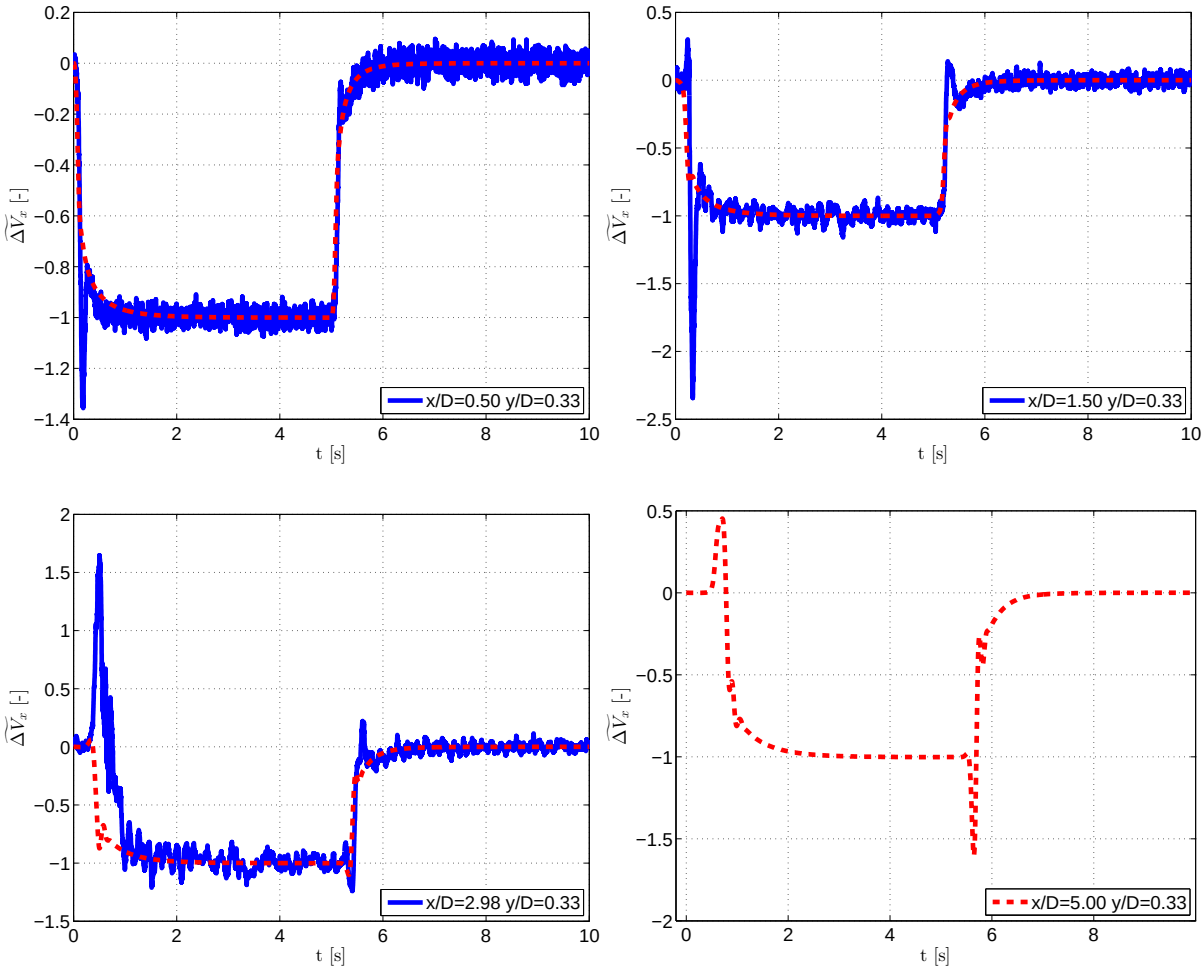

Figure 12.16: Experimental (−) and 3-D RANS (−−) results in the inner wake.

In the inner and near wake region (see Figure 12.16), 3-D RANS results do not necessarily reflect a velocity overshoot during the transient response. In the experiment results, overshoots are still seen and are likely because of the influence of the small scale turbulent structures from the porous mesh - which are not modelled in the 3-D RANS model. Depending on the loci of the chosen points in the inner near wake, no overshoot may be observed from the numerical computations if they are situated away from the convection path of the these vortical structures. After the load profile is suddenly changed, the 'new' shed vortices - released at the rotor's edge - interact with the 'old' vortices by process of self and inter-induction. Their influence eventually extends to the inner wake further downstream (see see vorticity contours in Figure 12.14 and Figure 12.15). As an illustrating example (see Figure 12.16), an overshoot effect is seen at $x/D = 5.00$ $y/D = 0.33$, even though none were seen at earlier planes.

Shear Layer and Just Outside Wake

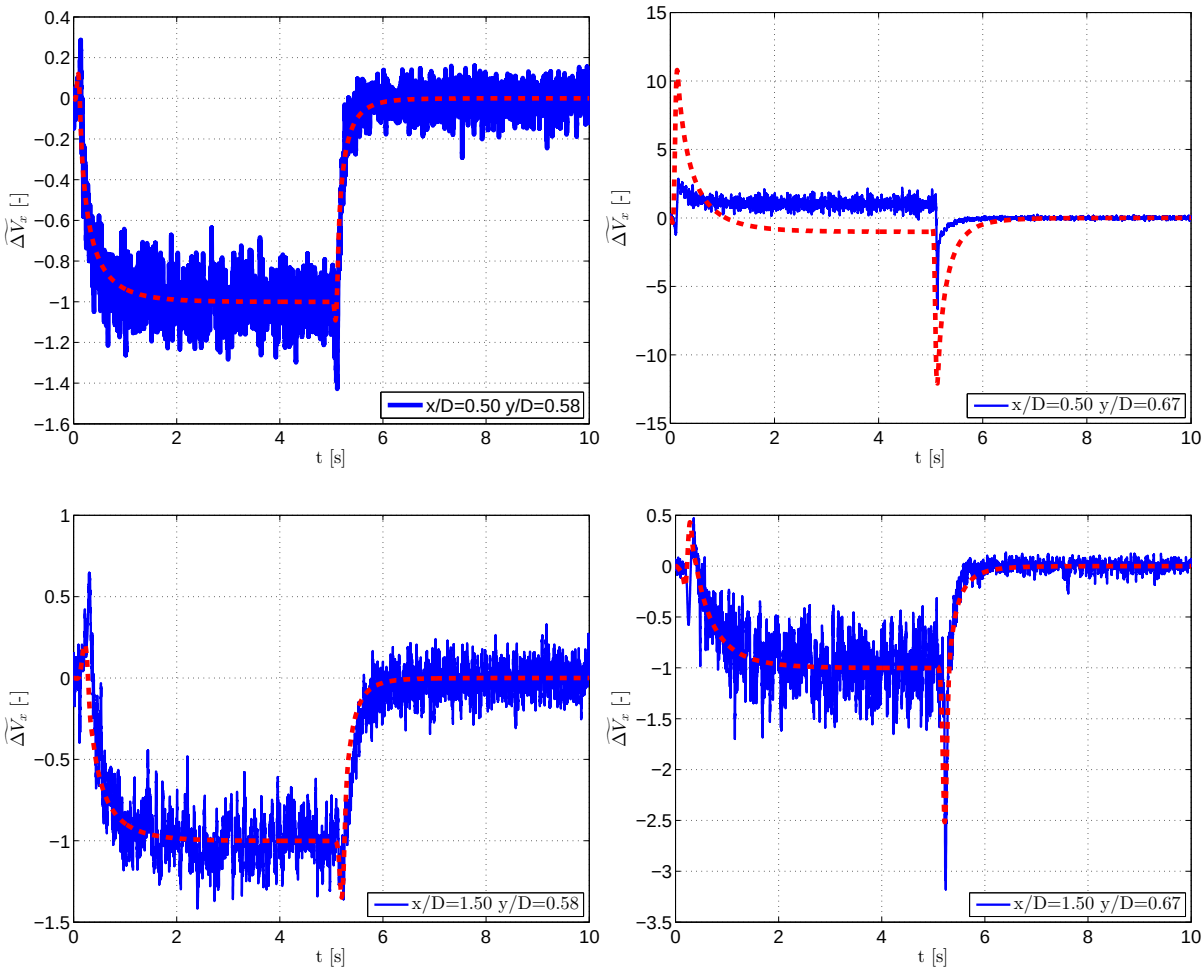

Figure 12.17: Experimental (—) and 3-D RANS (– –) results in the shear layer.

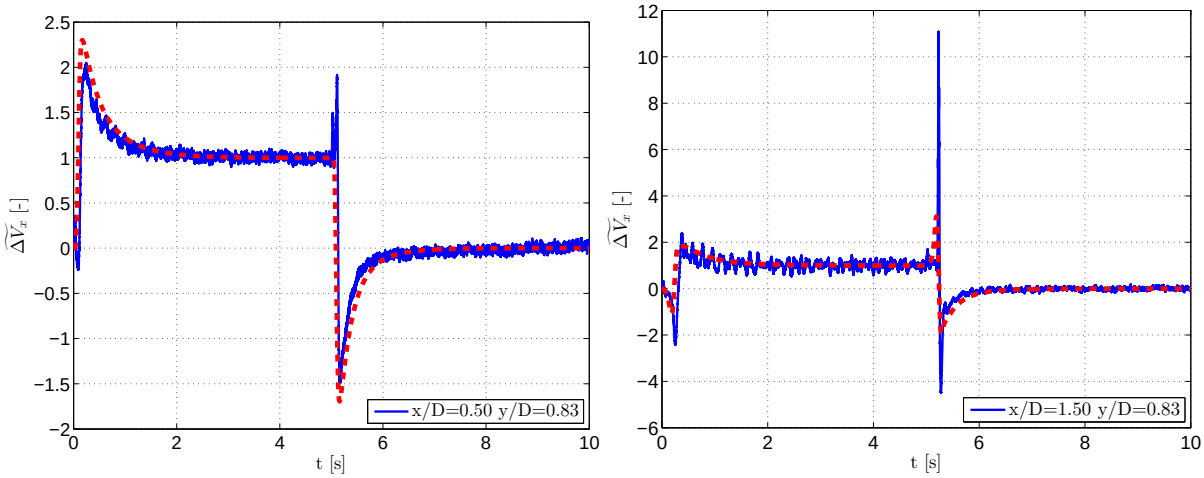

Figure 12.18: Experimental (—) and 3-D RANS (– –) results just outside the wake.

Based on the result at $x/D = 0.5$ $y/D = 0.67$ (see Figure 12.17), 3-D RANS simulation predict a faster wake expansion for high thrust coefficients. One can still see that the measured normalised velocity is still positive (i.e. measurement point is outside the wake). Whereas for the numerical computations, the similar point has a negative normalised velocity, meaning that the measurement point is in the wake of the rotor when $C_T = 0.82$. This discrepancy could be attributed to two reasons:

(a) the measured C_T value (which is used as an input to the 3-D RANS model) could be incorrect due to experimental errors. The C_T was measured at two mean wind speeds and values of 0.808 and 0.829 corresponding to 6 and 12 m/s were obtained for the low porosity state rotor. Given that the load cell had better signal-to-noise ratio at higher wind speeds, there could be C_T measurement error which resulted in an erroneous input to the numerical computations.

(b) the uneven edges of the porous disc (not present in the 3-D RANS model) and slight differences in the ambient turbulent intensity could also affect the wake expansion rate.

Nevertheless, the above figures still show that numerical computations are able to predict the transient velocity profiles with reasonable fidelity. The relative overshoot differences between the experimental and numerical profiles' is likely due to the non-exact positioning of the measurement probe in the experiments; the position of the measurement point would have an effect on the magnitude of the velocity overshoot.

3.3 Dynamic Inflow Time Decay

The unsteady velocity plots at various points of the wake field in the previous section have demonstrated the unsteady aerodynamics - overshoot due to passage of the 'old' and 'new' shed vortices, and the subsequent decay from the peak is associated with the in-stationary wake (of the convection of the time-varying shed vortices). The non-dimensional time associated with the former effect is represented as t_1^*, while t_2^* is associated with the dynamic inflow time decay (see Figure 12.19).

Extraction of this information from the time series data may be error prone as it is susceptible to judgement as to when the start and end times should be denoted. This susceptibility is more so for the experimental data, as the time series is fluctuating.

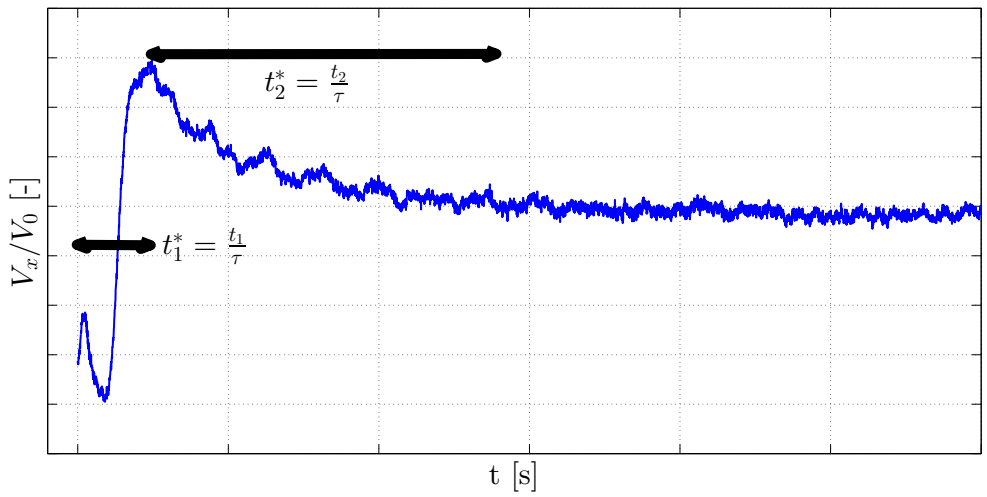

Figure 12.19: Non-dimensional delay times t_1^* and t_2^*, associated with the effects of in-stationary profile aerodynamics and wake respectively.

The dynamic inflow time delay t_2^* was estimated from the time series results from the experimental work and 3-D RANS simulations. Table 12.1 and Table 12.2 give the decay times for the sudden load increase and decrease cases respectively.

Table 12.1: Dynamic inflow time decay t_2^* at different rates of sudden load increase.

			Experiment			3-D RANS		
	y/D	δt^*	0.2	0.4	0.8	0.2	0.4	0.8
x/D = 0.5	0.33	t_2^*	1.9	3.5	4.4	6.9	6.9	7.0
	0.42		2.6	2.6	5.1	7.2	6.9	7.0
	0.50		3.6	2.0	2.5	7.6	7.7	7.7
	0.58		4.7	6.1	5.6	10.1	10.1	10.2
	0.67		5.6	3.4	7.2	25.8	25.8	25.6
	0.75			N.A.		15.2	15.1	15.0
	0.83		18.6	16.7	16.1	16.5	16.5	16.4
	1.00		15.0	12.5	12.6	18.8	18.8	18.7
x/D = 1.0	0.33	t_2^*	2.1	2.0	3.0	7.6	8.4	8.6
	0.42		3.0	2.2	5.0	7.5	7.5	7.6
	0.50		3.9	4.0	3.8	8.1	8.1	8.3
	0.58		6.1	8.2	4.6	10.4	10.4	10.5
	0.67		5.3	5.5	8.4	15.7	15.7	15.6
	0.75			N.A.		16.0	16.0	15.9
	0.83		8.5	12.8	9.9	15.6	15.6	15.5
	1.00		18.0	11.0	9.5	16.4	16.4	16.4
x/D = 1.5	0.33	t_2^*	3.9	3.8	3.1	6.3	6.3	6.3
	0.42		6.2	6.0	7.0	6.4	6.4	8.1
	0.50		5.4	6.0	5.6	8.6	8.6	8.6
	0.58		6.4	6.3	5.4	11.3	11.2	11.3
	0.67		6.9	9.6	10.2	15.0	15.0	14.9
	0.75			N.A.		18.0	18.0	17.8
	0.83		6.0	4.4	6.5	15.8	16.6	16.4
	1.00		8.0	6.1	8.1	16.4	16.4	16.4
x/D = 2.98	0.33	t_2^*	8.4	4.9	5.3	7.3	7.3	7.2
	0.42		6.4	8.5	9.2	9.2	9.2	9.3
	0.50		9.9	11.5	6.8	10.6	10.6	10.6
	0.58		9.1	7.8	5.0	13.4	13.4	13.5
	0.67		7.8	5.6	6.9	16.4	16.4	16.3
	0.75			N.A.		24.8	24.8	24.6
	0.83		1.4	1.5	1.7	18.6	18.5	18.3
	1.00		1.5	1.7	2.4	18.0	17.8	17.7
x/D = 5.0	0.33	t_2^*				7.2	7.1	7.0
	0.42					12.0	12.0	12.0
	0.50					15.1	15.1	15.0
	0.58					16.2	16.2	16.2
	0.67			N.A.		16.6	16.6	18.0
	0.75					22.8	22.8	22.6
	0.83					21.1	21.1	19.3
	1.00					20.0	20.2	18.3

Table 12.2: Dynamic inflow time decay t_2^* at different rates of sudden load decrease.

			Experiment			3-D RANS		
	y/D	δt^*	0.2	0.4	0.8	0.2	0.4	0.8
x/D = 0.5	0.33	t_2^*	4.2	8.2	5.0	5.3	5.3	5.6
	0.42		5.5	4.0	5.6	5.3	5.3	5.5
	0.50		4.0	4.9	3.7	5.6	5.6	5.8
	0.58		3.8	4.8	2.6	6.0	6.0	6.1
	0.67		8.0	6.8	6.0	18.8	18.8	18.7
	0.75			N.A.		11.2	11.2	11.1
	0.83		15.5	15.7	10.8	12.4	12.4	12.3
	1.00		8.3	11.8	12.0	14.4	14.4	14.4
x/D = 1.0	0.33	t_2^*	4.7	4.9	3.5	6.2	6.2	6.4
	0.42		4.5	3.4	3.5	6.2	6.2	6.4
	0.50		5.2	2.5	4.2	6.7	6.7	6.9
	0.58		5.5	6.4	6.4	5.9	5.9	6.0
	0.67		6.0	5.2	4.8	9.2	9.2	9.3
	0.75			N.A.		11.9	11.9	11.8
	0.83		10.2	9.2	10.4	11.9	11.9	11.7
	1.00		10.6	9.0	9.3	12.8	12.8	12.8
x/D = 1.5	0.33	t_2^*	4.7	7.3	4.3	7.1	7.1	7.4
	0.42		3.3	5.1	3.1	4.2	4.2	7.4
	0.50		6.1	4.9	7.4	7.9	7.9	8.1
	0.58		6.5	6.6	6.7	6.3	6.3	6.3
	0.67		4.2	5.4	6.2	8.2	8.2	8.2
	0.75			N.A.		13.4	13.4	13.3
	0.83		7.3	8.7	5.9	12.9	12.9	12.8
	1.00		8.6	7.0	9.0	13.5	13.5	13.3
x/D = 2.98	0.33	t_2^*	9.2	6.4	8.0	4.8	4.8	4.7
	0.42		5.2	7.4	6.9	4.9	4.9	5.0
	0.50		5.5	9.0	3.4	6.2	6.2	6.2
	0.58		8.4	6.7	7.6	7.9	7.9	7.9
	0.67		7.3	7.1	6.1	8.4	8.4	8.4
	0.75			N.A.		19.4	19.4	21.2
	0.83		4.0	2.3	3.0	14.9	14.9	16.2
	1.00		1.9	2.9	4.2	16.5	16.5	16.5
x/D = 5.0	0.33	t_2^*				6.0	6.0	6.1
	0.42					6.6	6.6	6.6
	0.50					8.6	8.6	8.6
	0.58					9.2	9.2	9.2
	0.67			N.A.		8.2	8.2	9.9
	0.75					17.6	17.6	17.5
	0.83					18.4	18.4	18.4
	1.00					17.9	17.9	17.8

Based on Table 12.1 and Table 12.2, the following observations were drawn:

(a) The decay times inside the wake are generally faster than other radial positions for a given downstream plane. The shorter decay time is due to the inside wake being more turbulent,

which facilitates momentum mixing and thus, resulting in the faster attainment of the new equilibrium. For the radial positions close to the rotor axis, the presence of the tower contributes further to the wake turbulence. As a result, one can also generally observe that experimental results at $y/D = 0.33$ have shorter decay times. Outside the wake, the flow is less turbulent and thus longer decay times were recorded. From the values, one can also deduce that the shear layer has begun to expand downstram due to the fact that the decay times at outer radial positions have begun to reduce. For the 3-D RANS, this shear layer expansion effect is limited to the radial position of $y/D = 0.67$.

(b) Between the experiment and numerical results, the decay times are generally shorter for the former. The underlying cause for this behaviour is the differences in the model setup. As opposed to the wind tunnel setup, the 3-D RANS model has neither small-scale turbulent structures generated at the rotor plane nor tower wake effects. These setup differences has resulted in the wake field having different turbulent intensity profiles (compare Figure 12.2 and Figure 12.5). The wake turbulence of the experimental setup is generally higher everywhere and has a twin peak, as result of the vortex shedded from the rotor edge and tower. As it would be later confirmed from numerical results (see explanation for Figure 12.20), there is a dominating effect of the flow's turbulent intensity on the decay rate. Hence, decay times under experimental conditions are generally shorter compared to the 3-D RANS model.

(c) From 3-D RANS computations, t_2^* for sudden load increase cases is clearly longer than that of load decrease cases. This result corroborates with what has been earlier explained. The faster convergence of the inflow velocity to the steady state equilibrium during sudden load decrease cases is afforded by the wake's higher mean flow which results in the faster convection of the 'new' vortices.

(d) Experimentally, there appears to be no apparent difference in the decay times between sudden load increase and decrease cases. While this has not been the case for the 3-D RANS model, it is hypothesised that this is due to the dominating effect of the flow's TI. The experimental TI is up to two or three times higher, especially at the tower and rotor tip regions, than the values compared to 3-D RANS predictions. This hypothesis was proven using CFD simulations and shown in Figure 12.20. One can observe that under low ambient TI conditions, t_2^* is indeed longer during a sudden load increase. The same cannot be said for that with high ambient TI, where t_2^* is almost similar whether for sudden load increase or decrease cases. Hence, it can be said that turbulence in the flow has a dominating effect on suppressing the effects of unsteady loading.

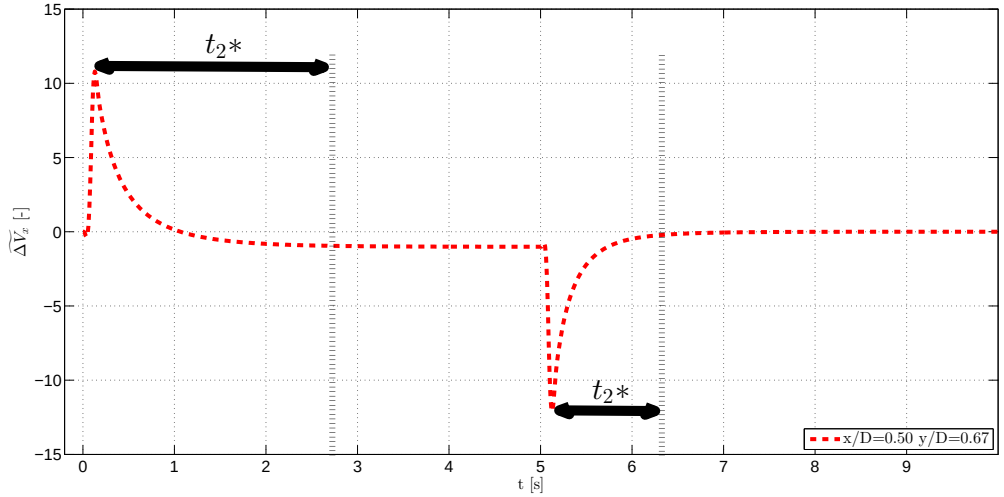

(a) Ambient $TI = 1\%$.

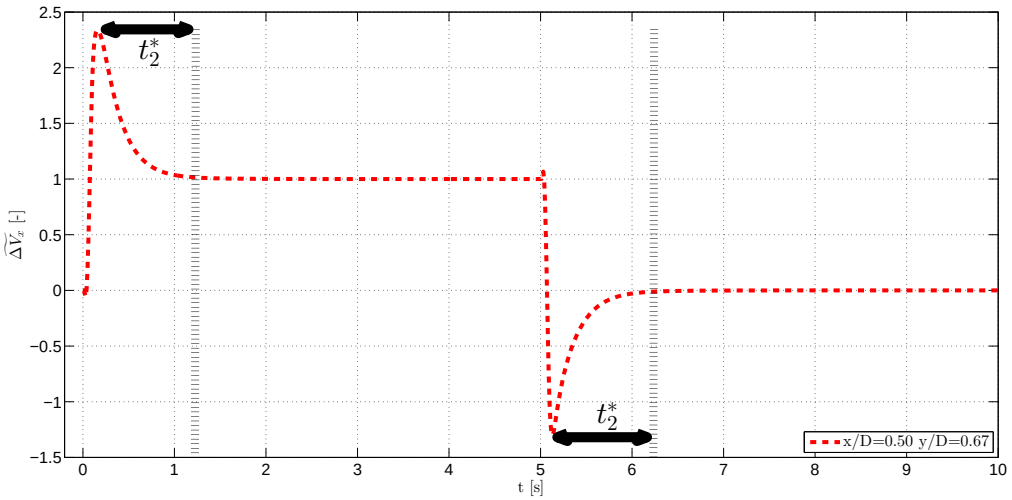

(b) Ambient $TI = 15\%$.

Figure 12.20: Comparison of transient responses for sudden load increase and decrease cases under different ambient TI conditions.

(e) The decrease of the unsteady load-time gradient, from $\delta t^* = 0.2$ to 0.8 has not appeared to reduce the dynamic inflow response. This was unlike the field experiments on real wind turbine machines[58], where $\delta t^* = 0.3$ to 0.5 were the time scales when the dynamic inflow phenomena was most apparent.

3.4 Different Unsteady Load Amplitude Profiles

In several of the above unsteady plots, it has been explained that an overshoot may be observed due to the passage of the 'old' and 'new' vortices through a given point along its convection path. Since there was essentially only one unsteady load profile i.e. from $C_T = 0.61$ to $C_T = 0.82$ and the opposite in the experiment, this subsection will leverage on CFD simulations to examine how different load profiles would affect the relative overshoot.

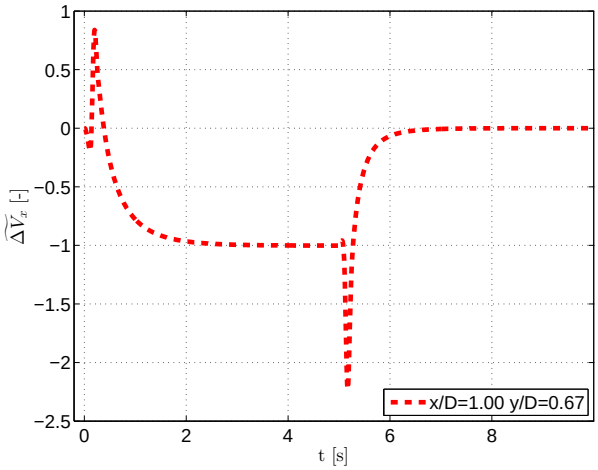

(a) C_T =0.61 to 0.82.

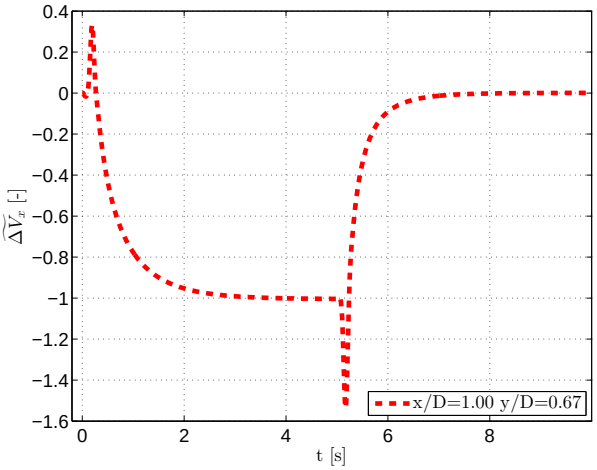

(b) C_T =0.78 to 0.89.

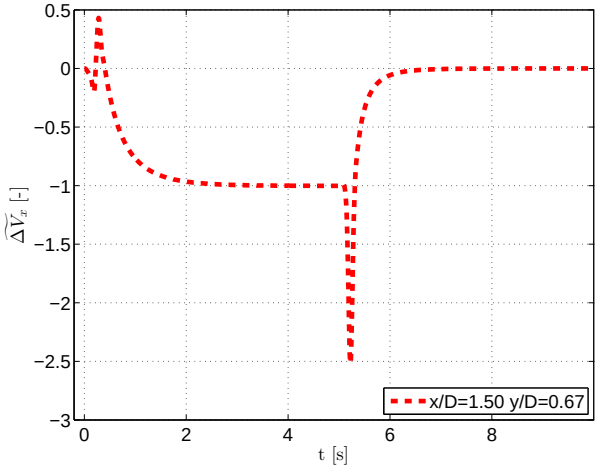

(c) C_T =0.61 to 0.82.

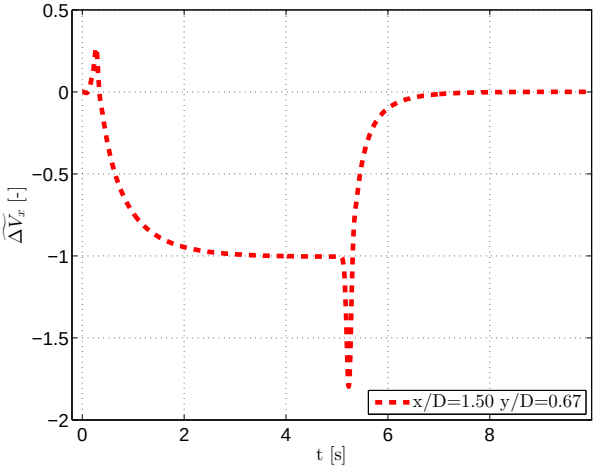

(d) C_T =0.78 to 0.89.

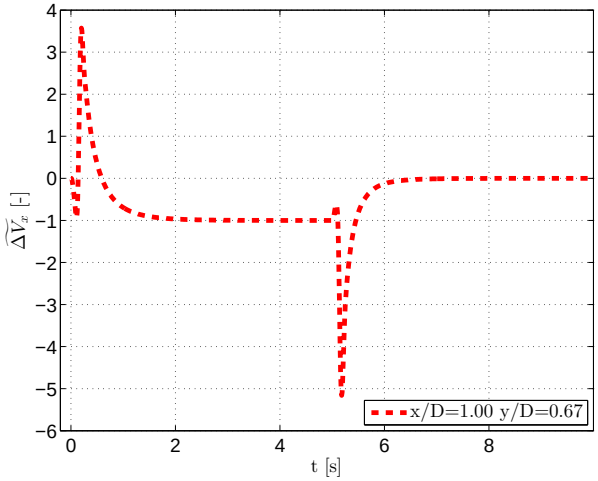

(e) C_T =0.50 to 0.71.

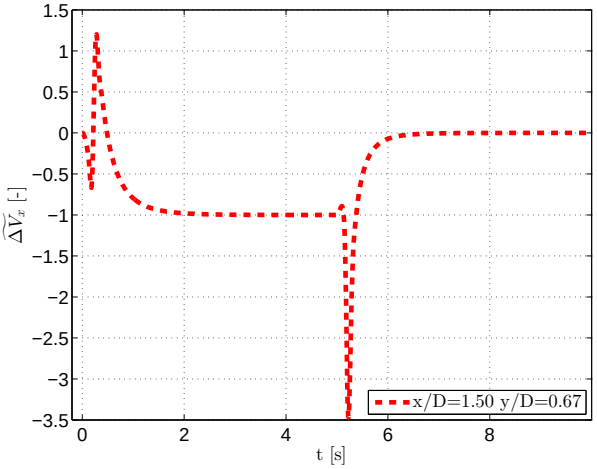

(f) C_T =0.50 to 0.71.

Figure 12.21: Overshoot response in relationship to different unsteady load amplitude profiles.

For a given unsteady load profile, the magnitude of the overshoot response is dependent on the position in the wake (as also seen in Figure 12.16). Whereas for a given point in the wake, the overshoot response increases with the amplitude of the load change (compare $C_T = 0.61$ to 0.82

and $C_T = 0.78$ to 0.89). This behaviour can be explained by the generation of stronger vortices, which thus causes a larger overshoot response as they travel through or close to the point. However for a given difference in the load change, there is no clear relationship with the amplitude of the relative overshoot. This is likely because for two vastly different initial C_T states, the trajectory of the shed vortices would also be different, owing to different wake expansions.

3.5 Comparison of Inflow Velocity Response predicted by 3-D RANS and FWVR

The average inflow velocity $V_{x,avg}$ at the rotor plane was computed from RANS and FWVR models and normalised using a similar expression from Equation 7.2. Together with the engineering models of Øye and Pitt-Peter, the transient velocity response was plotted against the non-dimensional time $t^* = \frac{t}{\tau}$. The instantaneous response or quasi-steady MT was also plotted for comparison.

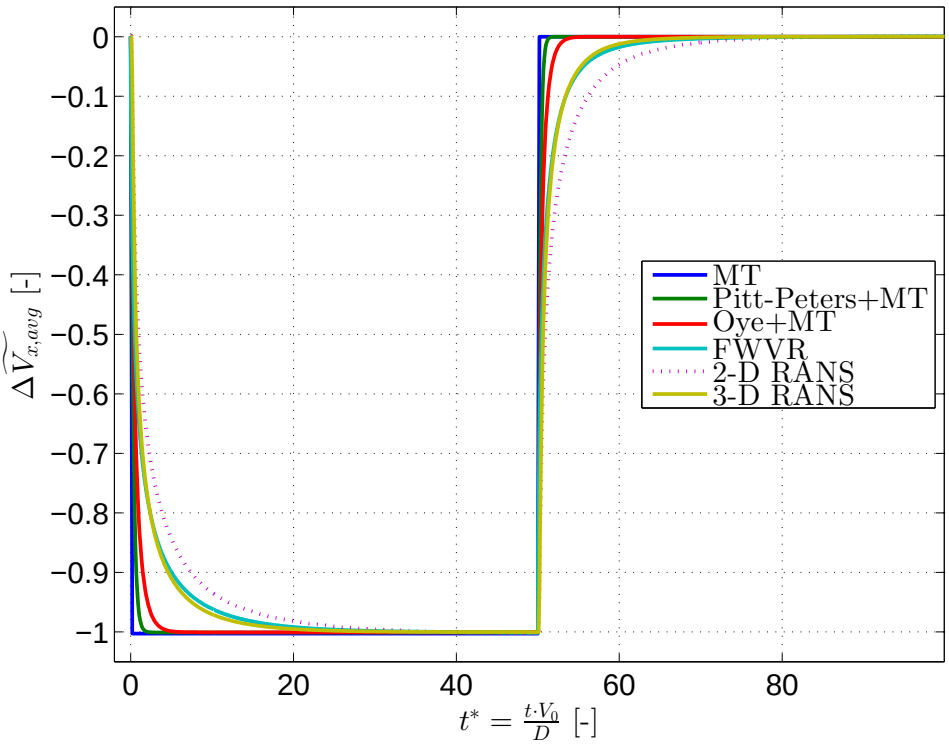

Figure 12.22: Inflow velocity response predicted by Dynamic Inflow Engineering Models, FWVR and 3-D RANS simulations.

From Figure 12.22, both engineering models predicted shorter decay times. Their respective decay rates are also equal in both sudden increase or decrease of C_T. On the other hand, both RANS and FWVR show a faster decay for sudden load decrease cases - the reason for which has been explained in the previous subsection. While relatively slower decay rates have been predicted by the current AD model, the rate is likely to be higher for real wind turbine blades. This is because real turbine blades have non-uniform loading along the blade span which would lead to vortices being shed across the rotor. The complex interaction of the 'old' and 'new' shed vortices during sudden blade pitch angles changes, as well as profile unsteady aerodynamics due to boundary layer separation delay, may lead to its earlier instability and result in the faster decay rates. Furthermore, the wake of a blade rotor is asymmetric due to its rotation which could further accelerate the instability onset.

In the above figure, the result of a 2-D RANS simulation of the problem has also been plotted. The discrepancy between 3-D RANS and 2-D RANS has demonstrated that flow effects across a disc rotor

are essentially 3-D and that by simplifying the problem, some accuracy has been lost.

Interestingly, prediction from the FWVR have a similar profile to that by a 3-D RANS. This close agreement demonstrate the validity of using vortex models to predict the transient response. The above results have been gathered from simulated cases of low ambient turbulence (in order to match the wind tunnel conditions). It is also important to note that the FWVR is an inviscid model which does not account for turbulent dissipation. Therefore, corrections may have to added onto FWVR to avoid unrealistic predictions.

To examine the influence of the ambient TI on the inflow velocity response, the 3-D RANS AD model was simulated at different ambient turbulence conditions. Figure 12.23 shows that there are indeed differences - higher ambient TI results in a faster decay which corroborates with what has been explained for Figure 12.20. As also discussed in chapter 7, the ambient TI has a dominating influence on the wake of a rotor under steady loading. Likewise, the ambient TI also appears to be the dominating influence on the transient inflow velocity response in sudden increase or decrease of loading. The decrease in response time is therefore likely due to the enhanced momentum mixing effect, which facilitates a faster transition to the new equilibrium state. This implies that ambient TI should somehow be included as a parameter in engineering models in order to improve predictions.

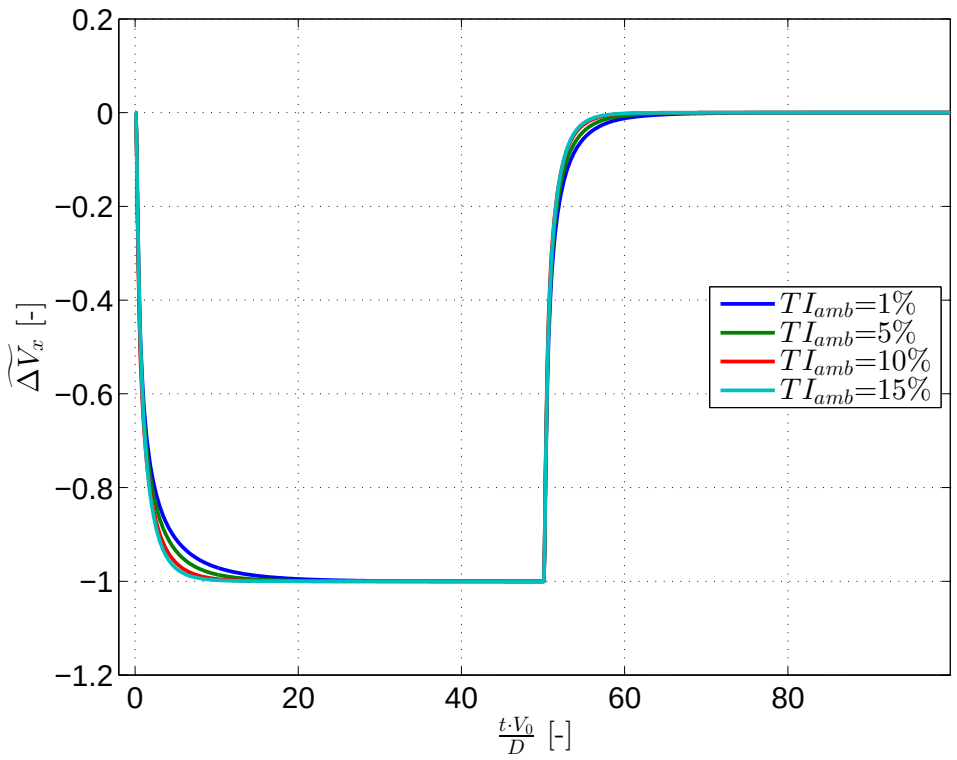

Figure 12.23: Ambient TI on the inflow velocity response prediction by 3-D RANS AD model.

"The future is green energy, sustainability, renewable energy."
Arnold Schwarzenegger (1947 – present)

13 Conclusions and Way Forward

The wake of an actuator disc under unsteady loading has been studied using experimental and numerical methods. The unsteady loading of an actuator disc was experimentally measured by using a porous disc rotor and dynamically invoking a controlled change in its porosity. The time-resolved wake field was sampled using a HWA in the OJF wind tunnel. Numerically, a 3-D RANS actuator disc model was setup in the commercial CFD code `Star-CCM+` and validated against momentum theory. Results from 3-D RANS simulations were then compared against the measured wake profiles of the disc rotor at two porosity states (different C_T). From the unsteady time series data, appropriate techniques such as power spectral and contour images were used to analyse the wake development and its properties. Finally, the transient inflow velocity responses predicted by the dynamic inflow engineering models of Pitt-Peters[49] and Øye[47] were benchmarked by the results from the experimental and 3-D RANS simulations, as well as the inviscid Free Wake Vortex Ring model[71].

1 Conclusions

The following points summarise the salient findings:

(a) The effects of the tower of a Horizontal Axis Wind Turbine on the rotor's inner wake is significant as the tower shadow effect would contribute to further velocity deficit and higher turbulent intensity, compared to a simulated rotor with no tower.

(b) For a rotor under steady loading, the wake from a higher C_T is relatively less stable as the instability of the shear layer occurs further upstream due to enhanced momentum mixing with the free stream (outside the wake). The enhanced momentum mixing is due to the shed vortices which are stronger as a result of the steeper velocity gradient at the disc edge. As a result, the velocity recovery process occurs relatively earlier.

(c) The wake of the porous disc rotor gave a Strouhal number of 0.16, which is in close agreement with the values measured on solid discs[17] and for a two bladed wind turbine[41] in previous works. This finding accentuates the fact that the wake of a blade rotor is meandering and can be compared to a disc rotor.

(d) Depending on the position in the wake field, there could be positive or negative velocity overshoot during the transient stage when the loading on a rotor suddenly changes. Vorticity

contour maps of a uniformly loaded rotor showed the generation and release of the 'new' shed vortices at the disc edge which is convected downstream by the mean flow. The 'old' and 'new' vortices have different vorticity magnitude owing to the amplitude of the load on the rotor. Depending on whether it is a load increase or decrease case, the 'old' and 'new' shed vortices interact with each other in a different manner. The passage effect by the 'old' and 'new' vortices over a given point causes a velocity overshoot, whose amplitude, direction and time of occurrence is dependent on the unsteady load profile and position of measurement point.

(e) The Dynamic Inflow engineering models of Pitt-Petters[49] and Øye[47] predict a higher decay rate of the inflow velocity ($0D$) when compared to the FWVR model[71] and 3-D RANS simulations. As real blade rotors have non-uniformly loaded rotors and have a asymmetric wake, the complex interaction of the spanwise and tip vortices could lead to an earlier onset of vortex instability and contribute to a higher decay rate.

(f) Whether for sudden load increase or decrease cases, both dynamic inflow engineering models predict the same decay rate. On the contrary, the 3-D RANS and FWVR, as well as experimental results, showed a slower decay rate for sudden load increase cases. From vorticity contour maps and velocity time series, it was observed that the strength and convection rate of the 'new' shed vortices to the far field have an influence on the inflow velocity's magnitude and convergence rate respectively. For sudden load decrease cases, the higher speed wake convects the shed vortices to the far field quicker and results in a faster velocity convergence at the rotor plane.

(g) As a vortex method, the FWVR has demonstrated to be a physical and reasonable representation of the problem and there was close agreement with 3-D RANS computations at low ambient turbulence. Using the 3-D RANS AD model, ambient TI was found to have a dominating influence on the wake's velocity response. It is hypothesised that this is the primary reason for the faster decay predicted by empirical-based engineering models of Pitt-Petters[49] and Øye[47]. Therefore, to apply vortex methods (such as the inviscid FWVR) and engineering models, viscous dissipation effects and parameters should be included to account for different levels of ambient turbulence.

2 Way Forward

Some enhancements and extension to the current work are proposed. These include:

(a) The approach undertaken to design the porous disc rotor has not been thoroughly systematic. It is suggested that an in-depth study on the aerodynamic effects are influenced by the various physical parameters (wires as opposed to perforated plates, hole size, hole-to-hole spacing etc). Furthermore, the importance of the gap clearance vis-a-vis the specific mesh-type material should be quantified for a rotor build using two meshes. This would allow better control of the desired C_T to be used in unsteady loading experiments.

(b) The use of PIV as a flow measurement technique could be advantageous in two ways towards this research. Firstly, the velocities just upstream of the porous disc rotor (undisturbed by the mesh grid) can be sampled. This would allow direct comparison with engineering models on the rotor's inflow velocity. Secondly, many of the flow features such as the interaction between the 'old' and 'new' vortices (that has been observed in CFD simulations) can be validated by experiment.

(c) To investigate the interactions between the span-wise and tip vortices of a real HAWT blade, the HAWT rotor could be simulated by a disc rotor with non-uniform radial loads. This would allow one to study the generation and release of vortices along the blade's span-wise, as well

as its effect on the near wake response. Some foreseen challenges would be the design of such of a disc, where a relationship between the placement and design of the holes may have to be empirically defined. While direct measurement of the radial loads would be a implementation challenge, PIV-derived velocity contour maps around the disc area could be used to back-compute the forces using momentum conservation equations.

(d) Similarly, controlled ambient turbulent flow could be generated in the wind tunnel to emulate the real operating environment. This would lend experimental confirmation on unsteady wind effects. The measured data could then spur adjustments to current engineering models in order to better predictions.

(e) Barring computation resource constraints, high fidelity time-resolved results using Large Eddy Simulation (LES) could be performed to validate the accuracy of RANS simulations.

Bibliography

[1] Ainslie, J. Calculating the flowfield in the wake of wind turbines. *Journal of Wind Engineering and Industrial Aerodynamics 27*, 1-3 (1988), 213–224.

[2] Alfredson, P. H., Dahlberg, J. A., and Bark, F. H. Some properties of the wake behind horizontal axis wind turbines. In *Proceedings of the 3rd International Symposium on Wind Energy Systems* (Lyngby, 1980), pp. 469–484.

[3] Alfredsson, P. H., and Dahlberg, J. A. A preliminary wind tunnel study of windmill wake dispersion in various flow conditions. *FFA Technical Note AU-1499* (1979).

[4] Alons, H. J. OJF External Balance Documentation.

[5] Ammara, I., Leclerc, C., and Masson, C. A Viscous Three-Dimensional Differential/Actuator-Disk Method for the Aerodynamic Analysis of Wind Farms. *Journal of Solar Energy Engineering1*, 124 (2002), 345–356.

[6] Andersen, S. J., Lignarolo, L. E. M., Ragni, D., Ferreira, C. J. S. a., Sø rensen, J. N., Mikkelsen, R. F., and van Bussel, G. J. W. Comparison between PIV measurements and computations of the near-wake of an actuator disc. *Journal of Physics: Conference Series 524* (2014), 012173.

[7] a.S. Bahaj, Myers, L., and Thompson, G. Characterising the wake of horizontal axis marine current turbines. *Proceedings of the 7th European Wave and Tidal Energy Conference* (2007).

[8] Aubrun, S., Devinant, P., Espana, G., Mécanique, L. D., and Vinci, L. D. Physical modelling of the far wake from wind turbines . Application to wind turbine interactions. *Ewec* (2007), 1–8.

[9] Aubrun, S., Loyer, S., Hancock, P. E., and Hayden, P. Wind turbine wake properties: Comparison between a non-rotating simplified wind turbine model and a rotating model. *Journal of Wind Engineering and Industrial Aerodynamics 120* (2013), 1–8.

[10] Barthelmie, R. J., Frandsen, S. T., Hansen, K., Schepers, J. G., Rados, K., Schlez, W., Neubert, a., Jensen, L. E., and Neckelmann, S. Modelling the impact of wakes on power output at Nysted and Horns Rev. *Ewec 2009* (2009).

[11] Barthelmie, R. J., Frandsen, S. T., Nielsen, M. N., Pryor, S. C., Rethore, P. E., and Jø rgensen, H. E. Modelling and measurements of power losses and turbulence intensity in wind turbine wakes at middelgrunden offshore wind farm. *Wind Energy 10*, 6 (2007), 517–528.

[12] Betz, A. Introduction to the Theory of Flow Machines. *Journal of Applied Mathematics and Mechanics 47* (1967), 140–141.

[13] Bjorck, A. Dynamic Stall and Three Dimensinoal Effect. *The Aeronautical Research Institute of Sweden* (1995).

[14] Briggs, K. Navigating the Complexities of Wake Losses. *North American Windpower* (2013).

[15] Buhl, M. L. A New Empirical Relationship between Thrust Coefficient and Induction Factor for the Turbulent Windmill State A New Empirical Relationship between Thrust Coefficient and Induction Factor for the Turbulent Windmill State. *Technical Report NREL/TP-500-36834*, August (2005).

[16] Burton, T., Jenkins, N., Sharpe, D., and Bossanyi, E. *Wind Energy Handbook*, 2nd ed. Wiley, 2011.

[17] Cannon, S., Champagne, F., and Glezer, a. Observations of large-scale structures in wakes behind axisymmetric bodies. *Experiments in Fluids 14*, 6 (1993), 447–450.

[18] Carpenter, P. J., and Fridovich, B. Effect of a Rapid Blade-Pitch Increase on the Thrust and Induced-Velocity Response of a Full-Scale Helicopter Rotor. Tech. rep., National Advisory Committee for Aeronautics, 1953.

[19] Carr, L. W. Dynamic stall progress in analysis and prediction. *AIAA 25*, 1 (1988), 6–17.

[20] Chorin, A. J. Blow-Up in Developed Turbulence. 853–866.

[21] Choudhry, A., Arjomandi, M., and Kelso, R. Lift Curve Breakdown for Airfoil undergoing Dynamic Stall. In *19th Australasian Fluid Mechanics Conference* (Melbourne, 2014), no. December.

[22] Crasto, G., Gravdahl, a. R., Castellani, F., and Piccioni, E. Wake modeling with the actuator Disc concept. *Energy Procedia 24*, January (2012), 385–392.

[23] Crespo, A., Hernandez, J., and Frandsen, S. Survey of modelling methods for wind turbine wakes and wind farms. *Wind Energy 2*, 1 (1999), 1–24.

[24] de Vaal, J. B., Hansen, M. O. L., and Moan, T. Effect of wind turbine surge motion on rotor thrust and induced velocity. *Wind Energy 17*, 1 (2014), 105–121.

[25] Fung, Y. C. *An Introduction to the Theory of Aeroelasticity*. Courier Corporation, 2002.

[26] Glauert, H. *The Elements of Aerofoil and Airscrew Theory*, 2nd ed. Press Syndicate of the University of Cambridge, 1926.

[27] Glauert, H. Airplane Propellers. In *Aerodynamic Theory*, W. F. Durand, Ed. Berlin: Springer Verlag, 1935, ch. XI.

[28] Green, D. R. R. Near wake wind tunnel studies. Tech. rep., Loughborough University, 1986.

[29] Green, D. R. R., and J., A. A. Measurement of velocity and turbulence profiles in flow situations relevant to wind turbine performance. Tech. rep., Loughborough University, 1985.

[30] Hansen, M. O. L. *Aerodynamicss of Wind Turbines*, 2nd ed. Earthscan, 2008.

[31] Harrison, M., Batten, W., Myers, L., and Bahaj, A. A comparison between CFD simulations and experiments for predicting the far wake of horizontal axis tidal turbines. In *8th European Wave and Tidal Energy Conference* (2009), pp. 566–575.

[32] Högström, U., Asimakopoulos, D., Kambezidis, H., Helmis, C., and Smedman, a. A field study of the wake behind a 2 MW wind turbine. *Atmospheric Environment (1967) 22*, 4 (1988), 803–820.

[33] Ivanell, S., Mikkelsen, R., Sø rensen, J., and Henningson, D. Three dimensional actuator disc modelling of wind farm wake interaction. *Interaction 1*, 20 (2008).

[34] Larsen, G. C. Dynamic wake meandering modeling. Tech. Rep. June, Risø, 2007.

[35] Lignarolo, L. E. M., Mehta, D., Stevens, R., Yilmaz, A. E., Meyers, J., Andersen, S. J., van Kuik, G. A. M., Meneveau, C., Holierhoek, J., Simão Ferreira, C. J., Ragni, D., and van Bussel, G. J. W. Comparison of LES and PIV measurements of actuator disk wakes in near field (In Preparation). 2015.

[36] Lignarolo, L. E. M., Ragni, D., Ferreira, C. J. S. a., and van Bussel, G. J. W. Kinetic energy entrainment in wind turbine and actuator disc wakes: an experimental analysis. *Journal of Physics: Conference Series 524*, Torque (2014), 012163.

[37] Lignarolo, L. E. M., Ragni, D., Krishnaswami, C., Chen, Q., Simão Ferreira, C. J., and van Bussel, G. J. W. Experimental analysis of the wake of a horizontal-axis wind-turbine model. *Renewable Energy 70* (2014), 31–46.

[38] Lignarolo, L. E. M., Ragni, D., Simão Ferreira, C. J., and van Bussel, G. J. W. Experimental comparison of a wind turbine and of an actuator disc wake.

[39] Lock, C. An extension of the vortex theory of airscrews with applications to airscrews of small pitch, including experimental results. Tech. rep., 1926.

[40] Medici, D. *Experimental Studies of Wind Turbine Wakes-Power Optimisation and Meandering*. PhD thesis, KTH Royal Institute of Technology, 2005.

[41] Medici, D., and Alfredsson, P. H. Measurements on a wind turbine wake: 3D effects and bluff body vortex shedding. *Wind Energy 9*, May 2005 (2006), 219–236.

[42] Medici D., and Alfredsson, H. Wind turbine near wakes and comparisons to the wake behind a disc. In *Proc. of the 43rd {AIAA} Aerospace Sciences Meeting and Exhibit* (Reno, Nevada, 2005), no. 595, pp. 1–12.

[43] Menter, F. R. Two-Equation Eddy-Viscosity Turbulence Models for Engineering Applications. *AIAA 32* (1994), 1598–1605.

[44] Menter, F. R. No T{A Comparison of some recent Eddy-Viscosity Turbulence Models}itle. *Journal of Fluids Engineering 118* (1996), 514–519.

[45] Miau, J. J., Leu, T. S., Liu, T. W., and Chou, J. H. On vortex shedding behind a circular disk. *Experiments in Fluids 23*, 3 (1997), 225–233.

[46] Milborrow, D. J., and Ross, J. N. The influence of turbulence and rotor thrust on wind turbine wake characteristics. *Memorandum TPRD/L/AP/0098/M83* (1983).

[47] Ø ye, S. Unsteady Wake Effects Caused by Pitch-Angle Changes. In *Proceedings of the First. IEA Symposium on the aerodynamic of wind turbines* (London, 1986), pp. 58–74.

[48] Ø ye, S. A simple vortex model of a wind turbine rotor. In *Third IEA Symposium on the Aerodynamics of Wind Turbines* (1989).

[49] Pitt, D. M., and Peters, D. a. Theoretical prediction of dynamic-inflow derivatives*. *Vertica 5*, September (1981), 21–34.

[50] Rethore, P., and Sø rensen, N. N. Validation of an Actuator Disc Model. Tech. rep., Wind Energy Division, RisøDTU, Denmark, 2010.

[51] Ross, J. N., and Ainslie, J. Wake measurements in clusters of model wind turbines using laser doppler anemometry. In *Proceedings of the 3rd BWEA Wind Energy Conference* (Cranefield, 1981), pp. 172–184.

[52] Sanderse, B. Aerodynamics of wind turbine wakes: Literature review. Tech. rep., ECN, 2009.

[53] Schepers, J. ENDOW: Validation and improvement of ECN's wake model. *Energy*, March (2003).

[54] Schepers, J. G. *Engineering models in wind energy aerodynamics*. PhD thesis, Technical University Delft, 2012.

[55] Sforza, P. M., Sheerin, P., and Smorto, M. Three-Dimensional Wakes of Simulated Wind Turbines. *AIAA 19*, 9 (1981), 1101–1107.

[56] Simms, D., Schreck, S., Hand, M., and Fingersh, L. J. NREL Unsteady Aerodynamics Experiment in the NASA-Ames Wind Tunnel : A Comparison of Predictions to Measurements NREL Unsteady Aerodynamics Experiment in the NASA-Ames Wind Tunnel : A Comparison of Predictions to Measurements. Tech. Rep. June, National Renewable Energy Laboratory, 2001.

[57] Smith, D., and Taylor, G. J. Further Analysis of Turbine Wake Development and Interaction Data. In *Proceedings of the 13th BWEA Wind Energy Conference* (1991), pp. 325–331.

[58] Snel, H., and Schepers, J. G. Joint Investigation of Dynamic Inflow Effects and Implementation of an Engineering Method. Tech. rep., ECN-C–94-107, 1995.

[59] Sø rensen, N., and Madsen, H. Modelling of transient wind turbine loads during pitch motion. *2006 European Wind Energy Conference di* (2006).

[60] Stock, M. J. Summary of Vortex Methods Literature (a living document rife with opinion). *Transport* (2007), 1–114.

[61] Talmon, A. M. The wake of a horizontal axis wind turbine model, measurements in uniform approach flow and in a simulated boundary layer. Tech. rep., TNO Division of Technology for Society, 1985.

[62] van Kuik, G. a. M. The edge singularity of an actuator disc with a constant normal load. *22nd AIAA/ASME Wind Energy Symposium*, January (2003).

[63] Vermeer, L. J. A review of wind turbine wake research at TUDelft, 2001.

[64] Vermeer, L. J., Sø rensen, J. N., and Crespo, a. Wind turbine wake aerodynamics. *Progress in Aerospace Sciences 39* (2003), 467–510.

[65] Vermeulen, P. E. J. An experimental analysis of wind turbine wakes. In *Proceedings of the 3rd International Symposium on Wind Energy Systems* (1980), pp. 431–450.

[66] Vermeulen, P. E. J., and Builtjes, P. J. H. Turbulence Measurements in Simulated Wind-turbine Clusters: Study Within the Framework of the IEA Programme of Research and Development of Wind Energy Conversion Systems, Annex V: "Study of Wake Effects Behind Single Turbines and in Wind-turbine Parks. Tech. rep., TNO Division of Technology for Society, 1982.

[67] Wilpert, P. *Drag and Wake Measurements on Cylinders and Discs for Wind Turbine Wake Modelling*. PhD thesis, 2014.

[68] Wilson, R. E. Wind Turbine Flow Field Model. *Journal of Solar Energy Engineering 108*, 345 (1986), 4–5.

[69] Winant, C. D., and Browand, F. K. Vortex pairing : the mechanism of turbulent mixing-layer growth at moderate Reynolds number. *Journal of Fluid Mechanics 63*, 02 (1974), 237.

[70] Wizelius, T. *Developing Wind Power Projects: Theory and Practice*. Earthscan, 2007.

[71] Yu, W., Simao Ferreira, C. J., van Kuik, G. A. M., and Baldacchino, D. Vortex ring model analysis of an actuator disc with unsteady, non-uniform load (Under Review). *Wind Energy 17*, April 2013 (2014), 657–669.

Appendices

A

Derivation of Reynolds Averaged Navier-Stokes Equations

To obtain the Reynolds-Averaged Navier-Stokes (RANS) equations, the Navier-Stokes equations for the instantaneous velocity and pressure fields are decomposed into a mean value and a fluctuating component. An averaging (temporal or ensemble averaging) technique will also be applied. The derivation will be shown in the following.

1 Derivation of Navier-Stokes Equations

Momentum Conservation

The law of momentum conservation law is applied by considering a control volume (CV) of fluid. The CV can be of any arbitrary shape and for simplicity, an infinitesimally small cube, representing a fluid particle, is considered (see Figure A.1).

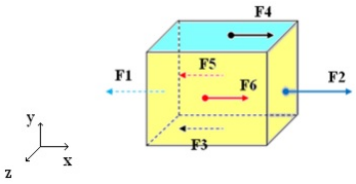

Figure A.1: Infinitesimally small cube of fluid representing by a fluid particle.

Using Taylor's formula, the body and surface forces acting on the CV are:

$$F_1 = -\left(\sigma_{xx} - \frac{dx}{2}\frac{\partial \sigma_{xx}}{\partial x}\right) dydz \qquad F_2 = \left(\sigma_{xx} + \frac{dx}{2}\frac{\partial \sigma_{xx}}{\partial x}\right) dydz$$
$$F_3 = -\left(\sigma_{yx} - \frac{dy}{2}\frac{\partial \sigma_{yx}}{\partial y}\right) dxdz \qquad F_4 = \left(\sigma_{yx} + \frac{dy}{2}\frac{\partial \sigma_{yx}}{\partial y}\right) dxdz$$
$$F_5 = -\left(\sigma_{zx} - \frac{dz}{2}\frac{\partial \sigma_{zx}}{\partial z}\right) dxdy \qquad F_6 = \left(\sigma_{zx} + \frac{dz}{2}\frac{\partial \sigma_{zx}}{\partial zy}\right) dxdy$$

where σ refers to the pressure. For example, the subscript xy refers to the pressure force acting in the x-direction onto the plane perpendicular to the y-axis.

The CV experiences body (e.g. gravity, centrifugal, electromagnetic) and surface forces (pressure and viscous). In the x-direction, one has:

$$\begin{aligned}\sum F_{x,surface} &= F_1 + F_2 + F_3 + F_4 + F_5 + F_6 \\ &= \left(\frac{\partial \sigma_{xx}}{\partial x} + \frac{\partial \sigma_{yx}}{\partial y} + \frac{\partial \sigma_{zx}}{\partial z}\right) dxdydz \\ \sum F_{x.body} &= \rho \cdot dxdydz \cdot g_x\end{aligned}$$

where gravity is assumed here to be the only force acting on the CV.

By considering momentum conservation in the CV, one has:

$$\begin{aligned}\text{x-direction}: \quad \left(\frac{\partial \sigma_{xx}}{\partial x} + \frac{\partial \sigma_{yx}}{\partial y} + \frac{\partial \sigma_{zx}}{\partial z}\right) dxdydz + \rho \cdot dxdydz \cdot g_x &= \rho \cdot dxdydz \cdot \frac{Du}{Dt} \\ \iff \frac{\partial \sigma_{xx}}{\partial x} + \frac{\partial \sigma_{yx}}{\partial y} + \frac{\partial \sigma_{zx}}{\partial z} + \rho g_x &= \rho \cdot \frac{Du}{Dt}\end{aligned} \tag{A.1}$$

where $\frac{Du}{Dt} = \frac{\partial u}{\partial t} + u\frac{\partial u}{\partial x} v\frac{\partial u}{\partial y} + w\frac{\partial u}{\partial z}$ is known as the total derivative.

Similarly, momentum conservation in the y and z direction gives:

$$\text{y-direction}: \quad \frac{\partial \sigma_{xy}}{\partial x} + \frac{\partial \sigma_{yy}}{\partial y} + \frac{\partial \sigma_{zy}}{\partial z} + \rho g_y = \rho \cdot \left(\frac{\partial v}{\partial t} + u\frac{\partial v}{\partial x} + v\frac{\partial v}{\partial y} + w\frac{\partial v}{\partial z}\right) \tag{A.2}$$

$$\text{z-direction}: \quad \frac{\partial \sigma_{xz}}{\partial x} + \frac{\partial \sigma_{yz}}{\partial y} + \frac{\partial \sigma_{zz}}{\partial z} + \rho g_z = \rho \cdot \left(\frac{\partial w}{\partial t} + u\frac{\partial w}{\partial x} + v\frac{\partial w}{\partial y} + w\frac{\partial w}{\partial z}\right) \tag{A.3}$$

Equation A.1, Equation A.2 and Equation A.3 are known as the Cauchy's momentum equations.

Alternatively, the pressure terms in the x-momentum can be expressed as:

$$\text{x-direction}: \quad \frac{\partial \sigma_{xx}}{\partial x} = -\frac{\partial P}{\partial x} + \frac{\tau_{xx}}{\partial x}, \quad \frac{\partial \sigma_{yx}}{\partial x} = -\frac{\tau_{yx}}{\partial x}, \quad \frac{\partial \sigma_{zx}}{\partial z} = \frac{\tau_{zx}}{\partial z}$$

By substituting the above into Equation A.1, one obtains:

$$\text{x-direction}: \quad -\frac{\partial P}{\partial x} + \frac{\tau_{xx}}{\partial x} + \frac{\tau_{yx}}{\partial x} + \frac{\partial \sigma_{zx}}{\partial z} + \rho g_x = \rho\left(\frac{\partial u}{\partial t} + u\frac{\partial u}{\partial x} v\frac{\partial u}{\partial y} + w\frac{\partial u}{\partial z}\right) \tag{A.4}$$

Similarly. for y- and z-direction, one obtains:

$$\text{y-direction}: \quad -\frac{\partial P}{\partial y} + \frac{\tau_{xy}}{\partial x} + \frac{\tau_{yy}}{\partial x} + \frac{\partial \sigma_{zy}}{\partial z} + \rho g_y = \rho\left(\frac{\partial v}{\partial t} + u\frac{\partial v}{\partial x} v\frac{\partial v}{\partial y} + w\frac{\partial w}{\partial z}\right) \tag{A.5}$$

$$\text{z-direction}: \quad -\frac{\partial P}{\partial z} + \frac{\tau_{xz}}{\partial x} + \frac{\tau_{yz}}{\partial x} + \frac{\partial \sigma_{zz}}{\partial z} + \rho g_z = \rho\left(\frac{\partial w}{\partial t} + u\frac{\partial w}{\partial x} v\frac{\partial w}{\partial y} + w\frac{\partial w}{\partial z}\right) \tag{A.6}$$

According to Stokes' hypothesis, one obtains:

$$\lambda = -\frac{2}{3}\mu$$

$$\begin{array}{lll} \tau_{xx} = 2\mu\frac{\partial u}{\partial x} + \lambda \bigtriangledown \cdot \overline{V} & \tau_{xy} = \mu\left(\frac{\partial v}{\partial x} + \frac{\partial u}{\partial y}\right) & \tau_{xz} = \mu\left(\frac{\partial w}{\partial x} + \frac{\partial u}{\partial z}\right) \\ \tau_{yx} = \mu\left(\frac{\partial u}{\partial y} + \frac{\partial v}{\partial x}\right) & \tau_{yy} = 2\mu\frac{\partial v}{\partial y} + \lambda \bigtriangledown \cdot \overline{V} & \tau_{yz} = \mu\left(\frac{\partial w}{\partial y} + \frac{\partial v}{\partial z}\right) \\ \tau_{zx} = \mu\left(\frac{\partial u}{\partial z} + \frac{\partial w}{\partial x}\right) & \tau_{zx} = \mu\left(\frac{\partial v}{\partial z} + \frac{\partial w}{\partial y}\right) & \tau_{zz} = 2\mu\frac{\partial w}{\partial y} + \lambda \bigtriangledown \cdot \overline{V} \end{array}$$

By substituting the above into the cauchy momentum equations Equation A.4, Equation A.5 and Equation A.6, one obtains:

$$\begin{aligned} \text{x-direction}: \quad & -\frac{\partial P}{\partial x} + \frac{\partial}{\partial x}\left[2\mu\frac{\partial u}{\partial x} + \lambda \bigtriangledown \cdot \vec{V}\right] + \frac{\partial}{\partial y}\left[\mu\left(\frac{\partial u}{\partial y} + \frac{\partial v}{\partial x}\right)\right] + \\ & \frac{\partial}{\partial z}\left[\mu\left(\frac{\partial u}{\partial z} + \frac{\partial w}{\partial x}\right)\right] + \rho g_x = \rho\left(\frac{\partial u}{\partial t} + u\frac{\partial u}{\partial x} + v\frac{\partial u}{\partial y} + w\frac{\partial u}{\partial z}\right) \\ \text{y-direction}: \quad & -\frac{\partial P}{\partial y} + \frac{\partial}{\partial x}\left[\mu\left(\frac{\partial u}{\partial y} + \frac{\partial v}{\partial x}\right)\right] + \frac{\partial}{\partial y}\left[2\mu\frac{\partial v}{\partial y} + \lambda \bigtriangledown \cdot \vec{V}\right] + \\ & \frac{\partial}{\partial z}\left[\mu\left(\frac{\partial v}{\partial z} + \frac{\partial w}{\partial y}\right)\right] + \rho g_y = \rho\left(\frac{\partial v}{\partial t} + u\frac{\partial v}{\partial x} + v\frac{\partial v}{\partial y} + w\frac{\partial v}{\partial z}\right) \\ \text{z-direction}: \quad & -\frac{\partial P}{\partial y} + \frac{\partial}{\partial x}\left[\mu\left(\frac{\partial u}{\partial z} + \frac{\partial w}{\partial x}\right)\right] + \frac{\partial}{\partial y}\left[\mu\left(\frac{\partial v}{\partial z} + \frac{\partial w}{\partial y}\right)\right] + \\ & \frac{\partial}{\partial z}\left[2\mu\frac{\partial w}{\partial y} + \lambda \bigtriangledown \cdot \vec{V}\right] + \rho g_z = \rho\left(\frac{\partial w}{\partial t} + u\frac{\partial w}{\partial x} + v\frac{\partial w}{\partial y} + w\frac{\partial w}{\partial z}\right) \end{aligned} \tag{A.7}$$

Navier-Stokes Equation

The equations in (A.7) are the fundamental equations that govern compressible fluid flow and are essentially the result of momentum conservation. However, in that current form, it is often inconvenient for writing and thus, Einstein notation (v_{ij}) is often used to express the x,y,z equations conveniently as:

$$\frac{\partial(\rho v_i)}{\partial t} + \frac{\partial(\rho v_i v_j)}{\partial x_j} = \rho g_i + \frac{\partial \sigma_{ij}}{\partial x_j} \tag{A.8}$$

where $\sigma_{ij} = -p\delta_{ij} + \mu\left(\frac{\partial v_i}{\partial x_j} + \frac{\partial v_j}{\partial x_i}\right)$.

Mass Conservation

Applying mass conservation, the fluid in the CV can be represented as:

$$\begin{aligned} & \frac{\partial \rho}{\partial t} + \bigtriangledown \cdot (\rho v_i) = 0 \\ \implies & \frac{\partial \rho}{\partial t} + \frac{\partial}{\partial x_j}(\rho v_i) = 0 \end{aligned} \tag{A.9}$$

By substituting Equation A.9 into LHS(Equation A.8), the following is obtained:

$$\text{Navier-Stokes Equations}: \quad \rho\left(\frac{\partial v_i}{\partial t} + v_j\frac{\partial v_i}{\partial x_j}\right) = \rho g_i + \frac{\partial \sigma_{ij}}{\partial x_j} \tag{A.10}$$

This is the general fundamental dynamics equations that governs fluid behaviour, famously known as the Navier-Stokes equations. Alternatively, the RHS of Equation A.10 can be expressed as:

$$\begin{aligned}\text{RHS of Equation A.10} &= \rho g_i + \frac{\partial}{\partial x_j}\left[-p\delta_{ij} + \mu\left(\frac{\partial v_i}{\partial x_j} + \frac{\partial v_j}{\partial x_i}\right)\right] \\ &= \rho g_i - \frac{\partial p}{\partial x_i} + \mu\left(\frac{\partial^2 v_i}{\partial x_j \partial x_j} + 0\right) \\ &= \rho g_i - \frac{\partial p}{\partial x_i} + \frac{\partial}{\partial x_j}(2\mu s_{ij})\end{aligned} \tag{A.11}$$

where $s_{ij} = \frac{1}{2}\left(\frac{\partial v_i}{\partial x_j} + \frac{\partial v_j}{\partial x_i}\right)$ is defined as the strain-rate tensor.

2 Reynolds Decomposition

The technique of Reynolds Decomposition is to express hydrodynamic quantities as the sum of its mean and fluctuating component. For example, the instantaneous velocity v and p can be expressed as:

$$\begin{aligned} v &= \overline{v} + v' = V + v' \\ p &= \overline{p} + p' = P + p' \end{aligned} \tag{A.12}$$

where the overbar and capitalised alphabets represents the mean value and $'$ represents the fluctuation from it.

Time Averaging

In measurements of statistically stationary flows, it is practically useful to use time averaged quantities i.e. flows in which averaged quantities are independent of time, to determine the mean value.

$$V = \overline{v(t)} = \lim_{T\to\infty}\frac{1}{T}\int_{t_0}^{t_0+T} v(t)\, dt \tag{A.13}$$

Ideally, to obtain a time independent value, the sampling time should be sufficiently large. Assuming that a limit exists, the average can be numerically computed with some degree of error. For periodic flows, T needs to be greater than all the random and periodic fluctuation time scales but less than that of which $\overline{V}$ varies.

Ensemble Averaging

Instead of using the time-averaged mean, one can consider an ensemble, or sets of independent data, where each set describes the same state of the flow. This ensemble $V^{(n)}; n = 1, ..., N$ can be gathered by carrying out the same experiment in N identical apparatuses or more realistically, by repeating the same experiment N times. N should also be large in order to obtain the true mean flow properties. This mean value is also known as the ensemble average defined as:

$$\overline{V} = \langle v \rangle = \frac{1}{N} \sum_{n=1}^{N} v^{(n)} \tag{A.14}$$

Implicitly, the N experiments are not exactly identical. Owing to fluctuations of turbulent flow, there would be differences during the same measurement phase of each experiment. In this sense, the concept of the ensemble average reduces the problem of approximating the true complete probability density function to the construction of realistic or acceptable probability density functions for the given conditions (i.e. initial conditions, inlet profiles, and any other external flow perturbations).

3 Derivation of Reynolds-Averaged Navier-Stokes Equations

To derive the incompressible RANS equations, we further assume the fluid is incompressible, meaning that $\frac{\partial \rho}{\partial t} = 0$.

Flow Incompressiblility and Mass Continuity

Since the fluid is incompressible, the general mass continuity equation can be expressed as:

$$\text{Equation A.9} \implies \frac{\partial v_i}{\partial x_i} = 0 \tag{A.15}$$

By applying Reynolds Decomposition, Equation A.15 becomes

$$\text{Equation A.15} \implies \frac{\partial V_i}{\partial x_i} = 0 \tag{A.16}$$

RHS of RANS

By applying Reynolds Decomposition, the RHS of the general RANS becomes:

$$\text{RHS (Equation A.11)} \implies \rho G_i - \frac{\partial P}{\partial x_i} + \frac{\partial}{\partial x_j}(2\mu S_{ij} - \rho \overline{v_i' v_j'}) \tag{A.17}$$

where $S_{ij} = \frac{1}{2}\left(\frac{\partial V_i}{\partial x_j} + \frac{\partial V_j}{\partial x_i}\right)$ is known as the mean strain-rate tensor.

LHS of RANS

Similarly, by Reynolds Decomposition, time-averaging and the result of Equation A.16, the LHS of Equation A.10 can be expressed:

$$\text{LHS (Equation A.10)} \implies \rho\left(\frac{\partial V_i}{\partial t} + \frac{\partial V_i V_j}{\partial x_j}\right) \tag{A.18}$$

RANS Equations

The Reynolds-Averaged Navier-Stokes (RANS) equations has thus been obtained from Equation A.17 and Equation A.18.

$$\rho\left(\frac{\partial V_i}{\partial t} + \frac{\partial V_i V_j}{\partial x_j}\right) = \rho G_i - \frac{\partial P}{\partial x_i} + \frac{\partial}{\partial x_j}(2\mu S_{ij} - \rho\overline{v_i' v_j'}) \tag{A.19}$$

By visual inspection, the RANS equations is nearly identical to the general Navier-Stokes equation (Equation A.10), except that an additional term now appears in the RHS. This additional term $\rho\overline{v_i' v_j'}$ is known as the Reynolds stress and $-\overline{v_i' v_j'}$ is known as the Reynolds stress tensor τ_{ij}, which can be mathematically shown to be

$$\tau_{ij} \equiv -\overline{v_i' v_j'} \equiv -\begin{pmatrix} \overline{v_1' v_1'} & \overline{v_1' v_2'} & \overline{v_1' v_3'} \\ \overline{v_2' v_1'} & \overline{v_2' v_2'} & \overline{v_2' v_3'} \\ \overline{v_3' v_1'} & \overline{v_3' v_2'} & \overline{v_3' v_3'} \end{pmatrix} \equiv -\begin{pmatrix} \overline{v_1'^2} & \overline{v_1' v_2'} & \overline{v_1' v_3'} \\ \overline{v_2' v_1'} & \overline{v_2'^2} & \overline{v_2' v_3'} \\ \overline{v_3' v_1'} & \overline{v_3' v_2'} & \overline{v_3'^2} \end{pmatrix} \tag{A.20}$$

The subscripts i and j denote Einstein's notations to give $v_1' = u'$, $v_2' = v'$, $v_3' = w'$. By decomposing the instantaneous quantities into mean and fluctuating components, three additional unknowns (v_i') have been introduced. Using RANS to resolve for the mean flow behaviour leads to the well-known turbulence closure problem because there are insufficient equations to solve the unknown variables. Additional equations or more commonly known as turbulence models need to be introduced to solve for each component of τ_{ij}. This subsequently ensures a determinate problem.

B

Vorticity Generation and Transport Equation

Vorticity is a vector field that describes the local spinning motion of a fluid. In mathematical operations, this is defined as the curl of the velocity field.

$$\omega = \bigtriangledown \times \overrightarrow{V}$$

The circulation of a flow field is defined as the line integral of a closed path of a vector field. In mathematical terms, this means

$$\overrightarrow{\Gamma} = \oint_C \overrightarrow{V} \cdot d\overrightarrow{l}$$

A flow need not to be rotating to have circulation. A flow can have zero vorticity, but yet have non-zero circulation, if its particles travel along curved trajectories and are not rotating about its centre of mass.

1 Derivation of the Vorticity Transport Equation

From the Navier-Stokes or RANS Momentum equation we have:

$$\rho \frac{\mathrm{D}\overrightarrow{V}}{\mathrm{D}t} = -\overrightarrow{\bigtriangledown} p + \rho \overrightarrow{f} + \mu \bigtriangledown^2 \overrightarrow{V} \tag{B.1}$$

The first term on the LHS represents the material derivative and can be represented as

$$\frac{\mathrm{D}\overrightarrow{V}}{\mathrm{D}t} = \frac{\partial \overrightarrow{V}}{\partial t} + (\overrightarrow{V} \cdot \bigtriangledown)\overrightarrow{V}$$

while noting that represents that $\mu \bigtriangledown^2 \overrightarrow{V}$ represents the diffusive term. $(\overrightarrow{V} \cdot \bigtriangledown)\overrightarrow{V}$ is the convective term which can be represented as

$$(\overrightarrow{V} \cdot \bigtriangledown)\overrightarrow{V} = \frac{1}{2} \bigtriangledown (\overrightarrow{V} \cdot \overrightarrow{V}) - \overrightarrow{V} \times (\bigtriangledown \times \overrightarrow{V}) = \bigtriangledown(\frac{v^2}{2}) - (\overrightarrow{V} \times \overrightarrow{\omega}) \tag{B.2}$$

Therefore, Equation B.1 can be re-written as

$$\frac{\partial \overrightarrow{V}}{\partial t} + (\overrightarrow{V} \cdot \bigtriangledown)\overrightarrow{V} = -\frac{1}{\rho}\overrightarrow{\bigtriangledown} p + \overrightarrow{f} + \nu \bigtriangledown^2 \overrightarrow{V} \tag{B.3}$$

To determine the vorticity transport equation, we take the curl of the momentum transport equation (i.e. Equation B.3 which is the Navier Stokes Equation).

$$\bigtriangledown \times \{\frac{\partial \overrightarrow{V}}{\partial t} + (\overrightarrow{V} \cdot \bigtriangledown)\overrightarrow{V} = -\frac{1}{\rho}\overrightarrow{\bigtriangledown} p + \overrightarrow{f} + \nu \bigtriangledown^2 \overrightarrow{V}\} \tag{B.4}$$

Thereafter, the following expressions were used to simplify each term of the vorticity transport equation in the following:

$$\text{Conservation of Mass, Incompressible Flow} \implies \bigtriangledown \cdot \overrightarrow{V} = 0$$
$$\text{Calculus Identity} \implies \bigtriangledown \times \bigtriangledown(scalar\ quantity) = 0$$

(a)

$$\begin{aligned} \bigtriangledown \times \frac{\partial \overrightarrow{V}}{\partial t} &= \frac{\partial}{\partial t}(\bigtriangledown \times \overrightarrow{V}) \\ &= \frac{\partial \overrightarrow{\omega}}{\partial t} \end{aligned}$$

(b)

$$\begin{aligned} \bigtriangledown \times (\overrightarrow{V} \cdot \bigtriangledown)\overrightarrow{V} &= \bigtriangledown \times \bigtriangledown(\frac{V^2}{2}) - \bigtriangledown \times (\overrightarrow{V} \times \overrightarrow{\omega}) \\ &= 0 - \bigtriangledown \times (\overrightarrow{V} \times \overrightarrow{\omega}) \\ &= \bigtriangledown \times (\overrightarrow{\omega} \times \overrightarrow{V}) \\ &= \overrightarrow{V} \cdot \bigtriangledown \overrightarrow{\omega} - \overrightarrow{\omega} \cdot \bigtriangledown \overrightarrow{V} + \overrightarrow{\omega}(\bigtriangledown \cdot \overrightarrow{V}) + \overrightarrow{V}(\bigtriangledown \cdot \overrightarrow{\omega}) \end{aligned}$$

(c)

$$\begin{aligned} \bigtriangledown \times (\nu \bigtriangledown^2 \overrightarrow{V}) &= \nu \bigtriangledown^2 (\bigtriangledown \times \overrightarrow{V}) \\ &= \nu \bigtriangledown^2 \overrightarrow{\omega} \end{aligned}$$

Thus, the vorticity transport equation (Equation B.4) can now be simplified as

$$\begin{aligned} \frac{D\overrightarrow{\omega}}{Dt} &= \frac{\partial \overrightarrow{\omega}}{\partial t} + (\overrightarrow{V} \cdot \bigtriangledown)\overrightarrow{\omega} \\ &= (\overrightarrow{\omega} \cdot \bigtriangledown)\overrightarrow{V} + \bigtriangledown \times \overrightarrow{f} + \nu(\bigtriangledown^2 \overrightarrow{\omega}) \end{aligned} \tag{B.5}$$

where $\frac{D\omega}{Dt}$ is the material or total derivative, which comprises of $\frac{\partial \overrightarrow{\omega}}{\partial t}$ as the time derivative, and $(\overrightarrow{V} \cdot \bigtriangledown)\overrightarrow{\omega}$ as the convective derivative.

- $(\overrightarrow{\omega} \cdot \bigtriangledown)\overrightarrow{V}$ is the vortex stretching Term, which physically represents the direction of the shed vortices.

- $\bigtriangledown \times \overrightarrow{f}$ is the body force term e.g. weight or applied force.
- $\nu(\bigtriangledown^2 \overrightarrow{\omega})$ is the viscous dissipation term of the vortices.

Equation B.5 tells one that if there is no generation and transport of vorticity ($\omega = 0$), it correspondingly means that the curl of the force ($\bigtriangledown \times \overrightarrow{f}$) is null. Vice versa, **vorticity is generated if there is a non-uniform force acting on the actuator discs** (by Newton's Second Law this force acts on the fluid). Therefore, we examine the term ($\bigtriangledown \times \overrightarrow{f}$), since this is the contributive term towards the generation of vorticity.

2 Uniformly loaded 1-D Actuator Disc

Mangitude and Direction of Vorticity

Alternatively, the vorticity in cylindrical coordinates can be expressed by

$$\omega = \bigtriangledown \times \overrightarrow{V} \tag{B.6}$$

$$= \frac{1}{r}\begin{vmatrix} \overrightarrow{e_r} & r\overrightarrow{e_\theta} & \overrightarrow{e_z} \\ \frac{\partial}{\partial r} & \frac{\partial}{\partial \theta} & \frac{\partial}{\partial z} \\ V_r & V_\theta & V_z \end{vmatrix} \tag{B.7}$$

$$= \frac{1}{r}\left[\left(\frac{\partial V_z}{\partial \theta} - \frac{\partial V_\theta}{\partial z}\right)\overrightarrow{e_r} - \left(\frac{\partial V_z}{\partial r} - \frac{\partial V_r}{\partial z}\right) r\overrightarrow{e_\theta} + \left(\frac{\partial V_\theta}{\partial r} - \frac{\partial V_r}{\partial \theta}\right)\overrightarrow{e_z}\right] \tag{B.8}$$

For illustration purposes, a non-rotating uniform flow (i.e. $\frac{\partial}{\partial r} = \frac{\partial}{\partial z} = V_\theta = 0$) is considered. Equation B.8 can be simplified as:

$$\text{Equation B.8} \implies -\frac{\partial V_z}{\partial r}\overrightarrow{e_\theta}$$

This above expression gives information that the vorticity magnitude is dependent on the radial velocity gradient and travels in the azimuthal direction.

Vorticity Generation

For simplicity, a 1-D uniformly loaded actuator disc ($\omega_x = \omega_y = \frac{\partial}{\partial z} = 0$) and inviscid ($\nu = 0$) flow is assumed. This gives rise to a simplification of the vorticity equation:

(a) $(\overrightarrow{\omega} \cdot \bigtriangledown)\overrightarrow{V} = \left(\omega_x \frac{\partial}{\partial x} + \omega_y \frac{\partial}{\partial y} + \omega_z \frac{\partial}{\partial z}\right)\overrightarrow{V} = 0$

(b) $\nu \bigtriangledown^2 \overrightarrow{\omega} = 0$

$$\therefore \text{Equation B.5} \implies \frac{D\vec{\omega}}{Dt} = (\vec{\omega} \cdot \bigtriangledown)\vec{V} + \bigtriangledown \times \vec{f} + \nu \bigtriangledown^2 \vec{\omega}$$

$$= \bigtriangledown \times \vec{f}$$

$$= \begin{vmatrix} \vec{i} & \vec{j} & \vec{k} \\ \frac{\partial}{\partial x} & \frac{\partial}{\partial y} & \frac{\partial}{\partial z} \\ f_x & f_y & f_z \end{vmatrix}$$

$$= \left(\frac{\partial f_z}{\partial y} - \frac{\partial f_y}{\partial z}\right)\vec{i} - \left(\frac{\partial f_z}{\partial x} - \frac{\partial f_x}{\partial z}\right)\vec{j} + \left(\frac{\partial f_y}{\partial x} - \frac{\partial f_x}{\partial y}\right)\vec{k}$$

$$= -\frac{\partial f_x}{\partial y}\vec{k}$$

Since $\vec{f}$ represents the force acting on the fluid, there would be no vorticity generated if no force is applied by the actuator onto the fluid (i.e. $\vec{f} = 0 \implies \frac{D\vec{\omega}}{Dt} = 0$). For an actuator disc with uniform loading, this means $\frac{\partial f_x}{\partial y} = 0$ everywhere in the flow, except at the edges. At the edges, force discontinuity means that $\frac{\partial f_x}{\partial y} \neq 0$, which implies that the vorticity would be generated at there. This is also the region where there is a significant velocity gradient, between the wake behind the disc and the freestream.